Queen Mary
University of London

Ferromagnetically filled carbon nanotubes: Radial structures and tuning of magnetic properties through new synthesis methods.

Boi, Filippo

The copyright of this thesis rests with the author and no quotation from it or information derived from it may be published without the prior written consent of the author

For additional information about this publication click this link.
http://qmro.qmul.ac.uk/jspui/handle/123456789/8734

Information about this research object was correct at the time of download; we occasionally make corrections to records, please therefore check the published record when citing. For more information contact scholarlycommunications@qmul.ac.uk

School of Physics and Astronomy

Ferromagnetically filled carbon nanotubes:

Radial structures and tuning of magnetic properties through new synthesis methods.

Doctoral Thesis

Filippo Boi

Queen Mary University of London

Supervisors: Dr. M. Baxendale and Dr. G. Mountjoy

Declaration

I declare that this work was performed entirely by myself during the course of my Ph.D. studies at the School of Physics and Astronomy, Queen Mary University of London and at the School of Physical Sciences, University of Kent, under the supervision of Dr. Mark Baxendale and Dr. Gavin Mountjoy. No part of this thesis has been submitted elsewhere for any other degree.

Filippo Boi

Acknowledgements

Without the following people this special journey in the wonderful world of carbon nanotubes would not have been possible.

My greatest thanks go to my supervisors, Dr. Mark Baxendale and Dr. Gavin Mountjoy, for their continuous support, guidance and patience in the course of this project.

Many thanks also to Prof. David Dunstan and Dr. Alan Drew for their important help and support.

Thanks also to the financial support from the South-East Physics Network.

I would like to thank also all the support staff that helped me in these three years: Dr. Ken Scott and Mr. Geoff Gannaway for the help in the reactor design and preparation, Mr George Nevill for the important help in the quartz substrates preparation, Dr. Zofia Luklinska for the help in scanning electron microscopy and transmission electron microscopy, Dr. Rory Wilson for the help in the X-ray diffraction measurements. I also would like to thank Prof. Neal Skipper for the help in the X-ray diffraction measurements performed in the first year.

Many thanks also to Dr. Liam Spillane and Dr. Lisa S. Karlsson for the great help in the electron microscopy investigations and result interpretation, and to Dr. Richard Thorogate for the help in the magnetic measurements.

I also would like to thank Dr. Anna Corrias for the great help in the X-ray diffraction measurements and also for all the support that I received in these years.

A special thank also to my family for the support, encouragement and love that I always received in my life.

Thanks also to all my friends for the help and the great time that we had in this journey: Ali Karatutlu, Calum McAndrew, Emanuele Mura, Valeria Isu, Carlos Aristizabal, Laura Sawiak, Serena Maugeri, Eva Zarkadoula, Hongtao Zhang, Huanqing Ye, David Holford, Shuo Han, Min Gao, Osman Ersoy, Yan Li, Sai Maddala, Shankui Chang, Dominic Carter, Will Little, Asmi Barot, Yuan Li, Shamim Khademi, Helen Duncan, Maureen Willis, Greg Fletcher, Tingting Zhang, Chenxing Yang, Yiwei Sun, Taze Peci, Mingying Song, Juan Du, Eleftherios Andritsos and Giacomo Snidero.

Abstract

Multiwall carbon nanotubes filled with continuous single-crystals of the ferromagnetic phase α-Fe were produced with two new synthesis methods: the boundary layer chemical vapour synthesis and the perturbed vapour chemical vapour deposition. In the first method, the nanotubes nucleate and grow radially from a central agglomeration of homogeneously nucleated spherical particles in a randomly fluctuating vapour created in the viscous boundary layer between a rough surface and a laminar pyrolyzed-ferrocene/Ar vapour flow. In the second method, the nanotubes nucleate and form in a flower-like arrangement departing from homogeneously nucleated particles. These particles are produced by the creation of a local perturbation in a vapour with a high density of Fe and C species obtained from the pyrolysis of ferrocene in a laminar Ar flow.

Electron microscopy investigations revealed that the continuous single crystals obtained with both methods exhibit diameters much lower than the critical diameter for a single magnetic domain of α-Fe (~ 66 nm). In the radial structures, the single-crystal diameter is in the range of ~ 17-37 nm, while in the flower-like structures the single crystals show mainly a diameter of ~ 30 nm and ~ 55 nm. The average single crystals length is 7-8 μm in the case of the radial structures and 19-21 μm in the case of the flower-like structures. DC magnetization measurements at 5 K show different magnetic behaviours. The flower-like structures present a very high saturation magnetization of 189.5 emu/g and a high coercivity of 580 Oe. The radial structures exhibit an exchange-coupled

ferromagnetic/antiferromagnetic system despite only 2% of γ-Fe is present inside the nanotubes. The radial structures obtained at flow-rates of 3.5 ccm and 20 ccm, show saturation-magnetizations of 31emu/g and 13 emu/g, and coercivities of 790 Oe and 843 Oe respectively.

Publications:

i) F. S. Boi, G. Mountjoy, Z. Luklinska, L. Spillane, L. S. Karlsson, R. M.Wilson, A. Corrias, and M. Baxendale. The Origin of Long-Period Lattice Spacings Observed in Iron-Carbide Nanowires Encapsulated by Multiwall Carbon Nanotubes. Microscopy and Microanalysis 2013; 19: 1298-1302.

ii) F. S. Boi, G. Mountjoy, and M. Baxendale. Boundary layer chemical vapor synthesis of self-organized radial filled-carbon-nanotube structures. Carbon 2013; 64: 516-526.

iii) F. S. Boi, G. Mountjoy, R. M. Wilson, Z. Luklinska, L. J. Sawiak and M. Baxendale. Multiwall carbon nanotubes continuously filled with micrometre-length ferromagnetic α-Fe nanowires. Carbon 2013; 64: 351-358.

Patents:

F. S. Boi, G. Mountjoy, and M. Baxendale. Boundary layer chemical vapor synthesis of self-organized radial filled-carbon-nanotube structures (patent application number GB1222781.5).

Contents:

List of figures

12: Growth mechanism of a carbon nanotube involving the supersaturation of the catalyst with carbon and the formation of Fe_3C. The instability of Fe_3C appears to be the key for nanotube growth [15].

13: Schematic diagram representing the open-ended base growth mechanism [17].

14: Fe-C phase diagram [18].

15: X-ray diffractograms of annealed (top) and unannealed (bottom) filled MWCNTs [7]. The peak indicated with the symbol Si refers to the 311 reflection of Si (space group Fd-3ms) and is due to the substrate where the MWCNTs were grown.

16: HRTEM micrographs of unknown Fe-C single crystals with anomalously long lattice spacings [11].

17: HRTEM micrographs of unidentified Fe-C single crystals exhibiting anomalously long lattice-spacings [11].

18: HRTEM image and FFT of the MWCNT filling exhibiting anomalously long lattice-spacings [66, 67].

19: Schematic diagram of a boundary layer developing at the leading edge of a plate [82].

20: Schematic diagram of a turbulent lump (eddy) fluctuation u' and mean velocity $\overline{u_x}$ [82].

21: Schematic diagram of the effect of *k* (A) and *d* (B) type roughness in a flow [83].

22: Schematic diagram of the reactor used for the synthesis of the radial structures.

23: Scanning electron micrograph (taken at 20 kV) showing the rough surface of the quartz substrate used for the synthesis of the radial structures.

24: Schematic diagram of the substrate used for flower-like MWCNT structures synthesis.

25: Schematic diagram of a X-ray diffractometer.

26: Schematic diagram of X-rays diffracting from the atomic planes of a crystal.

27: Schematic diagram of the reactor used for the synthesis of the filled-MWCNTs. The geometry and the dimensions of the substrates are also shown.

28: Temperature profile of the first 30 cm of the furnace used for the synthesis of the filled-MWCNTs measured from the starting point of the furnace (0 cm in the profile).

29: Scanning electron micrograph (taken at 20 kV) showing the cross-section of closely packed arrays of partially filled MWCNTs.

30: Transmission electron micrograph (taken at 200 kV) showing a typical example of partially filled MWCNT.

31: Scanning electron micrograph (taken at 20 kV) showing a radial-structure comprising MWCNTs continuously filled with single-crystals of ferromagnetic α-Fe and Fe_3C departing from a central core particle.

32: Scanning electron micrograph (taken at 20 kV) showing many radial-structures near the vapour-flow-facing edge of the substrate used for the MWCNTs deposition.

33: Schematic diagram showing the new substrate geometry used for the preliminary investigations of the radial structures to verify the presence of a local perturbation in the ferrocene/Ar vapour flow.

34: Scanning electron micrograph (taken at 20 kV) showing many radial structures deposited on the vertical surface of the Si/SiO_2 substrate.

35: Scanning electron micrograph (taken at 20 kV) showing a top view of many radial structures deposited on the vertical surface of the Si/SiO_2 substrate.

36: Scanning electron micrograph (taken at 20 kV) showing many radial structures deposited on the top of closely-packed vertical arrays grown on the horizontal surface of the quartz substrate shown in Fig.33.

37: Transmission electron micrograph (taken at 200 kV) showing a typical example of MWCNT (detached from a radial structure) continuously filled for ~ 12 μm.

38: Schematic diagram showing the viscous boundary layer (eddies) created by the vapour-flow-facing edge of the Si/SiO_2 substrate. This viscous boundary layer is responsible of the formation of the radial structures in the vapour. These structures deposit on the vapour-flow-facing edge of the substrate (green area). The average Reynolds number for the ferrocene vapour flow was estimated to be Re=2-4

39: Schematic diagram showing the viscous boundary layer created by the vertical Si/SiO_2 substrate in the geometry shown in Fig.33. This local-perturbation is responsible of the formation of the radial structures that will deposit on the vertical and horizontal surfaces of the Si/SiO_2 and quartz substrates (green areas), as shown in Figs.34-36. The average Reynolds number for the ferrocene vapour flow was estimated to be Re=2-4.

40: HRTEM micrograph of a Fe_3C single-crystal (taken at 200 kV). In the inset, the reciprocal lattice reflections obtained by electron diffraction (SAED) are shown. The forbidden 100 reflections of Fe_3C (between the red lines) correspond to the lattice spacing 0.49 nm. The blue circles indicate the allowed 031 reflections of Fe_3C corresponding to the lattice spacing 0.19 nm. The green circles

indicate the 002 reflection of the graphitic MWCNT walls (lattice spacing of 0.34 nm). The beam direction is [01-3].

41: HRTEM micrograph of a Fe_3C single-crystal (taken at 200 kV). In the inset the reciprocal lattice reflections obtained by electron diffraction (SAED) are shown. The forbidden 010 reflections of Fe_3C (between the red lines) correspond to the lattice spacing 0.66 nm. The blue circles indicate the allowed 200 reflections of Fe_3C corresponding to the lattice spacing 0.24 nm. The beam direction is [001].

42: HRTEM micrograph of a Fe_3C single-crystal (taken at 300 kV). In the inset the reciprocal lattice reflections obtained by FFT (of the area within the red square) are shown. The forbidden 100 reflections of Fe_3C (between the red lines) correspond to the lattice spacing of 0.49 nm, while the forbidden 001 reflections (between the blue lines) correspond to the lattice spacing of 0.44 nm. The beam direction is [010].

43: Low-angle XRD diffractogram and Rietveld refinement (green line) of the filled-MWCNT extracted from the reactor. No peaks are observed at low angle, the large peak corresponds to the (002) planes of the graphitic MWCNT walls. The light-violet line corresponds to the difference between the X-ray diffractogram data (red) and the refinement (green line).

44: XRD diffractogram and Rietveld refinement (green line) from the filled-MWCNT extracted from the reactor. The relative abundance of the phases is 2.0% of γ-Fe cubic (*Fm-3m*), 20.1% of Fe_3C orthorhombic (*Pnma*) and 16.5% of α-Fe cubic (*Im-3m*). The light-violet line corresponds to the difference between the X-ray diffractogram data (red) and the refinement (green line).

45: High resolution scanning TEM image of the Fe_3C single crystal used for the EELS analyses (taken at 80 kV). In the inset the reciprocal lattice reflections, obtained by FFT of the area delimited by the red square, are shown. The forbidden 100 reflections of Fe_3C (between the red lines) correspond to the lattice spacing of 0.51 nm. The blue circles indicate the allowed 011 reflections corresponding to the lattice spacing 0.39 nm. The beam direction is [0-11].

46: Typical EELS spectra of the Fe_3C single crystal from Fig. 45 before (black) and after (blue) the application of the Pearson method. The two step functions are shown with red color.

47: Scanning electron micrograph (taken at 20 kV) of a radial structure comprising radial continuously filled-MWCNTs departing from a central particle (obtained with a flow rate of ~ 11 ccm).

48: Scanning electron micrograph (taken at 20 kV) of another radial structure comprising radial continuously filled-MWCNTs departing from a central particle (obtained with a flow rate of ~ 11 ccm).

49: Schematic diagram of the viscous boundary layer between the rough surface of a quartz substrate and the laminar ferrocene/Ar vapour flow. The vapour flow is dominated by viscous forces which result in non-zero lateral velocity at the tips of asperities and fluctuating, confined eddies.

50: SE micrograph (taken at 20 kV) showing an as grown thick deposit of radial structures.

51: A scanning electron micrograph (taken at 20 kV) showing a distinct vertical-to-radial growth region at smooth-rough quartz substrate boundary: the upper-right region is the top view of a vertical array of filled-multiwall carbon nanotubes

grown perpendicular to the smooth quartz surface, and the lower-left is that of layers of free-standing radial structures on the rough quartz surface.

52: TEM micrograph (taken at 200 kV) showing the cross section of a typical radial structure obtained at a flow rate of ~7 ccm.

53: TEM micrograph (taken at 200 kV) showing the cross section of another typical radial structure obtained at a flow rate of ~ 15 ccm.

54: Transmission electron micrograph (taken at 200 kV) of small particles (diameter ~100 nm) observed in the core of a small radial structure. Inset: selective area electron diffraction pattern obtained from one of the spherical particles. The orange arrows indicate a lattice spacing of 0.25 nm corresponding to the (200) plane of Fe_3C. The blue arrows indicate a lattice spacing of 0.11 nm corresponding to the (303) plane of Fe_3C. The green arrows indicate the spots corresponding to the (002) lattice planes of graphite with spacing 0.33 nm.

55: Transmission electron micrograph (taken at 200 kV) showing more small particles (diameter ~100 nm) observed in the core of a small radial structure.

56: The A-F sequence of transmission electron micrographs (taken at 200 kV) follows a single continuously filled-MWCNT; the filling is continuous for ~9μm. The swelling feature in micrograph F is due to electron beam damage that resulted from the long exposure time needed to complete the sequence.

57: The A-E sequence of transmission electron micrographs (taken at 200 kV) follows a continuously filled MWCNT; the filling is continuous for ~12μm. In the insets (A(i),B(i) and E(i)) the SAED analyses of the filling structure reveal the reflection of orthorhombic Fe_3C. In A(i) and B(i): the turquoise circles indicate

the 112 reflection of Fe_3C, the orange circles indicate the 002, 004 and 006 (visible only in A(i)) reflections of the MWCNT, the yellow circles (in A(i)) indicate the 120 and 240 reflections of Fe_3C. In E(i) only the 240 reflection of Fe_3C (indicated with the blue circles) is observed.

58: Transmission electron micrograph (taken at 200 kV) showing a radial structure obtained at vapour flow rates of 15 ccm. The core (agglomeration of spherical nanoparticles) clearly exhibits an elongated shape.

59: Transmission electron micrograph (taken at 200 kV) showing another radial structure obtained at vapour flow rates of 15 ccm. The core (agglomeration of spherical nanoparticles) presents a straight and elongated shape with a length of ~ 5 μm.

60: Transmission electron micrographs (taken at 200 kV) showing in A the elongated core (agglomeration of spherical nanoparticles) of a radial structure obtained at vapour flow rates of 20 ccm. In B a high detail of the core particles-agglomeration is shown.

61: Transmission electron micrograph (taken at 200 kV) showing a continuously filled MWCNT. The MWCNT was detached from a radial structure obtained at vapour flow rates of 20 ccm.

62: Schematic diagram showing the effect of higher vapour flow rates of 15-20 ccm in the confined eddies. The shape of the core particles suggests that at these flow rates the eddies are not confined. This schematic diagram could explain the elongated shape of the core (particles agglomeration) of the radial structures obtained at vapour flow rates of 15-20 ccm.

63: Typical X-ray diffractogram data (red), and Rietveld refinement (green line), of the 002 graphitic carbon reflection obtained from a powder comprising filled nanotube material grown on a smooth quartz surface (A) and from powder comprising radial structures prepared under identical reaction conditions (B). Clearly (B) shows two proximate peaks; the lower angle peak (1) corresponds to the 002 reflection from multiwall carbon nanotube walls observed in (A). This feature corresponds to the 0.34 nm lattice spacing directly observed in selective area diffraction studies of individual filled nanotube (Fig.57), namely the 002 reflection from graphite space group *$P6_3/mmc$* (ICSD Chemical Database Ref. 53781). The second graphitic peak (2) corresponds to the lattice spacing of 0.33 nm (002 peak of graphite hexagonal *$P6_3/mmc$*, ICSD Chemical Database 52230) of the graphitic shell of the spherical particles as observed in the selective area diffraction pattern in Fig.54 (inset). The light-violet line corresponds to the difference between the X-ray diffractogram data (red) and the refinement (green line).

64: Typical X-ray diffractogram data (red), and Rietveld refinement (green line) for powder of radial structures obtained with an vapour flow rate of 3.5 ccm. The relative weight abundance of the encapsulated phases are 3% cubic γ-Fe (*Fm-3m*, Crystal Open Database Ref. 9008469), and 12% of cubic α-Fe (*Im-3m*, Crystal Open Database Ref. 1100108) and 18 % of orthorhombic Fe_3C (Crystal Open Database Ref. *Pnma* 16593). A 17% weight abundance of Fe_3O_4 (cubic, space group *Fd3-mz,* Ref. 65338 ICSD) results from spontaneous oxidation of non-encapsulated Fe particles when the powder is handled in air. The light-violet line corresponds to the difference between the X-ray diffractogram data (red) and the refinement (green line).

65: Typical X-ray diffractogram data (red), and Rietveld refinement (green line) for powder comprising radial structures obtained with a vapour flow-rate of 20 ccm. The relative weight abundance of the phases are 2% cubic γ-Fe (*Fm-3m*), and 28% of cubic α-Fe (*Im-3m*). A 26% weight abundance of Fe_3O_4 (cubic, space group *Fd3-mz*) results from spontaneous oxidation of non-encapsulated Fe particles when the powder is handled in air. The light-violet line corresponds to the difference between the X-ray diffractogram data (red) and the refinement (green line).

66: Schematic of the proposed growth mechanism of the radial structures.

67: Schematic diagram of the substrate used for the production of flower-like structures indicating the direction of vapour flow, dimensions of the hole, and the growth region.

68: Scanning electron micrographs (taken at 20 kV) of un-annealed flower-like structures in the growth area. A and B show a front-view and top-view (respectively) of individual flower-like structures, C shows a top-view of many flower-like structures.

69: Scanning electron micrograph (taken at 20 kV) of un-annealed flower-like structures in the growth region at low magnification. The length of the growth region is ~ 10 mm.

70: Scanning electron micrograph (taken at 20 kV) of un-annealed flower-like structures showing another part of the growth region at low magnification.

71: Scanning electron micrograph (taken at 20 kV) of un-annealed flower-like structures in the growth region of the substrate. In some cases the flower-like structures are found with an higher degree of alignment.

72: Schematic diagram of the quartz substrate cross-section and ferrocene/Ar vapour flow.

73: Growth mechanism of the flower-like structures. The black solid lines represent the islands of C atoms formed in a spherical homogeneously nucleated particle (1) that assumes a cap-like shape after contact with the substrate. Carbon caps will start to grow from carbon-islands formed in the homogeneously nucleated particle (stage 2-3) leading to carbon nanotube growth (stage 4).

74: Schematic diagram of the new substrate geometry used for the production of the flower-like structures.

75: Scanning electron micrograph (taken at 20 kV) showing the new substrate geometry and diameter of the vapour flow-facing edge.

76: Scanning electron micrograph (taken at 20 kV) of un-annealed flower-like structures in the new substrate.

77: Scanning electron micrograph (taken at 20 kV) showing the homogeneity of the flower-like structures grown in the new substrate.

78: Scanning electron micrograph (taken at 20 kV) showing another region of growth of the flower-like structures grown in the new substrate.

79: Scanning electron micrograph (taken at 20 kV) showing the high homogeneity of the flower-like structures in a top-view of a larger area.

80: Scanning electron micrograph (taken at 20 kV) showing flower-like structures obtained with lower sublimation rate of ferrocene (~140 °C in 1 min and 45 sec).

81: Scanning electron micrograph (taken at 20 kV) showing the variable homogeneity of flower-like structures growth when a lower sublimation rate of ferrocene is used. The violet arrow indicates a single flower like structure.

82: Scanning electron micrograph (taken at 20 kV) showing in a top view the lower homogeneity of flower-like structures growth when a lower sublimation rate of ferrocene is used.

83: Scanning electron micrographs (taken at 20 kV) showing in A and B the open growth-mechanism of the flower-like structures.

84: Scanning electron micrographs (taken at 20 kV) showing in A and B two more examples of the open growth-mechanism of the flower-like structures.

85: XRD diffractogram obtained from the un-annealed flower-like structures mechanically removed from the growth area in Fig.62C. The Rietveld refinement is indicated by the green line. The light-violet line corresponds to the difference between the X-ray diffractogram data (red) and the refinement (green line).

86: XRD diffractogram of the flower-like structures obtained after annealing for 13 h at 500ºC. The Rietveld refinement is indicated by the green line. The light-violet line corresponds to the difference between the X-ray diffractogram data (red) and the refinement (green line).

87: XRD diffractogram of the flower-like structures after annealing for 15 h at 500 ºC. The Rietveld refinement is indicated by the green line. The light-violet line corresponds to the difference between the X-ray diffractogram data (red) and the refinement (green line).

88: A backscattered electron and a secondary electron micrographs of the flower-like structures removed from the substrate after annealing for 13h. A shows (bright regions) the continuous single crystals filling the MWCNTs. B shows the SE image (taken at 20 kV) of the same area. It is also possible to observe some Fe_3O_4 nanoparticles resulting from oxidation of Fe particles (non-encapsulated inside the nanotubes) when the powder is handled in air.

89: Transmission electron micrograph (taken at 200 kV) showing typical MWCNTs continuously filled with α-Fe (obtained after 15 h of annealing) with the selective area electron diffraction taken from the area indicated by the blue arrow.

90: Transmission electron micrographs (taken at 200 kV) showing a region of a MWCNT continuously filled for approximately 19 μm.

91: Transmission electron micrographs (taken at 200 kV) showing another region of a MWCNT continuously filled for approximately 19 μm.

92: Transmission electron micrographs (taken at 200 kV) showing another MWCNT continuously filled for approximately 13 μm obtained after 15 h of annealing.

93: Scanning electron micrograph (taken at 20 kV) showing α-Fe2O3 particles on filled MWCNTs structures owing to the oxidation process after 15 h of annealing at 500 °C.

94: The field dependence of dc magnetization at T=5 K of as-produced powder of radial structures for two values of the laminar vapour flow rate. The relative weight abundance for the powder produced with a flow rate of 3.5 ccm was 3% γ-Fe, 12% α-Fe, 18% Fe_3C, 17% Fe_3O_4, and 50% C (see Fig.64). The relative

weight abundance for the powder produced with a flow rate of 20 ccm was 2% γ-Fe, 28% α-Fe, 26% Fe_3O_4, and 44% C (see Fig.65).

95: Temperature dependence of field-cooled dc magnetization under the applied magnetic field of 10 kOe (powder produced with a flow rate of 3.5 ccm).

96: Temperature dependence of field-cooled dc magnetization under the applied magnetic field of 1 kOe (powder produced with a flow rate of 3.5 ccm).

97: Temperature dependence of field-cooled dc magnetization under the applied magnetic field of 0.1 kOe (powder produced with a flow rate of 3.5 ccm).

98: Hysteresis loop at 5 K of the powder containing the flower-like structures annealed for 13 h (X-ray diffractogram previously shown in Fig.86). In this case also the diffraction peaks of the ferromagnetic Fe_3O_4 nanoparticles were included in the quantitative analysis.

Introduction

The challenge

Since the first observations by LV Radushkevich [1] in 1952, by M Endo and A Oberlin [2] in 1976, and the significant contributions of S Iijima in 1991 [3-4], carbon nanotubes (CNTs) have attracted the attention of many research groups owing to their outstanding physical properties. The small size, large aspect ratio, high elasticity, and high chemical stability render these nanostructures ideal systems which can be used as containers in the nanometre scale to accommodate a desired material. The carbon shells provide an effective barrier against oxidation, protecting the accommodated material from the external environment and ensuring long-term stability. In the last decade CNTs have been filled with different kinds of materials: metals, semiconductors, organic materials, therapeutic drugs, salts, etc. A great attention has been focused on the possibility of filling CNTs with the transition metals Co, Fe and Ni. In particular, the possibility of filling nanotubes with ferromagnetic single-crystals of α-Fe has been investigated for many years owing to the desirable magnetic properties that these materials would possess when accommodated inside CNTs. Very long (many micrometres) and thin (single magnetic domain diameter ~10-40 nm) α-Fe single crystals could display exceptional properties of saturation magnetization (~220 emu/g) and of coercivity (higher than 2000 Oe) [5-9]. The achievement of

these exceptional magnetic properties requires a control of the dimensions and of the phase composition of the single crystals involved in the growth of the CNTs.

The challenge of this project is the continuous filling of ferromagnetic single crystals of α-Fe in multiwall carbon nanotubes.

These ferromagnetic systems can be ideal candidates for many magnetic applications. For example as nanoscale containers for biomedical diagnosis, therapy, and monitoring, due to the high mechanical resistance and to the heat dissipation generated by the reversal of the magnetic moment direction in the presence of an alternating magnetic field. These structures also have potential applications in magnetic data recording for quantum disk fabrication, or as probes for magnetic force microscopy. In the last decade conventional chemical vapour deposition (CVD) methods have been developed in the attempt to guarantee the growth of multiwall carbon nanotubes (MWCNTs) continuously filled with α-Fe through the sublimation and pyrolysis of a ferrocene vapour in a steady-state Ar flow. The formation mechanism of the MWCNTs is generally based on vapour-, liquid-, and solid-phase chemistry and catalysis models. These mechanisms are controversial but the most widely-accepted general features can be stated as follows: i) at elevated temperature (i.e. 750-1000 ºC) there is exothermic catalytic decomposition of hydrocarbons at the surface of the transition metal nanoparticles. These nanoparticles are assumed to be in liquid-state, ii) the carbon species dissolve into the metal nanoparticle until the solubility limit at that temperature is reached and a metastable metal-carbide phase is formed iii) the metal-carbide phase decomposes and the carbon precipitates on the surface crystallize endothermically into energetically stable graphitic carbon, iv) alternatively, a high carbon flux at the nanoparticle surface can also result in

graphitic shell formation (endothermic process), and v) the temperature gradient created by the exo- and endo-thermal processes drives the flow of dissolved carbon in the particle as described before. Despite the numerous studies, the synthesis of MWCNTs filled with continuous single crystals of α-Fe is still difficult to achieve. The reason can be found in the steady-state conditions that do not guarantee a continuous delivery of the Fe-species to each MWCNT and in the presence of multiple Fe-based phases (Fe_3C, γ-Fe, α-Fe) that are involved in the MWCNTs growth. Previous reports stated that continuous filling can be achieved by using high sublimation rates of ferrocene [10], however these statements were contradicted by other recent publications [7,8], showing that with conventional CVD only filling rates of ~ 40% are achievable and the limiting factor is related to the stoichiometry of each ferrocene molecule containing 10 atoms of C and only 1 atom of Fe [7,8]. The presence of other magnetic Fe-based (Fe_3C and γ-Fe) phases involved in the MWCNTs growth together with α-Fe represents another important issue for achieving the single crystals continuity [11-17]. Since the formation of Fe_3C is fundamental for the MWCNTs growth, it would be difficult to avoid the formation of this phase [11,15]. A similar consideration can also be made for the γ-Fe phase, which is generally observed near the cap of the MWCNT owing to the pressure applied by MWCNT walls on the filling [7,13,14]. The presence of other unknown Fe-C based phases inside the MWCNTs, together with the phases mentioned above (α-Fe, γ-Fe, Fe_3C), also represents an additional problem in the achievement of the continuous α-Fe filling [11,17].

Scope of the project and preliminary strategy

CNTs can be filled in-situ during the synthesis process or through subsequent opening, filling and closing. In this thesis the attention will be focused only on the in-situ filling process. In this process a particular family of compounds, known as metallocenes (M-$(C_5H_5)_2$ with M = transition metal) is used. These compounds contain the C and M elements in a fixed ratio of 1:10 and are usually used for in-situ synthesis of CNTs owing to the convenient temperature range for sublimation and thermal decomposition. The most common metallocenes ferrocene, cobaltocene and nickelocene contain the transition metals Fe, Co and Ni. These metals can easily form metastable carbides and catalyse CNT growth in vapours containing high quantities of carbon (owing to the solubility of carbon in the metal). The growth of CNTs is induced by a self-organization process of the carbon and metal species that results from the decomposition of the metallocene. In this process the growth and the filling of the CNT are simultaneous.

The goal of this project consists in finding and developing new reproducible-methods that can allow the synthesis of MWCNTs continuously filled with single crystals of ferromagnetic α-Fe with uniform α-Fe/MWCNTs-wall interfaces and a diameter in the order of that of a single magnetic domain (~ 66 nm).

As explained above, the achievement of a continuous α-Fe filling of the MWCNT core is complicated mainly by the stoichiometry of the ferrocene compound, and by the steady state conditions of the ferrocene/Ar vapour flow, which does not guarantee a continuous delivery of the Fe-species to each MWCNT.

To understand how to solve this problem, a preliminary strategy would consist of increasing the concentration of Fe in the pyrolysing vapour, using a larger

quantity of ferrocene (60-100 mg with a synthesis time of ~ 4 min) with respect to what is generally used in literature (i.e. 6 mg/min with a synthesis time of 10 min [11,17]), high sublimation rates (sublimation temperatures of 180- 260ºC [10,11,17]), high pyrolysis temperatures (i.e. ~1000 ºC [7,10,11]) and lower flow rates of Ar (~ 12 cubic centimetres per minute, i.e. 25 standard cubic centimetres per minute) with respect to those previously reported in literature (100-300 standard cubic centimetres per minute) [10,11,17]. In these conditions the pyrolysed ferrocene vapour would contain a very high concentration of Fe and C. The effect of a very high concentration of Fe in the MWCNT-filling process will be investigated. Once the continuous filling of the MWCNTs is achieved, the second step will consist in controlling the composition of the Fe-based phases (α-Fe, γ-Fe, Fe_3C, unknown Fe-C phases) involved in the MWCNT growth and achieve a single phase filling of α-Fe. According with the Fe-C diagram, bulk γ-Fe decomposes into α-Fe and Fe_3C below 727 ºC, and bulk Fe_3C decomposes into α-Fe and graphitic carbon when is in contact with graphite [18,19] .The maximum decomposition rate of Fe_3C has been reported to be in the temperature range 500-550 ºC [19]. Previous reports of post-synthesis annealing of MWCNTs partially filled with single crystals of Fe_3C, α-Fe and γ-Fe have shown that annealing for 15-20 hours at 645 – 675 ºC in Ar/H_2 or in Ar can allow to achieve a single-phase α-Fe filling [7,8]. However the decomposition rate of the unknown Fe-C phases previously observed in literature has not been reported [11]. If these phases will be observed inside the MWCNTs, more investigations will be performed to understand their origin and the decomposition rate during the annealing process.

Thesis outline

Chapter 1 introduces the Fe-filled MWCNT field, listing the conventional methods that are generally used to synthesize MWCNTs filled with Fe-based single crystals of Fe_3C, γ-Fe and α-Fe and showing the limits of these conventional methods in the achievement of the continuous filling. The concepts of heterogeneous nucleation are also introduced to explain the models of the MWCNT growth mechanism previously reported in literature. The concepts of homogeneous nucleation are also outlined. This chapter summarises also the magnetic properties and applications of the MWCNTs filled with Fe_3C, γ-Fe and α-Fe single crystals, showing the effect of annealing on the MWCNT filling. The previous reports related to the Fe-C phases with unknown lattice spacings are also described. A brief description of the theory behind chemical vapour synthesis (CVS), perturbed flow, eddy viscosity, and surface roughness is also given. These concepts will be useful to completely understand the results and discussion section in Chapter 3. Chapter 2 describes the experimental methods that are used for the MWCNTs synthesis and characterization. The first part of this chapter is focused on a detailed explanation of the CVS and CVD systems used in the new synthesis approaches. The second part describes the main techniques used for the characterization of the MWCNTs. These include the structural characterizations with X-ray diffraction and electron diffraction, morphological analyses with electron microscopy, chemical analyses with electron energy loss spectroscopy, and magnetic-structure characterization with magnetometry.

Chapter 3 is focused on the main findings of this project and is divided in four main parts.

The first part shows the preliminary results obtained with the steady state CVD approach and describes how, the first serendipitous observation of new radial structures comprising radial MWCNT continuously filled with Fe-based single-crystals allowed the development of two new synthesis approaches: ‘‘ boundary layer chemical vapour synthesis’’ (CVS) and ‘‘locally perturbed chemical vapour deposition’’. The second part reveals the origin of the anomalously long lattice spacings that were previously reported in literature and wrongly associated to unknown structures inside the MWCNTs. The third part is dedicated to the new syntheses approaches based on the creation of a local perturbation in a laminar ferrocene vapour flow. The new approaches and the new structures observed as synthesis products are shown in detail. The fourth part shows the magnetic properties of the new structures obtained with these new synthesis methods. The approximated critical diameter size with which a single crystal of α-Fe can be considered a single magnetic domain is also compared to the diameter of the observed α-Fe single crystals that continuously fill the MWCNTs obtained with the new synthesis methods. Chapter 4 summarises the final conclusions of this project. Chapter 5 suggests possible new experiments that could be done in the future with these new syntheses approaches.

Chapter 1

Literature review and background

1.1 Lattice configuration of multiwall and singlewall carbon nanotubes

The lattice configuration of multiwall and singlewall carbon nanotubes (SWCNT) can be qualitatively envisioned in Fig.1. and Fig.2. SWCNT can be visualized by rolling up a single graphene sheet (single layer of carbon atoms) to form a hollow cylinder, while MWCNT can be visualized by rolling up more layers of graphene sheets to form concentric cylinders. SWCNTs are characterized by a wrapping (chiral) vector $\mathbf{C_h} = n\mathbf{a_1} + m\mathbf{a_2}$, where $\mathbf{a_1}$ and $\mathbf{a_2}$ are the graphitic Bravais lattice vectors, **T** is the translational vector and n and m are integers. The chiral angle θ is that between $\mathbf{a}_1$ and $\mathbf{C_h}$. The Chiral vector $\mathbf{C_h}$ defines the circumference of the nanotube and different values of n and m allows to obtain different SWCNT structures. For zigzag SWCNT $\theta = 0^o$ and for armchair SWCNT $\theta = 30^o$ [20] (see Fig.1 and Fig.2). In the case of a MWCNT, a turbostratic stacking of graphene sheets has been suggested [21]. It was reported that the wide d_{002} spacing is due to the fact that neighboring graphitic sheets are parallel to each other, but translational and rotational correlations within a sheet plane are random.

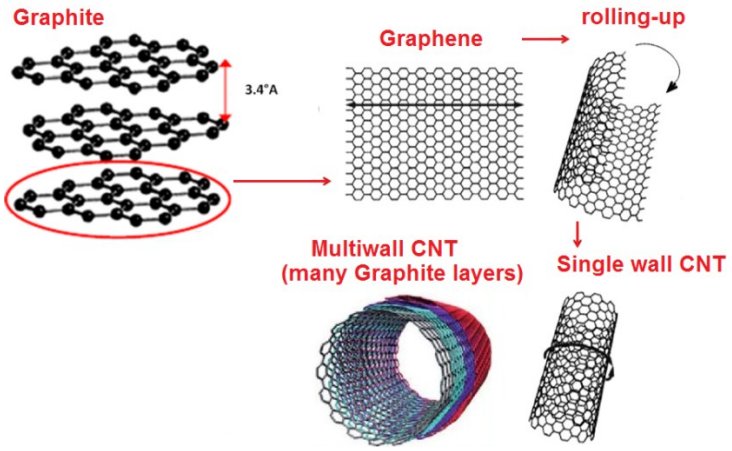

Fig.1: Atomic structure of single wall and multiwall carbon nanotubes.

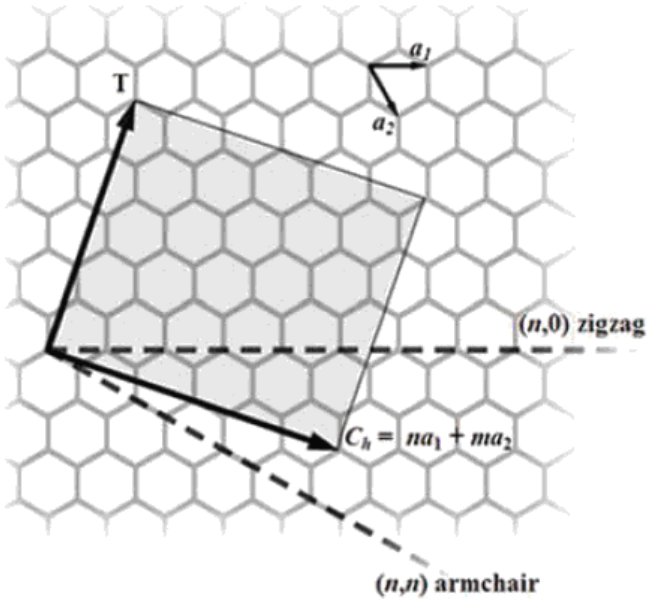

Fig.2: Lattice configuration of singlewall carbon nanotubes [20].

1.2 Chemical vapour deposition of transition-metal filled carbon nanotubes

Chemical vapour deposition is a process that involves the formation of a thin solid film on a substrate by a chemical reaction of vapour-phase precursors [22]. The reaction can be initiated by heat (in thermal CVD), UV radiation (photo-assisted CVD) or plasma (plasma enhanced CVD) [22]. This process can be distinguished from the physical vapour deposition which instead, involves only physical processes in which a material is vaporized from a solid or a liquid source into atoms and molecules and transported (through a vacuum environment) to a substrate, where it condenses [22]. CVD is one of the most common methods used to produce large quantities of carbon nanotubes (CNTs), with acceptable quality [23]. CNTs can be synthesized as empty nanotubes, or they can be filled with single crystals of elemental phases, alloys, or carbides of transition metals. The processes used for the synthesis of empty and filled nanotubes are similar; indeed in both cases hydrocarbon compounds are required as a precursor necessary to deliver the carbon for the growth of the CNTs. In the particular case of empty nanotubes, the catalyst is generally located on a substrate and the hydrocarbons (i.e. methane or others) are delivered through a carrier gas (N_2 or Ar) in a reaction zone (see Fig.3), and decomposed at high temperatures (700-1000 ºC) [10].

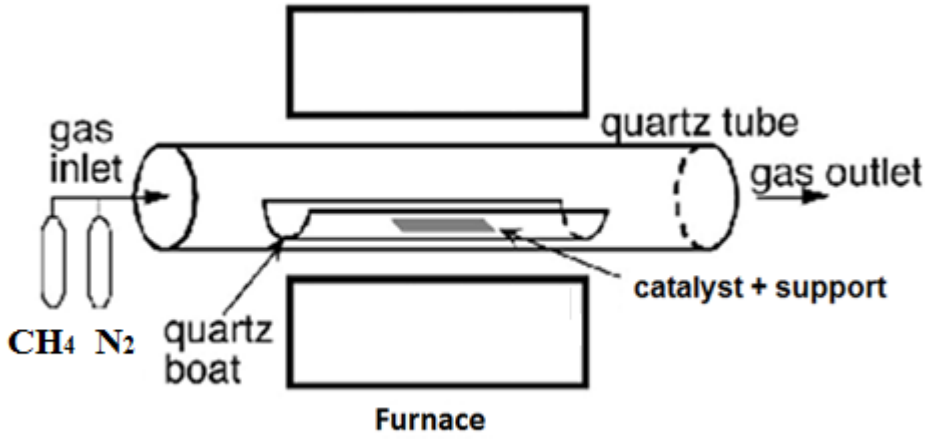

Fig.3: Setup of CVD system for the growth of empty nanotubes.

In the case of metal filled MWCNTs, different compounds are used as precursors [5-17,24]. These compounds are known as metallocenes and contain both metal and carbon generally in a ratio 1:10. Ferrocene is the metallocene that is generally used in the synthesis of MWCNTs filled with α-Fe (see Fig.4). Metallocenes have a sandwich-like molecular structure with the metal in the centre and two cyclopentadienyl rings as ligands [24]. Since they possess a convenient temperature range for sublimation and decomposition, is possible to use these compounds as precursors for the synthesis of metal-filled MWCNTs.

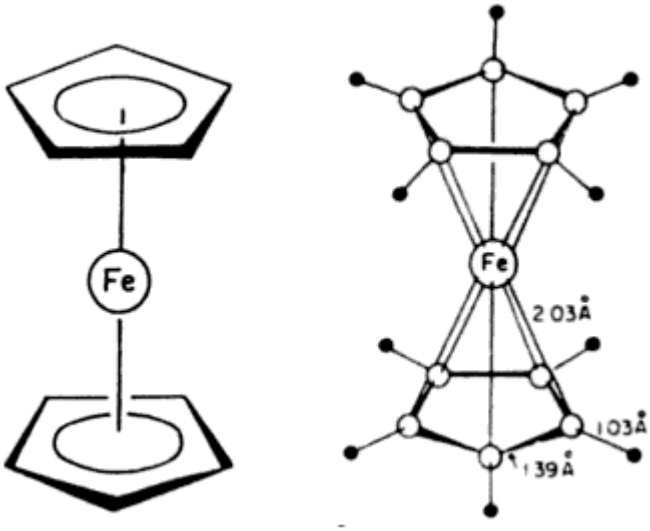

Fig.4: Sandwich-like molecular structure of ferrocene [25].

Metal-filled MWCNTs are conventionally produced by two main CVD methods: solid-source CVD (SSCVD) [5-7,10,11,24,26] and liquid-source CVD (LSCVD) [5,8,9,12,24,26,27]. In the case of SSCVD a solid material (ferrocene or other metallocenes) is used as precursor; in LSCVD, the precursor is liquid and consist of a hydrocarbon (benzene, toluene, etc.) in which the metal catalyst compounds (often metallocenes) are dissolved [5,8,9,12,24,26,27]. In both cases a horizontal quartz tube and a two zone furnace is generally used. However, owing to the high excess of carbon produced during the reaction, LSCVD is not suitable for the growth of MWCNTs filled with continuous single-crystals of α-Fe. Previous reports have shown that the excess of carbon will predominantly favour the growth of hollow carbon nanotubes filled with small Fe_3C particles. A typical setup for the SSCVD system can be observed in Fig.5.

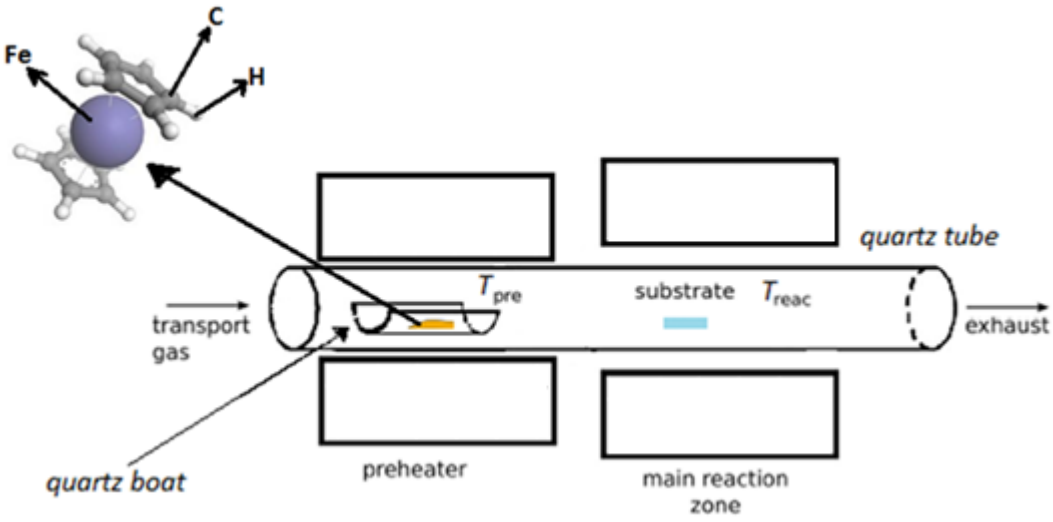

Fig.5: Setup for solid source CVD system.

The metallocene powder is placed in a quartz boat, inside a quartz tube, and is sublimated (preheater zone) at a specific temperature that depends by the compound that is used. Once is sublimated, the metallocene vapour is transferred into the main reaction zone by a controlled flow of a gas carrier (generally Ar or N_2). In the main reaction zone the decomposition of the metallocene and the growth of metal filled MWCNTs will occur. In particular, it was proposed that from temperatures around 550 °C metallocenes start to decompose into metal and hydrocarbons components (1) [24]:

$$M(C_5H_5)_2 \rightarrow M + H_2 + CH_4 + C_5H_6 + \ldots \qquad (1)$$

The choice of the sublimation temperature is critical, because it regulates the control the sublimation rate of the metallocene transferred in the reaction zone. For the growth of Fe-filled MWCNTs the reaction temperature is generally varied

between 750°C and 1100°C. The deposition occurs in every part of the inner wall of the quartz tube, however the attention is always focused on the isothermal zone, where control of CNT growth can be achieved. Silicon substrates with an upper thin SiO_2 layer and a thin metal layer on the top of the oxide layer are commonly used in the synthesis processes. Previous reports showed that SiO_2 inhibits Fe from silicidation [28,29]. In particular in the work of Jung *et al.* a prepaterned Si/SiO_2 substrate was used for CVD growth of CNTs using an Fe catalyst [29]. The authors succeeded in growing nanotubes only on the SiO_2 regions, while on pure Si, only stable $FeSi_2$ and Fe_2SiO_4 were detected. In some cases a metal layer is deposited by sputtering on the top of the substrates and is considered as promoter for the CNTs growth [7,10].

1.3 Homogeneous versus heterogeneous nucleation

1.3.1 Homogeneous nucleation

The formation of particles in a vapour is often explained through ‘‘homogeneous gas phase nucleation’’ [22,30]. Classical theories of homogeneous nucleation of particles in a CVS vapour are based on the idea that, when a vapour is supersaturated, there is a critical particle size over which the particle-formation and growth is stable. Particles smaller with respect to that size tend to evaporate, while particles with larger size tend to grow. The overall excess free energy (see equations (2) and (3)) necessary to form a stable crystal nucleus is equal to the sum of the surface excess free energy (ΔG_s) and the volume excess free energy (ΔG_V).

$$\Delta G = \Delta G_s + \Delta G_V \quad (2)$$

In the case of the formation of a spherical liquid droplet in a supersaturated vapour, the previous equation can be written as shown in equation (3):

$$\Delta G = 4\pi r^2 \gamma + \frac{4}{3}\pi r^3 \Delta G_v \qquad (3)$$

Where γ is the surface energy of the droplet per unit area, ΔG_v is the free energy change of the transformation per unit of volume, and *r* the radius of a spherical droplet. The two terms on the right side of equation (3) are of opposite sign and depend differently on *r*. ΔG_s is a positive quantity and its magnitude is proportional to r^2. In a supersaturated vapour or solution, G_V is a negative quantity proportional to r^3.

The overall excess free energy of formation (ΔG) passes through a maximum as shown in Fig.6. This maximum value corresponds to a critical nucleus of radius r_c. This can be obtained by setting $\frac{d\Delta G}{dr} = 0$, as shown in equation (4):

$$\frac{d\Delta G}{dr} = 8\pi r\gamma + 4\pi r^2 \Delta G_v = 0 \qquad (4)$$

This can be observed in Fig.6

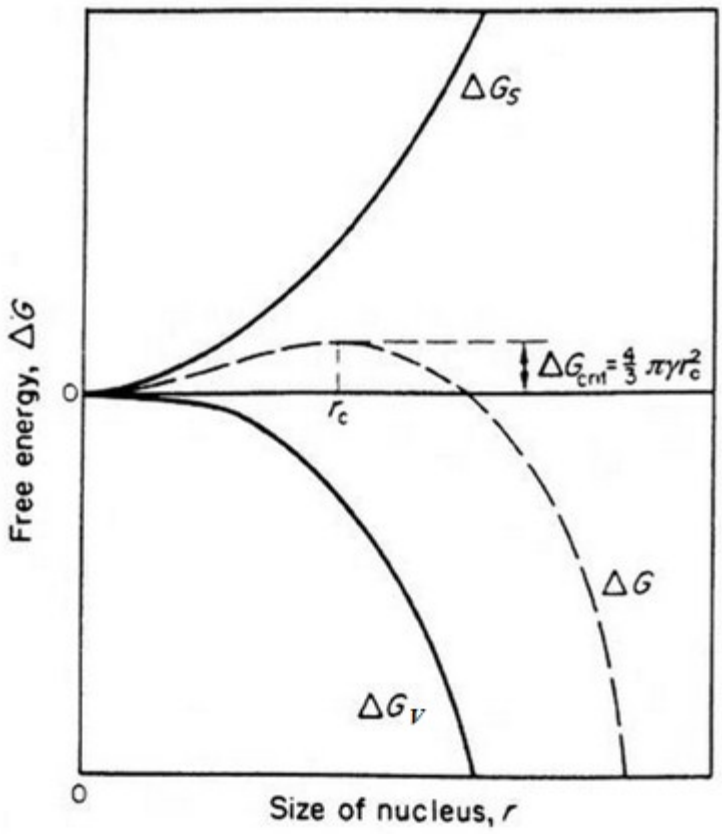

Fig.6: Thermodynamic potential barrier of nucleus formation in the case of homogeneous nucleation [30].

Once a nucleus achieves a radius bigger than r_c further transformations results in a continuous decrease of the free energy, so the process will become spontaneous. The radius *r* of a droplet can be obtained by equation (5):

$$r = \frac{-2\gamma}{\Delta G_v} = \frac{2\gamma v}{\mathbf{k}T\ln S} \qquad (5)$$

Where $\ln S = \frac{2\gamma v}{\mathbf{k}Tr}$, T is the absolute temperature, **k** is the Boltzmann constant, v is the molecular volume, and *S* refers to the supersaturation of the system.

The overall excess free energy for the nucleus formation will be then given by equation (6):

$$\Delta G_{crit} = \frac{16\pi\gamma^3 v^2}{3(\mathbf{k}T\ln S)^2} \qquad (6)$$

This equation gives a measure of the excess free energy in terms of supersaturation of the chosen system.

1.3.2 Heterogeneous nucleation

Heterogeneous nucleation is usually observed in conventional CVD methods used for the film-growth [31]. In this process, the atoms of the nucleating-metal (nucleus) attach to the substrate surface, and the nucleus grows atom by atom [31]. Conventionally this nucleation process is described with the concept of contact angle between the nucleus in the shape of a spherical cap and the substrate

(see Fig.7). With this definition, the free energy of formation of a heterogeneous nucleus (ΔG^{het}) of critical radius is given by equation (7) [31]:

$$\Delta G^{het} = a_3 r^3 \Delta G_v + a_1 r^2 \gamma_{vf} + a_2 r^2 (\gamma_{fs} - \gamma_{sv}) \qquad (7)$$

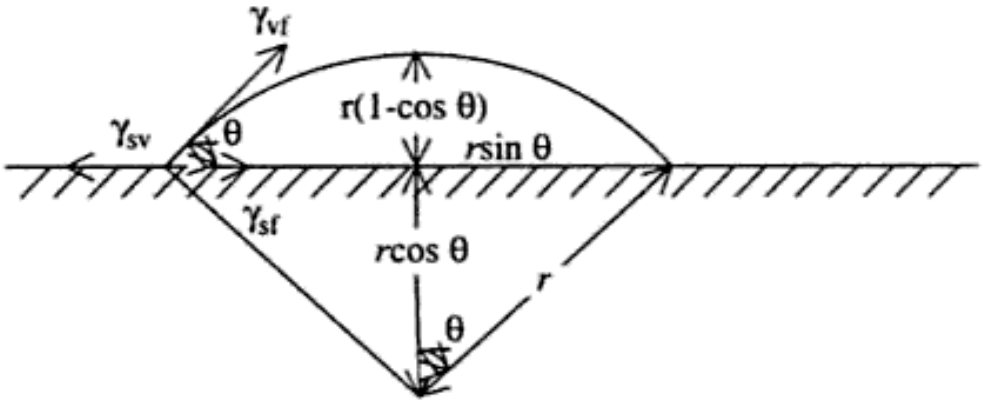

Fig.7: Schematic diagram of the heterogeneous nucleation.

Where *r* is the mean curvature of the nucleus, , ΔG_v is the free energy change of the transformation per unit of volume, and $\gamma_{vf}, \gamma_{fs}, \gamma_{sv}$ are the surface or interface energy of vapour nucleus, nucleus-substrate, and substrate-vapour interfaces and a_1,a_2 and a_3 are geometrical constants defined by equations (8), (9) and (10) [31].

$$a_1 = 2\pi(1 - cos\theta) \qquad (8)$$

$$a_2 = \pi sin^2\theta \qquad (9)$$

$$a_3 = 3\pi(2 - 3cos\theta + cos^2\theta) \qquad (10)$$

Where θ is the contact angle that depends only on the surface properties or interfaces involved. This is defined by the Young equation (equation (11)):

$$\gamma_{sv} = \gamma_{fs} - \gamma_{vf} cos\theta \qquad (11)$$

Similarly to the homogeneous nucleation, the formation of a new phase results in a reduction of the volume free energy, but in an increase in the total surface energy. The nucleus is stable only when its size is larger than the critical size r_c, as shown in equation (12).

$$r_c = \frac{-2(a_1\gamma_{vf}+a_2\gamma_{fs}-a_2\gamma_{sv})}{3a_3\Delta G_v} \qquad (12)$$

The presence of the substrate surface in heterogeneous nucleation decreases the work required to create a critical nucleus and increases locally the probability of nucleation. As shown in equation (11) and equation (13) the contact angle is determined by the interactions between the surface and the molecules of the nucleus.

$$\frac{\gamma_{fs}-\gamma_{sv}}{cos\theta} = \gamma_{vf} \qquad (13)$$

The work of formation for heterogeneous nucleation is substantially reduced compared to that for a homogeneous nucleation process. Attractions (between the surface and the molecules) that are stronger than those between the molecules in the nucleus will lead to a small θ as the nucleus spreads in a thin droplet to maximize the contact area with the surface. If the surface tends to repel the

molecules, then the nucleus is pushed away from the surface, resulting in a contact angle major than 90 degrees [31,32]. This can be observed in equation (14):

$$\Delta G^{het} = \Delta G^{hom}\phi \quad (14)$$

Where ϕ is the ratio between the heterogeneous and homogeneous nucleation mechanism contribution and is defined as: wetting factor. Considering the interaction between molecules with a perfectly planar substrate, this interaction can be expressed with the following equation (equation (15)) [32].

$$\frac{\Delta G^{het}}{\Delta G^{hom}} = \phi = \frac{1}{2} - \frac{3}{4}cos\vartheta + \frac{1}{4}cos^3\vartheta \quad (15)$$

So if the nucleus wets the substrate completely (with θ=180 degrees) G_{het}=G_{hom}; when the contact angle θ= 90 degrees, G_{het}= 1/2G_{hom}, and the smaller the contact angle θ, the smaller the value of the activation energy for nucleation, which will be zero for θ = 0. The role of the surface is, therefore, to provide a constant wetting angle through smoothness on the scale of the nanoscale product and inert, invariant surface chemistry over the desired area. The liquid metal-catalyst particles will then assume a non-spherical shape after wetting on a surface.

Metal particles heterogeneously nucleated from a pyrolyzed-ferrocene vapour, have generally a diameter in the order of 10 nm and can act as a catalyst for the CNT growth.

1.4 The role of nucleation and growth in the growth-mechanism of carbon nanotubes

In the last decade intensive studies were performed in order to find the growth-mechanism of CNT [33-54]. It seems clear that the process of CNT growth starts from the decomposition of hydrocarbons on metal-particles surfaces, followed by the diffusion of carbon species into the metal particles. The first observations of carbon filament growth process was reported *in-situ* by Baker *et al.* [46]. This was done by installing a gas-reaction cell in the transmission electron microscope (TEM) specimen chamber. Filament growth was then performed in a temperature range of 600–1200 ºC at different gas pressures [46], while the TEM column was maintained at sufficiently low temperature and pressure suitable for electron microscopy. The experiment showed that in the case of acetylene decomposition on nickel catalyst at 600 ºC, the metal particles changed shape and moved up with a trail of carbon deposit of 30–50 nm diameter. These observations underlined the liquid status of the catalyst particle during carbon filament growth. In previous literature reports [33-54] many models have been developed to describe the role of nucleation in the CNT growth-mechanism. However the interpretation of the nucleation-process remains controversial and no models of nanotube-nucleation from homogeneously nucleated particles are reported. A three stages growth-mechanism model was proposed by Baker *et al.*[46]. The first stage involves the decomposition of the hydrocarbon on the front of the surface of the metal particles, generating hydrogen and carbon that will dissolve into the metal. Furthermore, the dissolved carbon will diffuse through the volume of the particle and will be deposited on the trailing face, forming the filament (second stage). From this stage, the particle can remain anchored to the

substrate, this synthesis mode is called “base-growth”, or can lift off the substrate, in this case will be observed on the top of the filament (tip growth mode). The difference of growth mode is often explained in terms of adhesion force between the catalyst-particle and the substrate. Indeed a weak contact with the substrate favours the tip-growth mechanism, while a strong interaction promotes the base-growth (see Fig.8). The base- and tip- growth stages shown in this model have the crucial role of enabling the formation of the nanotubes after the nucleation on the heterogeneously nucleated particles. However in this model is not possible to explain in detail the role of nucleation in the CNT growth mechanism.

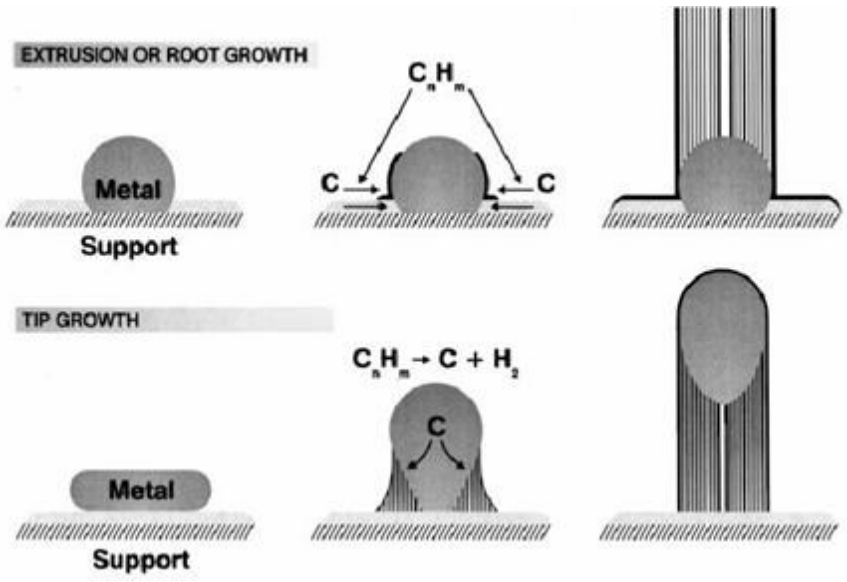

Fig.8: Base and tip growth mechanisms of carbon filaments [16].

In 2005 and 2003 the research works reported by J Y Raty *et al.*[41] and Anna Moisala *et al.* [35] proposed two mechanism of nanotube nucleation from heterogeneously nucleated particles. The first mechanism [41] involves the formation of a floating graphene-cap. The nanotube-nucleation process was divided in three step: i) diffusion of single carbon atoms on the surface of the

catalyst ii) formation of an sp^2 graphene sheet floating on the catalyst surface with edge atoms covalently bonded to the metal iii) root incorporation of diffusing single C atoms (see Fig.9) [41]. The nucleation has therefore the fundamental role of nanotube-cap-creation in the CNT growth-mechanism. Interestingly a process involving the formation of islands of C atoms was proposed by Moisala *et al.*. In this process, the competition between two fluxes of carbon was described for the SWCNT nucleation-mechanism (see Fig.10) [35]: The segregation flux of dissolved carbon atoms towards the particle surface and the diffusion flux of carbon atoms toward the particle surface seeking their lowest energy states [35]. Due to the competition between the segregation and diffusion fluxes, two situations can occur in the system. First situation: if the segregation flux is higher than the diffusion flux, initiation of CNT growth can occur. This nucleation process occurs likely from islands where the segregation flux is larger. If the segregation flux is lower than the diffusion flux, carbon will form the thermodynamically most stable system consisting of metal particles surrounded by graphitic layers (see Fig.10).

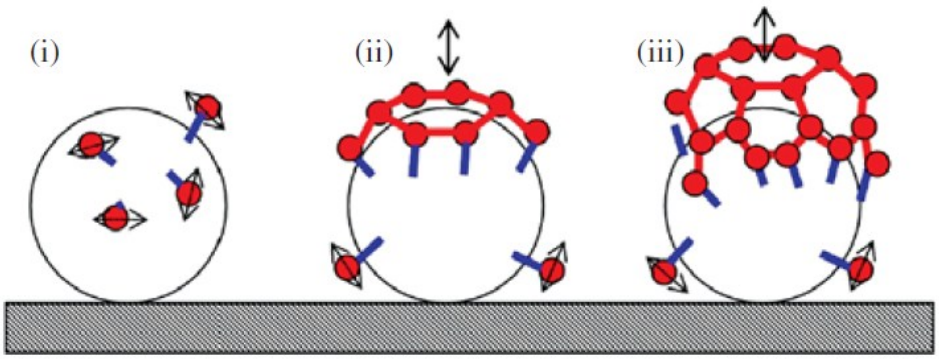

Fig.9: Nucleation of a carbon nanotube cap : i) shows the diffusion of single carbon atoms on the surface of the catalyst-particle ii) shows the formation of an sp^2 graphene sheet floating on the catalyst surface iii) represents the last step consisting of root incorporation of diffusing single C atoms [41].

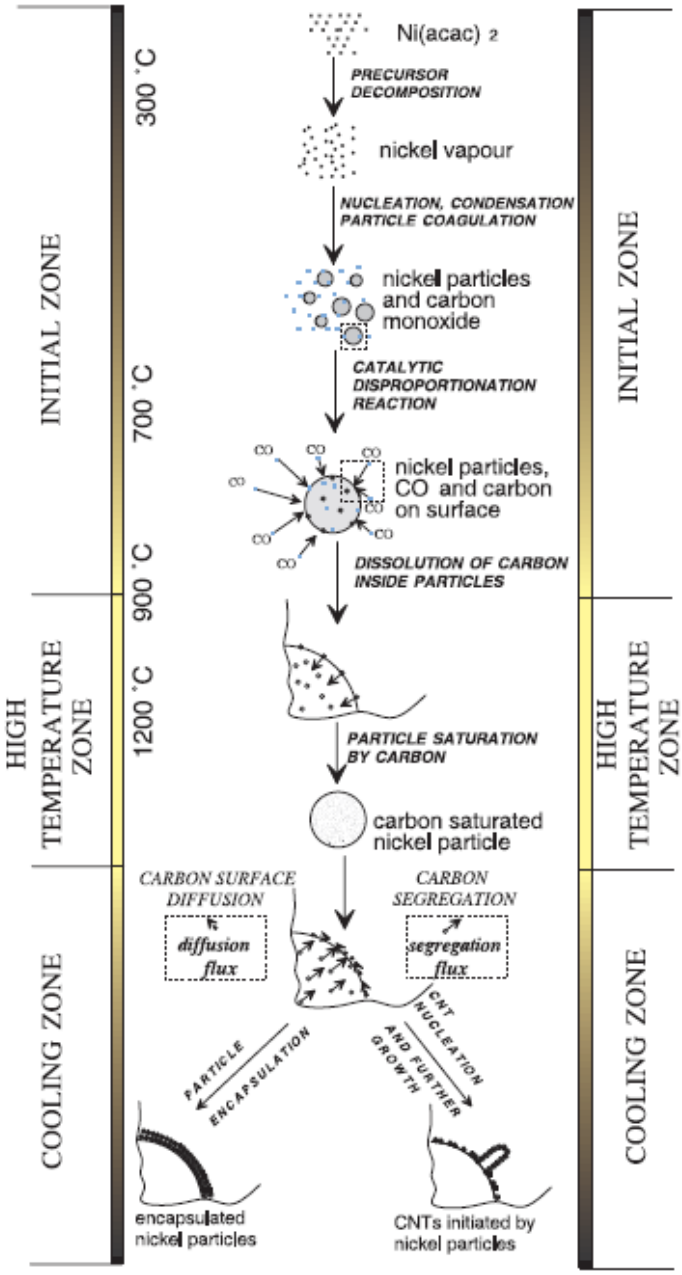

Fig.10: Growth mechanism of a single wall carbon nanotubes consisting in nucleation and growth. In the cooling zone the synthesis product is described as the result of the competition between the segregation flux of dissolved carbon atoms towards the particle surface and the diffusion flux of carbon atoms toward the particle surface seeking their lowest energy states [35].

In 1984 Gary Tibbetts completed the theory reported by Baker et al. explaining also why carbon filaments were tubular [47]. It was shown that the free energy required for the growth of a filament has a minimum value when graphite is in the form of a cylinder surrounding the metal. The inner core of the filament is hollow because inner cylindrical planes of small diameter would be highly strained and energetically unfavourable to form. Tibbetts explained a more detailed growth mechanism with a vapour-liquid-solid model, originally formulated for Si and Ge whiskers. [48]. These models are conventionally accepted for CNTs growth, but it is often questioned how Fe, Co, Ni (or other metals with normal melting point ~1500 ºC) could be in liquid state within 600–900 ºC.

It seems clear that the solubility of the carbon obtained from the pyrolysis of the hydrocarbons can have a great influence in the melting point of these metals particles [11,15,33-53]. Because of the dissolution of carbon and the small-diameter of the metal particles, the melting point can be considered to be far below the melting point of bulk metal [11,15,33-53].

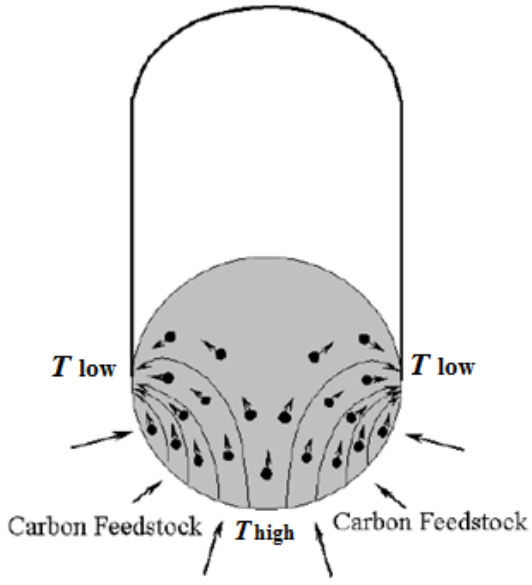

Fig.11: Temperature gradient in the catalyst during the nanotube growth [49].

This mechanism suggests also the presence of a temperature gradient in the metal-catalyst particle (see Fig.11) during the CNT growth [15,33-53]. This temperature gradient is connected to the process of carbon-dissolution inside the metal-particle [47]. Fe catalyst-particles reach supersaturation after a certain time of exposition to the pyrolyzed-hydrocarbon vapour (at 680–800 ºC). As a consequence, the new phase Fe_3C (iron carbide) is formed [15,50,51].

Previous reports have shown that the segregation of the carbon layers starts when the carbon concentration dissolved in the metal particles exceeds super-saturation, underlining the importance of Fe_3C in this process [15,50]. However the stability of Fe_3C in contact with the graphite shells is still under debate. The Fe_3C is generally considered not stable in contact with graphite [15]. The instability of this phase leads to carbon migration towards the volume of the particles and consequent deposition of graphite layers (see Fig.12). Since the nucleation must overcome an energy barrier (activation energy), other graphite layers will deposit around the former layers. The multiple repetition of the Fe_3C formation/decomposition is considered fundamental for the nanotube growth. However its formation/decomposition rate and the influence of the vapour carbon density in the growth-process are not well known and still controversial [15].

In fact, it is well known that for bulk Fe-C alloys, there is no metastable equilibrium between carbide and graphite phases; therefore, it would be not easy to think about the existence of a direct interface boundary between an Fe_3C filling and the graphitic shells of the nanotube.

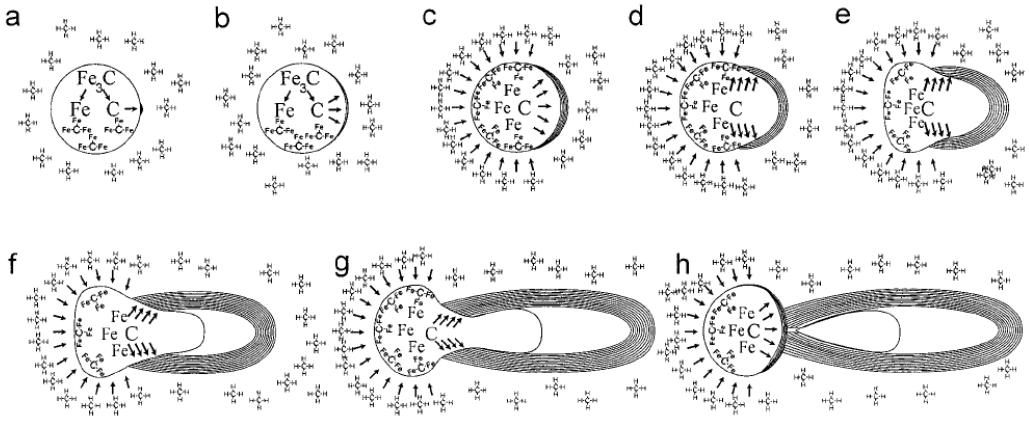

Fig.12: Growth mechanism of a carbon nanotube involving the supersaturation of the catalyst with carbon and the formation of Fe_3C. The instability of Fe_3C appears to be the key for nanotube growth [15].

Interestingly, it was proposed, by Kim *et al.*, that a thin layer of Fe can be formed between Fe_3C or rarely observed carbide and graphite, as a result of the carbide decomposition [52-53]. This thin layer can act as a catalyst, ensuring further deposition and CNTs growth. Interestingly, a so called metal-dusting process supports this hypothesis [54-62]. According to this process, when bulk Fe is exposed to a large amount of carbon in the temperature range of 400-800 ºC, Fe_3C and graphite are produced at the surface and a thin layer of Fe is formed between the Fe_3C and the graphite as a result of the decomposition of Fe_3C. Zhang *et al.* wrote that the formation of an α-Fe layer at the Fe_3C/graphite interface was observed at first during metal dusting of Fe in CO-H_2-H_2O gas mixtures at 700 ºC with low CO contents [55]. Moreover, it was shown that with the increasing of CO content in the gas mixture, the tendency of Fe particle/layer formation decreases. Indeed with 20% of CO only a small amount of Fe particles was found in the interface, while with 50% of CO no Fe was detected in the interface by optical microscopy. Zhang *et al.*, tried also to give an explanation of the rate of

the catalytic reaction, pointing out the reason for the Fe layer disappearance with high CO content [56]. It was written that at CO contents higher than 30 vol.% the catalytic reaction becomes much faster, and therefore, Fe particles that were formed by Fe_3C decomposition had no time to agglomerate. The fast catalytic reaction leads to filament formation, with particles that are then detached from the interface. A very important role is also played by the atmosphere in which the reaction is done. Indeed Podgurski *et al.* showed that the Fe_3C formed from an Fe_2C phase that had been prepared by exposure with a carbon monoxide vapour was quite stable and will withstand many hours heating in vacuum at 500ºC before decomposing [62]. On the contrary the Fe_3C formed from Fe_2C samples prepared by exposure with butane vapour, was found to decompose almost completely at 500ºC in a few hours. The cause of this difference is not well known, however it seems possible that the oxide impurity present in carbides, formed from carbon monoxide and a Fe catalyst, has a stabilizing effect on Fe_3C. This point was also confirmed by Browning [62].

Focusing the attention in the growth mechanism of metal-filled MWCNTs, Müller *et al.* proposed a growth mechanism known as open-ended base growth (Fig. 13) [17]. This mechanism is based on the idea that nanotubes are open during the growth process and carbon is added at their open ends. The closure of the tube will be observed when the growth rate decreases and finally stops. This can happen when a particle deposits on the open end and owing to the incorporation of pentagons and heptagons in the hexagonal carbon lattice, the high defect level leads to tube closure. Interestingly Guo *et al.* suggested that additional carbon atoms, bridging the dangling bonds between carbon shells provide stability to the structure [63]. Furthermore Kwon *et al.*, suggested the idea of covalent bonds

between adjacent walls [64]. Owing to the pressure imposed by the carbon to the catalyst-particle during the capping process, another Fe-based phase is conventionally observed inside the nanotubes: γ-Fe. The distribution of this phase is still under debate [7,13,14]. Leonhardt *et al.* observed that this phase is present mainly at the tips (capping-part) of the MWCNTs [7,65]. Marco *et al.* proposed that the MWCNT filling could consist of a shell structure composed of an α-Fe core surrounded by an γ-Fe shell, finally covered by an Fe_3C layer [13,14].

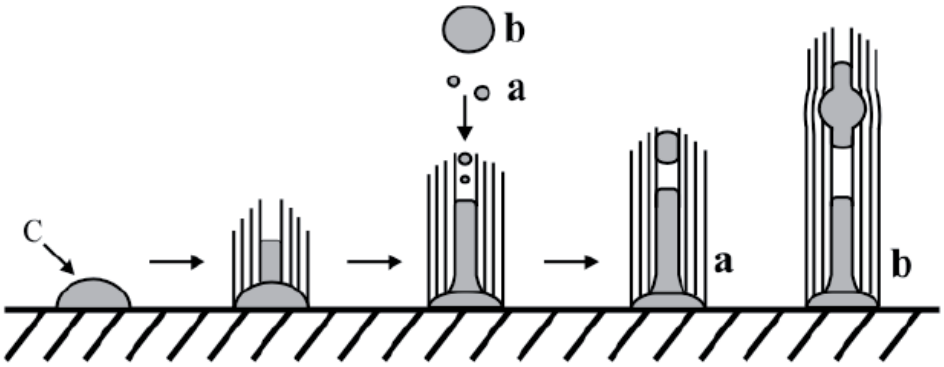

Fig.13: Schematic diagram representing the open-ended base growth mechanism [17].

1.5 Phase transformation of Fe_3C and γ-Fe

As shown in the previous sections, the main phases that generally fill the MWCNTs obtained by pyrolysis of ferrocene are α-Fe, Fe_3C and γ-Fe. The observation of the γ-Fe phase at room temperature is generally attributed to the pressure that the MWCNTs walls apply to the encapsulated Fe-based single crystals and can be justified by considering the phase diagram in Fig.14.

The phase diagram shows that the transition from the bcc α-Fe phase to the fcc γ-Fe phase starts at temperatures ~ 727 ºC and is complete at temperatures ~1000 ºC . This means that for CNTs syntheses performed at temperatures ~ 1000 ºC the main phases involved in the CNTs nucleation and growth processes will be γ-Fe and Fe_3C. However during the cooling process, the majority of the γ-Fe phase will come-back to the bcc α-Fe and orthorhombic Fe_3C phase (at room temperature) in a process involving the 9% of volume expansion [52-53], while the metastable Fe_3C could decompose into Fe and C in a slow process [7, 8, 18, 19].The residual quantity of γ-Fe will include all the γ-Fe single crystals that are not able to change phase back to α-Fe phase owing to the pressure imposed by the MWCNT walls (that does not allow the 9% volume expansion) [52,53].

To maximize the quantity of α-Fe, a post-synthesis heat-treatment is frequently considered since, as shown in the phase diagram (see Fig.14), bulk γ-Fe can decompose into α-Fe and Fe_3C below 727 ºC and bulk Fe_3C decomposes into α-Fe and graphitic carbon when is in contact with graphite; the maximum decomposition rate was reported to be in the temperature range 500-550 ºC [18,19]. Previous reports of post-synthesis annealing of closely packed arrays of MWCNTs filled with Fe_3C, γ-Fe and α-Fe phases showed that annealing for 15-20 hours at 645 – 675 ºC in Ar/H_2 or in Ar resulted in the decomposition of the encapsulated γ-Fe phase into α-Fe and Fe_3C [7, 8]. However difficulties in the decomposition of γ-Fe phase were observed in single-crystal regions constrained by the pressure of the MWCNT walls. Fig.15 shows the X-ray diffractograms that were obtained from two filled-MWCNTs samples (by Leonhardt *et al.*[7]), before and after annealing of the filled-MWCNTs for 20 h. It is interesting to notice that

after 20 h only α-Fe was observed and no Fe_3C and no γ-Fe were present inside the MWCNTs. However no informations about the decomposition rates of these two phases were reported.

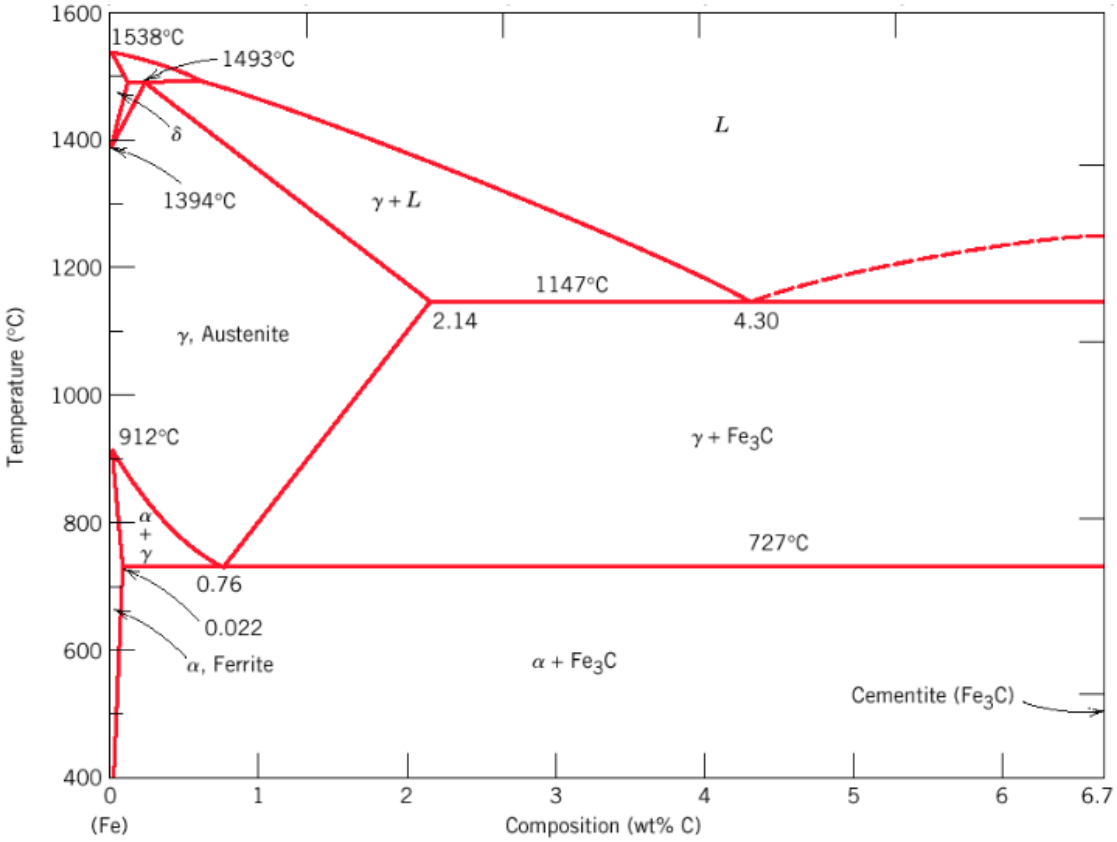

Fig.14: Fe-C phase diagram [18].

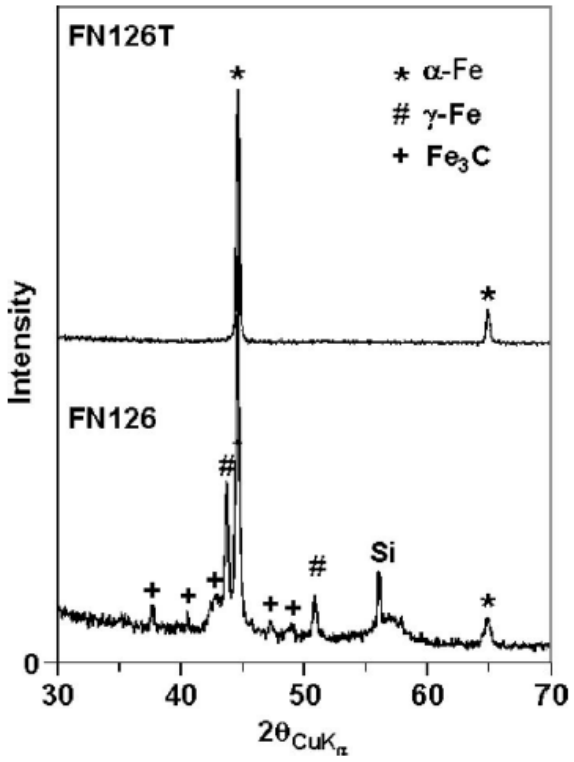

Fig.15: X-ray diffractograms of annealed (top) and unannealed (bottom) filled MWCNTs [7]. The peak indicated with the symbol Si refers to the 311 reflection of Si (space group Fd-3ms) and is due to the substrate where the MWCNTs were grown.

1.6 Observation of anomalously long lattice-spacings in Fe-based single-crystals

High resolution transmission electron microscopy (HRTEM) micrographs of unknown Fe-based crystals exhibiting anomalously long lattice-spacings were shown for the first time by Golberg *et al.* [11]. Interestingly, these structures show lattice-spacings much longer with respect to those present in the frequently observed Fe_3C [ICSD Ref. Code 16593], and the rarely observed less stable carbides Fe_2C [ICSD Ref. Code 76826], Fe_7C_3 [ICSD Ref. Code 167346], $Fe_{20}C_9$

[ICSD Ref. Code 740753] and $Fe_4C_{0:63}$[ICSD Ref. Code 9860]. Lattice spacings of 0.57 nm and 0.42 nm are expected for the rare stable carbide Fe_5C_2 [ICSD Ref. Code 76829 and 245334], while lattice spacings of >0.21 nm are not expected for α-Fe [ICSD Ref. Code 64795] and γ-Fe [ICSD Ref. Code 53803]. An unsuccessful attempt was made to match these lattice-spacings with those observed in the stable orthorhombic Fe_3C, or less stable iron carbides as Fe_5C_2 and Fe_7C_3 [11]. The characteristic anomalous lattice spacings observed by Golberg *et al.* were found to be 4.6 Å, 4.3 Å, 3.7 Å and 6.6 Å, as is possible to observe in Fig.16 and 17. These lattice-spacings were assigned, without supporting evidence, to rarely seen silicon doped octahedral iron carbides [11].

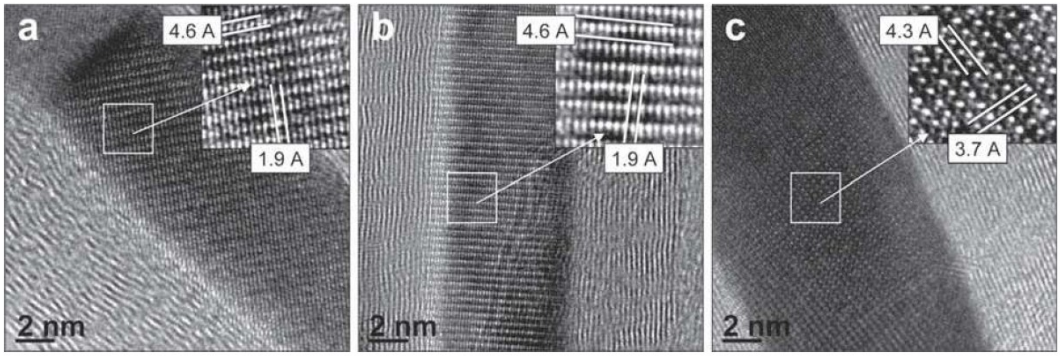

Fig.16: HRTEM micrographs of unknown Fe-C single crystals with anomalously long lattice spacings [11].

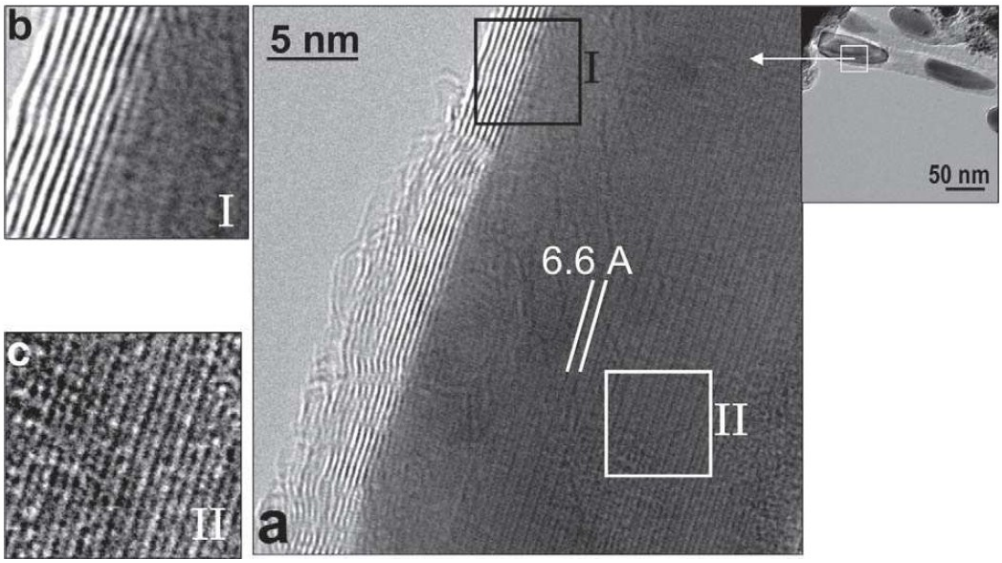

Fig.17: HRTEM micrographs of unidentified Fe-C single crystals exhibiting anomalously long lattice-spacings [11].

Moreover, it was also shown in another report that more anomalously long crystal lattice spacings were observed, however, the origin was never explained [17]. The measured inter-atomic distances were recognized as the doubled (110) spacing of α-Fe (lattice parameters $a = b = c = 2.886$ Å) with value of $d = 0.42$ nm and to the doubled (111) and tripled (220) spacings of γ-Fe (lattice parameters $a = b = c =$ 3.646 Å), respectively with values of 0.42 nm and 0.39 nm. Interestingly also Schaper *et al.*, Weissker *et al.* and Lutz *et al.* reported the evidence of structures with an anomalously long lattice-spacing [50, 66, 67]. In fact as is possible to see in Fig.18 the fast Fourier transform (FFT) of the partial image of the filling revealed the lattice parameter (010) reflection of a structure that was recognized as orthorhombic Fe_3C (space group *Pbnm*). Considering an orthorhombic structure, with a space group *Pnma*, in which generally the unit cell parameters are labelled as $a = 0.509$ nm, $b = 0.675$ nm and $c = 0.452$ nm, the only allowed sets of reflection would be (hkl) = no conditions, (h00) with h=2n, (0k0) with

k=2n, (00*l*) with *l*=2n, 0*kl* with *k*+*l*=2n and hk0 with *h* =2n. In the case of an orthorhombic structure, with a space group *Pbnm* and with unit cell parameters *a* = 0.453 nm, *b* = 0.508 nm and *c* = 0.674 nm, the only allowed reflections would be for (*hkl*)= no conditions, (*h*00) with *h*=2n, (0*k*0) with *k*=2n, (00*l*) with *l*=2n; 0*kl* with *k*=2n and *h*0*l* with *h*+*l*=2n. In both cases the observation of the (100) or the (010) reflection is forbidden by the selection rules imposed by the symmetry of the crystal in kinematic diffraction conditions [67-68].

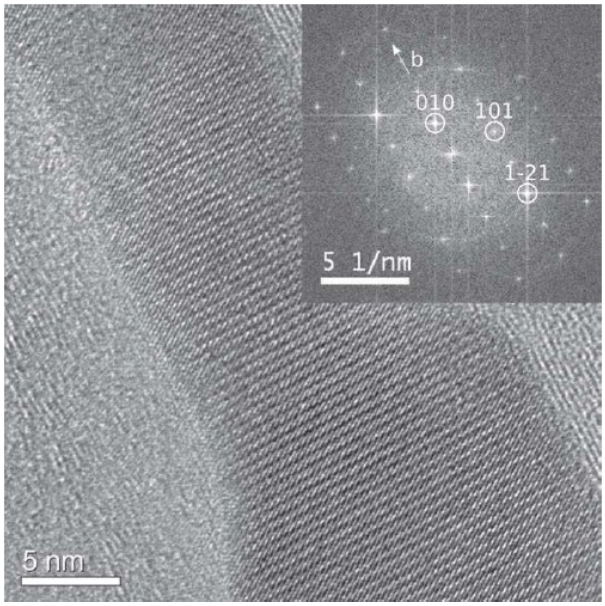

Fig.18: HRTEM image and FFT of the MWCNT filling exhibiting anomalously long lattice-spacings [66, 67].

1.7 Control of diameter and length of the filling

In the last decade numerous attempts were made to achieve a complete control of the length and diameter of the ferromagnetic single-crystals filling the MWCNTs. Despite the great number of reports presented in literature, it is still difficult to understand how to completely control the single-crystals dimensions. In 2003 it was reported that continuous filling could be achievable by using high sublimation rates and high pyrolysis temperatures of ferrocene [10], however this statement was recently contradicted [7], showing that only filling rates of ~ 40% are achievable with SSCVD and, that the limiting factor is related to the stoichiometry of each ferrocene molecule containing 10 atoms of C and only 1 atom of Fe [7,8]. The diameter of the MWCNT filling seems to increase with the concentration of ferrocene in the vapour [10]. Considering that the size of the catalyst particles fixes the diameter of the growing nanotubes, an increase in the ferrocene concentration would lead to a higher clustering rate of the catalyst particles and therefore to a larger single-crystals diameter [10]. Similar considerations about the filling length have been reported also in the case of LSCVD. In this case the MWCNTs are generally discontinuously filled for 45% of the cores [8,26]. Similarly to SSCVD, also in LSCVD the single-crystal diameter depends on the concentration of ferrocene [8,26]. Cyclopentane, toluene, trichlorobenzene are frequently used as a second carbon source in addition to ferrocene [9,26,69]. Interestingly, especially in the case of toluene, it has been shown that the diameter of the single crystals can be smaller than 10 nm. This could be due to the additional pressure that is imposed by the higher quantity of carbon in the ferrocene/toluene vapour. The higher quantity of carbon also seems

to be responsible of the complete supersaturation of the Fe single-crystals [9]. So, in the case of LSCVD the formation of small (~10 nm) single crystals of Fe_3C is generally favoured by the very high quantity of carbon in the vapour [9]. However, the addition of a second carbon source leads also to a reduction of the filling length [9,26].

1.8 Magnetic properties of multiwall carbon nanotubes filled with Fe-based single crystals and applications

To investigate the magnetic properties of MWCNTs filled with Fe-based single crystals, many techniques can be used. As reported by Leonhardt *et al.* one of the most common methods is the alternating gradient method (AGM) [7]. By using this method, typical hysteresis loops can be measured for an aligned array of filled-MWCNTs deposited on the silicon substrate. The saturation magnetization M_s and the coercivity H_c of these nanostructures depend not only on the ferromagnetic α-Fe fraction that is generally present in the sample but also on the alignment level, on the diameter and on the length of the filling. The magnetic properties of individual filled-MWCNTs were also investigated in previous reports [66,67]. In particular magnetic force microscopy was used to investigate the magnetic properties of single domain α-Fe and Fe_3C [66,67]. The ferromagnetic properties of α-Fe single-crystals are strongly dependent on the axial shape anisotropy [67] while, the ferromagnetic properties of Fe_3C single-crystals are strongly affected by the magnetocrystalline anisotropy so the shape

anisotropy plays a lesser role [66, 67]. γ-Fe is paramagnetic at room temperature and antiferromagnetic at $T < 50$ K [12,13,14]. The graphitic carbon of the MWCNT walls is paramagnetic at room temperature and slightly diamagnetic at $T<50$ K [70]. The coercivity of these nanostructures appears to be strongly dependent on the alignment [7], the magnetocrystalline anisotropy [9,66,67,69], the filling diameter, and the spatial-distribution of the filling-phases inside the nanotubes [13,14]. The saturation magnetization of a powder containing MWCNT filled with γ-Fe, α-Fe and Fe_3C seems to be dependent mainly on the quantity of α-Fe [6,7]. Previous reports have shown that after annealing [7], the saturation magnetization of the powder increased owing to the higher quantity of α-Fe (owing to the phase transformation) inside the MWCNT [7].

Owing to the very small diameter size, the high aspect ratio and the very high coercivity, the Fe_3C and α-Fe single crystals fillings are generally considered to be in a single magnetic domain arrangement [66,67]. The magnetic arrangement of these single crystals were carefully analysed in the reports of Weissker *et al.*[66] and Lutz *et al.* [67]. In these reports the single crystals are approximated as single magnetic domain with an estimated critical diameter size of 60 nm for a spherical single crystal of Fe_3C [66,67]. Interestingly also Ruitao *et al.* reported very high (2000 Oe) coercivity dependent mainly on the small diameter of the ferromagnetic single crystals used for the buckypaper [69]. However in this case no structural X-ray or selective area electron diffraction analyses were shown, so it is difficult to understand the phase composition and physical distribution of the single crystal-phases filling the MWCNTs. The high resolution transmission electron micrograph that was reported, clearly show the presence of orthorhombic Fe_3C single crystals inside the MWCNTs, so the magnetocrystalline anisotropy

contribution in this case could play also an important role [69]. The coercivity displayed by the single crystals filling the MWCNTs (at low temperatures) seems to be also independent of the applied magnetic field directions.

Very high coercivities of single magnetic domain crystals filling the MWCNTs were also reported by Aaron Morelos-Gomez *et al.*[9]. In this particular case the very high coercivity seems to be mainly related to the contributions of Fe_3C single crystals (single magnetic domain). In particular from this report it seems clear that the coercivity increases dramatically when the diameter of the single-crystals decreases, whereas no effect from the length variation is detected. More considerations about the critical single-domain diameter size were also reported by Philippi *et al*. In this case micrometre-length α-Fe single crystals with a diameter of 30 nm were approximated as single magnetic domain [71].

MWCNTs filled with ferromagnetic α-Fe or Fe_3C can be potentially used in a wide range of applications owing to the ability to tune the magnetic response through the composition, magnetocrystalline anisotropy and shape anisotropy of the filling. Small and thin α-Fe or Fe_3C filled MWCNTs have potential applications in: magnetic storage media and quantum disk fabrications [5], owing to the very high coercivity displayed by single domain α-Fe or Fe_3C [9]; drug delivery systems, nanoscale containers for biomedical diagnosis, therapy, and monitoring owing to the high mechanical strength of the MWCNTs and to the heat dissipation produced by the magnetic moment reversal in presence of a time varying magnetic field [72-76]. Many other applications require long MWCNTs filled continuously with Fe_3C or α-Fe single crystals: nanoscale inductors [77], magnetic force microscopy probes [78], nanocomposite magnetic filler particles [79], buckypaper [69], and microwave absorption materials [80]. Other

applications exploit the torque on the structures when placed in a constant magnetic field [81], or the oscillatory motion when placed in a time-varying magnetic field [71].

1.9 Theory of chemical vapour synthesis and boundary layer flow

Chemical vapour synthesis (CVS) is a modified CVD method where the synthesis parameters are adjusted to form nanoparticles instead of a film [22].

In CVD processes, particle formation is conventionally avoided to prevent the formation of defects and other sources of disorder that could consume the precursors intended for the film growth [22]. The CVS conditions generally require high reaction temperatures, high supersaturation conditions, low (carrier) gas flows and long reactors [22]. The principle advantages of the reactions in the gas phase are very short process times and nanoscaled powder of high purity with a narrow particle size distribution.

1.9.1 Boundary-layer in a gas flow from a leading edge of a plate

Viscosity can be defined as the measure of the internal resistance of a fluid to flow [82]. Viscous forces are generally described in terms of a shear stress τ between the fluid layers. If this stress is assumed to be proportional to the normal velocity gradient it is possible to define the viscosity as shown in equation (16):

$$\tau = \mu \frac{du}{dy} \quad (16)$$

The constant of proportionality μ is called the dynamic viscosity, and u represents the velocity. The region of flow that develops from the leading edge of a plate (in Fig.19) in which the effects of viscosity are observed is defined as ‘‘boundary layer’’. An arbitrary point is generally used to designate the y position where the boundary layer ends; this point is usually chosen as the y coordinate where the velocity becomes 99% of the free-stream value.

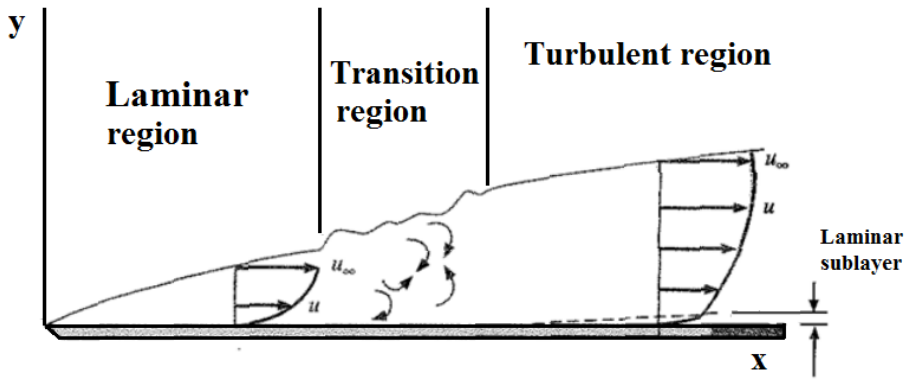

Fig.19: Schematic diagram of a boundary layer developing at the leading edge of a plate [82].

Initially, the boundary layer is laminar, but at some critical distance from the leading edge, small disturbances in the flow begin to become amplified, and a transition process takes place until the flow becomes turbulent. The transition from laminar to turbulent flow is described by equation (17):

$$\frac{u_\infty x}{\nu} = \frac{\rho u_\infty x}{\mu} > 5 \times 10^5 \qquad (17)$$

Where u_∞ is the free-stream velocity, x the distance from the leading edge, ρ is the density of the fluid and ν the kinematic viscosity.

This particular grouping of terms (shown also in equation (18)) is defined as ‘‘Reynolds number ’’, and is dimensionless:

$$Re_x = \frac{u_\infty x}{\nu} \qquad (18)$$

1.9.2 Heat transfer and eddy viscosity in turbulent-boundary layer in a gas flow from a leading edge of a plate

Focusing the attention in the turbulent region of the boundary layer is possible to define the instantaneous velocity (equation (19)) in a turbulent-flow as composed of fluctuations about the mean flow velocity. As shown in Fig.20, $\overline{u_x}$ is the mean velocity and u' is the fluctuation from the mean (in the *x* component of velocity).

$$u_x = \overline{u_x} + u'_x \qquad (19)$$

For steady flow conditions the mean value of the fluctuation u'_x is zero over a certain time. There are also fluctuations in the *y* component of velocity, as shown in equation (20):

$$u_y = \overline{u_y} + u'_y \qquad (20)$$

The fluctuations give rise to a turbulent-shear stress as shown in Fig.20

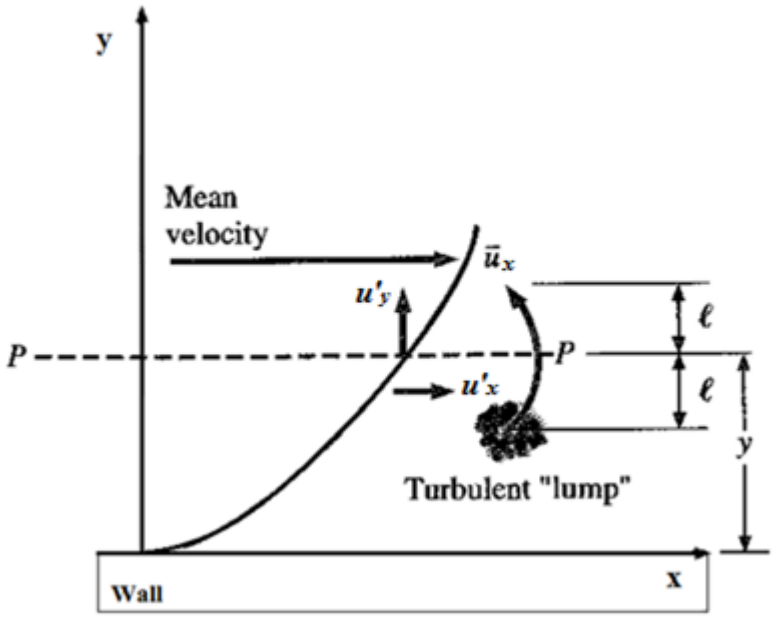

Fig.20: Schematic diagram of a turbulent lump (eddy) fluctuation u' and mean velocity $\overline{u_x}$ [82].

The instantaneous turbulent mass transport rate across the plane (P-P) is described by the product $\rho u'_y$. A change in the *x* component of the velocity u'_x is also associated with this mass transport [82].

When a turbulent lump moves upward ($u'_y > 0$) it enters a region of higher $\bar{u}$, effecting a slowing-down fluctuation in u'_x [82]. This can be seen also in equation (21) that defines the average turbulent-shear stress.

$$\tau_t = -\overline{\rho u'_y u'_x} \qquad (21)$$

The turbulent lump in Fig.20 can be considered as located at distance ℓ above or below the plane P-P. This lump of fluid can move back and forth across the plane

and give rise to the eddy or turbulent shear-stress effect. At $y+\ell$ and $y-\ell$ the velocity would be approximately defined by equations (22) and (23).

$$u(y+\ell) \approx u(y) + \ell \frac{\partial u}{\partial y} \qquad (22)$$

$$u(y-\ell) \approx u(y) - \ell \frac{\partial u}{\partial y} \qquad (23)$$

The turbulent fluctuation u'(see equation (24)) is proportional to the mean of the two quantities expressed above

$$u' \approx \ell \frac{\partial u}{\partial y} \qquad (24)$$

This expression is known as Prandtl postulate and the distance ℓ shown in Fig.20 is called Prandtl mixing length [82]. Prandtl also postulated that u'_x would be of the same order of magnitude as u'_y, so the turbulent shear stress and eddy viscosity will be then written as follows (equation (25) and (26)).

$$\tau_t = -\overline{\rho u'_y u'_x} = \rho \ell^2 \left(\frac{du}{dy}\right)^2 = \rho \epsilon_M \frac{du}{dy} \qquad (25)$$

$$\epsilon_M = \ell^2 \frac{\partial u}{\partial y} \qquad (26)$$

The turbulent heat transfer [82] per unit area associated with the turbulent lump movement previously described can be then defined (equation (27)) in analogy with equation (25).

$$\left(\frac{q}{A}\right)_{turb} = -\rho c_p \epsilon_H \frac{\partial T}{\partial y} \quad (27)$$

Where c_p is the specific heat at constant pressure.

1.9.3 Effect of surface roughness and fluctuating eddies

The framework of rough-wall flow has been investigated since 1933, when Nikurdse [83] found that with increasing Reynolds number the flow depended on the relative scale of the roughness *k*/*d*. *k* usually represents the roughness scale, while *d* is used to represent the pipe diameter. Nikurdse found that increasing Reynolds number the flow becomes independent from the viscosity and is a function of *k*/*d* alone. Flow dependent on *k*/*d* alone was defined fully rough, while flow dependent on both *k*/*d* and Reynolds number was defined transition flow. A boundary layer on a rough wall behaves as if its origin is located at some distance below the crest of the rough elements. The distance below the crest of the elements can be qualitatively defined as a measure of the interaction between the mean flow and the roughness. In the case of *k* roughness, eddies with a length scale proportional to *k* are assumed to be shed into the flow above the crest of the elements. On a *d* type roughness the elements are more closely spaced and stable vortices are set up in grooves. In this case eddy shedding from the elements into the flow is generally considered negligible [83]. A qualitative example of the *k* and *d* roughness is shown in Fig.21 , more details about the theoretical description can be found in [83].

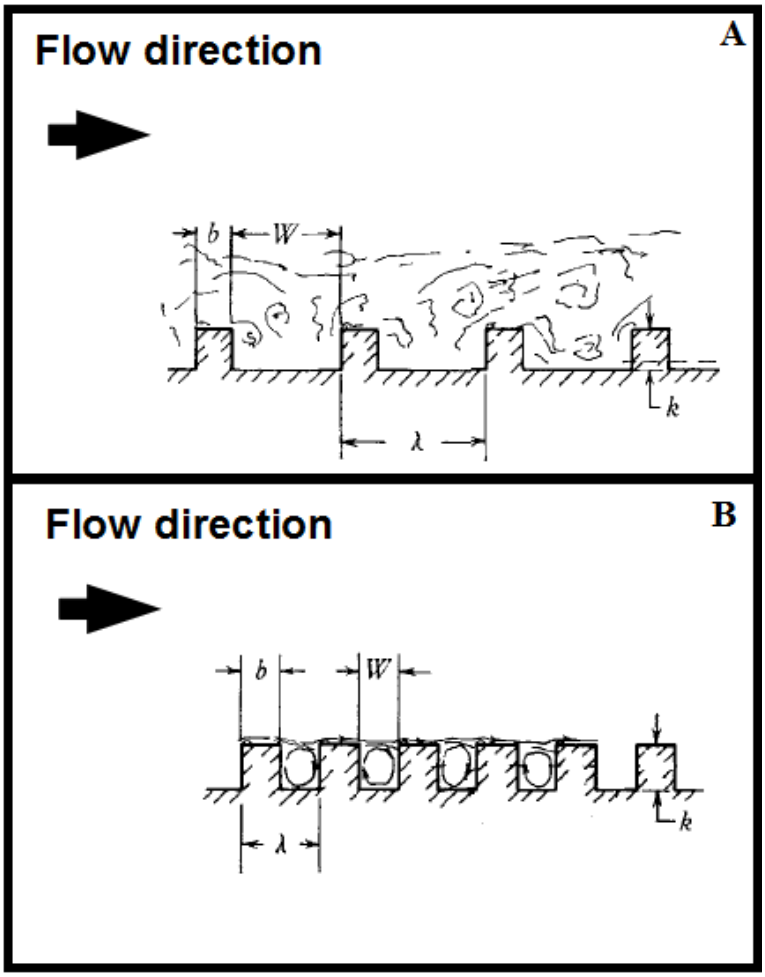

Fig.21: Schematic diagram of the effect of *k* (A) and *d* (B) type roughness in a flow [83].

Chapter 2

Experimental methods and techniques

2.1 Synthesis

2.1.1 Boundary Layer chemical vapour synthesis method

Radial structures comprising multiwall carbon nanotubes continuously filled with ferromagnetic single-crystals of α-Fe or Fe_3C were produced in randomly fluctuating vapour in the viscous boundary layer between a rough quartz surface (quartz substrate) and a laminar vapour flow. A schematic diagram of the reactor used for the synthesis is shown in Fig.22. In Fig.23 a scanning electron micrograph of the rough surface of the substrate is shown.

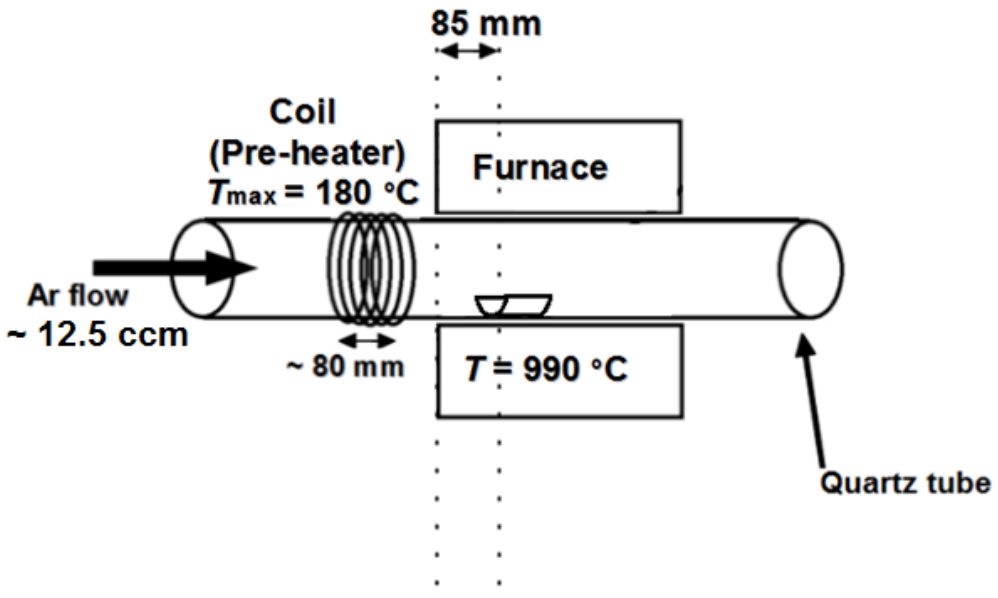

Fig.22: Schematic diagram of the reactor used for the synthesis of the radial structures.

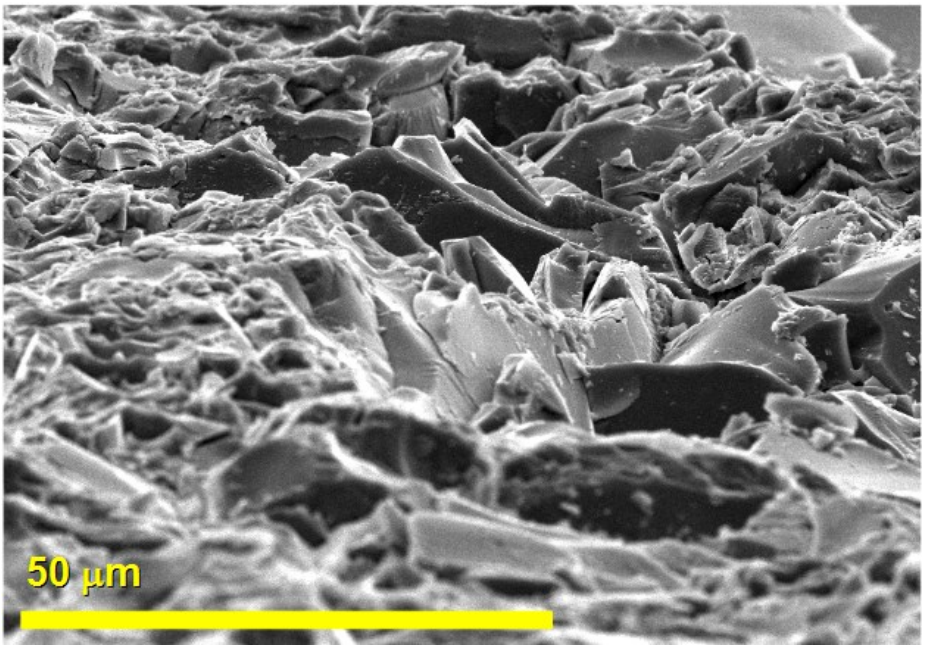

Fig.23: Scanning electron micrograph (taken at 20 kV) showing the rough surface of the quartz substrate used for the synthesis of the radial structures.

The rough surfaces were prepared by roughening a quartz substrate using a conventional diamond cutting tool to produce multi-scale roughness with a peak-to-valley distance of ~30-60 μm. The source vapour was produced by sublimation of 60-100 mg of ferrocene in a quartz tube reactor with the following dimensions: length: 2 m, outer diameter: ~ 22 mm, inner diameter: ~ 19 mm, wall thickness: ~ 1.5 mm. The maximum temperature of the preheater was 180 °C (reached in ~ 3 min). The synthesis product was achieved using the argon flow rates between 3 and 20 cubic centimetres per minute and a furnace temperature of ~ 990 ºC. The best growth conditions were achieved with a flow rate of 12.5 ccm. The average Reynolds number for the ferrocene vapour flow was estimated to be Re=2-4; well within the range for laminar flow, Re<2000 [82]. The duration of the reaction was 4.5 minutes. The reactor was cooled to room temperature at the natural rate of the

furnace. After removal from the reactor, the radial structures were magnetically and mechanically removed from the quartz substrates and dispersed in ethanol.

2.1.2 Locally-perturbed chemical vapour deposition method

Flower-like structures of MWCNTs continuously filled for at least 19 micrometre length were produced in perturbed-vapour chemical vapour deposition conditions. A small hole (approximately 1 mm diameter) in an otherwise smooth quartz substrate was used to locally perturb a laminar ferrocene/Ar vapour flow. The perturbation influences the transport of the Fe- and C-containing species (products of ferrocene pyrolysis). The reactions were performed by sublimation and pyrolysis of 80-111 mg of ferrocene in an Ar flow inside a reactor reactor with the following dimensions: length: 2 m, outer diameter: ~ 22 mm, inner diameter: ~ 19 mm, wall thickness: ~ 1.5 mm. Inside a one-zone electrical furnace with an isothermal reaction zone at 990 °C. The maximum temperature of the preheater was 180 °C and the duration of the reaction was 4 minutes. The synthesis product was achieved using the argon flow rate of 12.5 cubic centimetres per minute. A schematic diagram of the quartz substrate is shown in Fig.24. Two alternative methods of sample-cooling were used. In the first method the sample was left to cool down at the natural rate of the furnace in an argon flow.

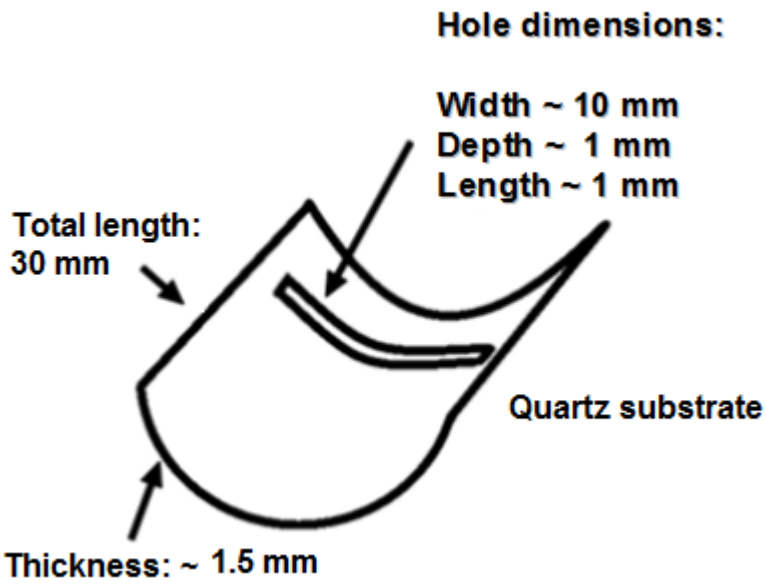

Fig.24: Schematic diagram of the substrate used for flower-like MWCNT structures synthesis.

The use of a slow cooling method guarantees a low relative abundance of Fe_3C single crystals inside the MWCNTs. Since Fe_3C is not stable in contact with the MWCNTs walls, in slow cooling conditions the carbon atoms will migrate from the Fe_3C single crystals-core toward the single crystal-MWCNTs walls interfaces, forming additional graphitic layers. In the second method, to avoid the formation of iron oxide, the sample was cooled rapidly through a quench by removing the furnace along a rail system. If the cooling procedure is very fast (quench method), the carbon atoms have not enough time to migrate and the relative abundance of Fe_3C will be higher with respect to the relative abundance of α-Fe. A post-synthesis annealing was performed following the first method of cooling, by reducing the furnace temperature to 500 °C with the substrate under Ar flow and then annealing at 500 °C for 10 h (note that annealing the sample after first

exposing to air resulted in complete oxidation of the flower-like MWCNT structures to α-Fe_2O_3 powder). After annealing under Ar flow, the sample was brought to room temperature at the natural cooling rate of the furnace (under Ar). After removal from the reactor, the flower-like MWCNT structures were mechanically removed from the quartz substrates and dispersed in ethanol or in distilled water.

2.2 Characterization

Transmission electron microscopy (TEM), HRTEM, SEM and X-ray diffraction (XRD) were used to analyse the morphology and the structural composition of the MWCNT filling. Electron energy loss spectroscopy (EELS) was used to measure the chemical composition of the Fe-based single-crystals.

2.2.1 X-Ray Diffraction

XRD analyses were performed with a Siemens D5000, an Xpert-Pro and an Panalytical Empyrean diffractometers (all with Cu K-α sources with λ = 0.154 nm). The samples were prepared by evaporation of the ethanol in which the MWCNT were previously dispersed. A schematic diagram of the diffractometer is shown in Fig. 25. The diffractograms were analyzed using the inorganic crystal structure database (ICSD) and the international centre for diffraction data (ICDD) cards of the phases commonly observed as products of the pyrolysis of ferrocene.

The Rietveld refinement method, which uses the least-squares approach to match a theoretical line profile to the diffractogram, was used to identify and estimate the relative abundances of the encapsulated phases from the area enclosed by the

diffraction peaks. The software ‘‘GSAS’’ (General Structure Analysis System) was used to refine a theoretical line profile until it matched with the measured one.

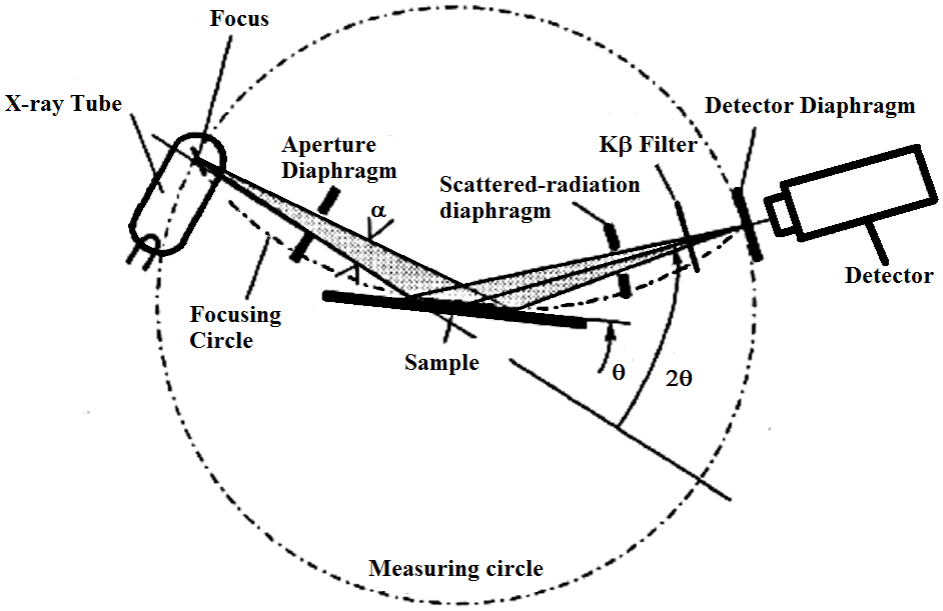

Fig.25: Schematic diagram of a X-ray diffractometer.

The function type 1 (shifted Chebyschev) with 8 numbers of terms was used as background function. Also the scaling and profile (LX) commands were used to improve the quality of the refinement. The diffraction peaks of Fe_3O_4 with space group *Fd3-ms* were considered only in the case of magnetic data analyses. The Fe_3O_4 diffraction peaks were excluded from all the other Rietveld refinements since this phase is not inside the MWCNTs but results from spontaneous oxidation of Fe particles when the sample is handled in air (confirmed by electron microscopy).

In order to obtain a diffraction peak the Bragg condition (equation (28)) must be satisfied:

$$2dsin\theta = n\lambda \qquad (28)$$

Where n is an integer and the other terms are shown in Fig.26.

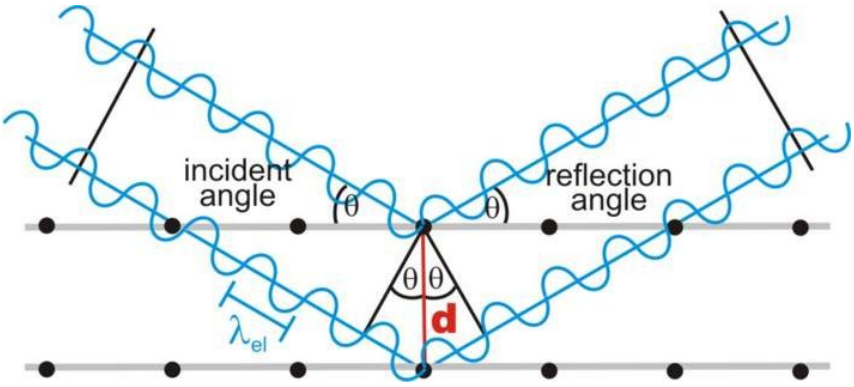

Fig.26: Schematic diagram of X-rays diffracting from the atomic planes of a crystal.

2.2.2 Electron Microscopy

SEM investigations were performed using an FEI Inspect F microscope.

TEM, HRTEM, and selective area electron diffraction (SAED) investigations of the Fe-C phases exhibiting anomalously long lattice spacings were performed using a 200 kV Jeol Jem 2010, 300 kV Jeol 3000F and an FEI TITAN 80/300 (S) TEM (accelerating voltage of 80 kV). The lattice spacings extracted from the SAED analyses are reported with an accuracy of ± 0.01 nm.

The TEM and SAED investigations for the characterization of the radial-structures and flower-like structures were performed using only the 200 kV Jeol Jem 2010. The calibration results from lattice plane resolution test of evaporated gold particles induced to grow in a (100) direction: 0.14 nm for the (220) lattice planes and 0.20 nm for the (200) lattice planes. The Image acquisition and processing software used in all the TEM investigations was Gatan Digital Micrograph. The TEM samples were prepared by two main steps. The continuously filled MWCNTs were firstly dispersed in ethanol or distilled water and then transferred on the top of carbon-coated copper grids.

In the case of the EELS measurements we noticed that long exposure to the electron beam of the MWCNTs previously dispersed in ethanol, lead to the production of contamination agents (hydrocarbons). This contamination process was considered to be due to a residual layer of ethanol in the TEM grid. To solve this problem, another TEM grid was prepared with MWCNTs previously dispersed in distilled water. In this case no contamination problem was found and all the measurements were performed successfully. EELS investigations were performed using a FEI TITAN 80/300 (S) TEM (accelerating voltage of 80 kV) fitted with a GIF Tridiem electron energy-loss spectrometer.

The EELS technique can be used to measure the energy distribution of electrons that have interacted with a specimen and lost energy due to inelastic scattering. The excitation of atomic $2p_{3/2}$ and $2p_{1/2}$ electrons by a transmitted electron gives rise to Fe-$L_{2,3}$ ionization edges. The Fe-$L_{2,3}$ spectra are sensitive to the local environment of Fe in Fe-based phases, so do not include signals from the graphitic MWCNT walls. The ratio of the integrated area under the L_1 and L_2 peaks, Fe-L_3/L_2, is useful to identify the composition of the MWCNT filling by comparison

with the values previously reported in the literature. EELS data were acquired at collection semi-angle of 22 mrad, dispersion 0.2 eV/pixel and acquisition time of 8 s. The spectra were acquired at multiple points along the MWCNT fillings selected from different regions of the TEM grid. The averaging was over four spectra acquired from eleven different filling-MWCNT regions.

The analyses were performed following the approach of Pearson *et al.* for 3d transition metals (reported also by Riedl *et al.* [84-85]), which approximates the Fe-$L_{2,3}$ ionization edges as a sum of two step functions. The extracted Fe-L_3/L_2 values are expressed with an accuracy of ±0.1.

2.2.3 Magnetic characteristics

The magnetic properties of the continuously filled MWCNTs were measured in a MPMS-7 magnetometer with a superconducting quantum interference device (SQUID). The magnetisation was measured as a function of magnetic field up to 50 kOe and temperature from 300 to 5 K. For field-cooled (FC) magnetization measurements, the sample was cooled 3 times from 300 K down to 5 K under the magnetic fields of 0.1 kOe, 1 kOe and 10 kOe respectively. The magnetization was measured as function of temperature as the sample was cooling.

Chapter 3

Results and discussion

3.1 Preliminary results

The synthesis of MWCNTs continuously filled with single crystals of ferromagnetic α-Fe was firstly attempted with the conventional CVD approach by pyrolysis of an Ar/ferrocene vapour flow on SiO_2 substrates in steady state conditions. A schematic diagram of the system used for these first experiments is shown in Fig.27. The reactor consisted of a quartz tube with the following dimensions: length: 2 m, outer diameter: ~ 22 mm, inner diameter: ~ 19 mm, wall thickness: ~ 1.5 mm. The ferrocene powder (60-70 mg) was sublimated in a preheater zone (ramp with T_{max} of 180 ºC reached in ~ 3 min). The ferrocene vapour was then transported in the reaction zone by using a low Ar flow rate of 12 ccm and pyrolysed at ~ 990 ºC. The temperature profile of the furnace is shown in Fig. 28. Thermally oxidized Si/SiO_2 (thickness of SiO_2 layer ~ 1 μm) substrates were placed in different regions of the hotter zone of the reactor to understand the position where ferrocene reaches the optimum pyrolysis conditions. The synthesis time was 4 min. The produced samples were then cooled to room temperature at the natural rate of the furnace. Preliminary investigations of the cross-sections of the substrates extracted from the reactor (after the synthesis) revealed the growth of closely packed arrays of partially filled MWCNTs. A typical example of these arrays is shown in Fig.29. A typical example of a single discontinuously filled MWCNT is shown in Fig.30. From a first analysis, it was clear that even the use

of flow-rates much lower with respect to those previously reported in literature (100-200 ccm) and very high concentration of ferrocene does not change the morphology of the closely packed MWCNT arrays that remain filled only discontinuously.

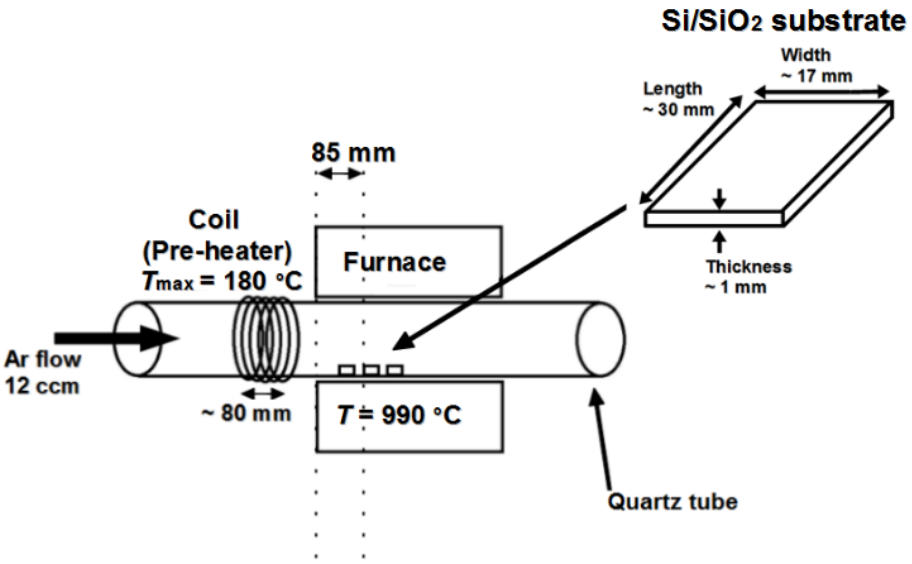

Fig.27: Schematic diagram of the reactor used for the synthesis of the filled-MWCNTs. The geometry and the dimensions of the substrates are also shown.

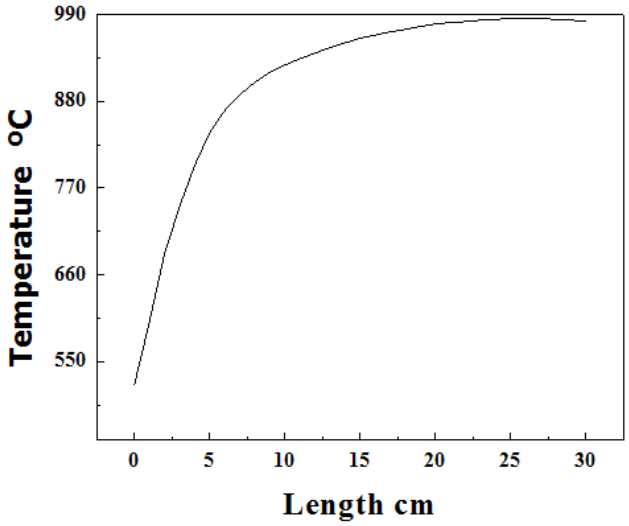

Fig.28: Temperature profile of the first 30 cm of the furnace used for the synthesis of the filled-MWCNTs measured from the starting point of the furnace (0 cm in the profile).

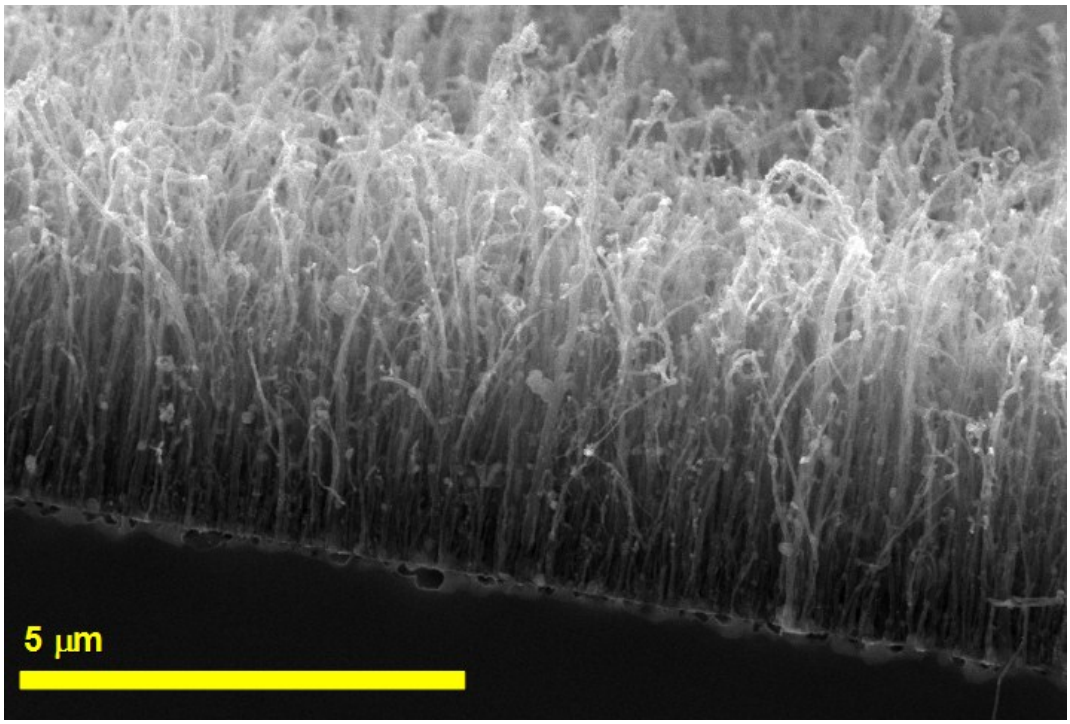

Fig.29: Scanning electron micrograph (taken at 20 kV) showing the cross-section of closely packed arrays of partially filled MWCNTs.

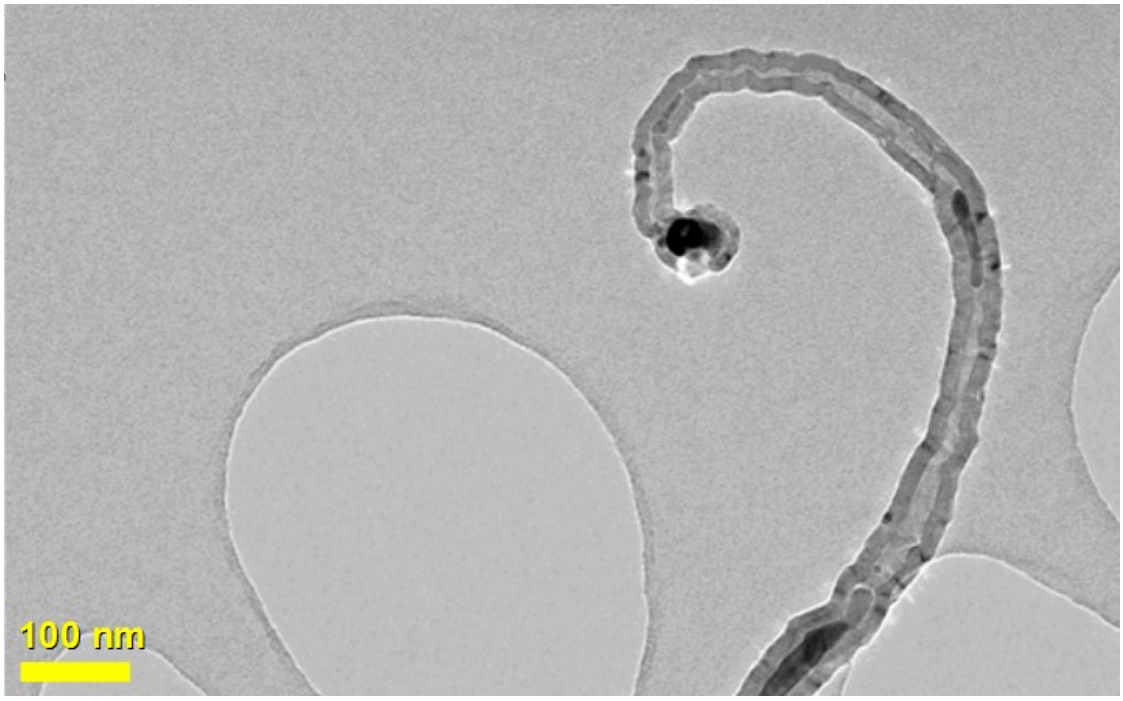

Fig.30: Transmission electron micrograph (taken at 200 kV) showing a typical example of partially filled MWCNT.

However, further investigations of the samples obtained with these experiments led to the serendipitous observation of not previously observed radial-structures comprising MWCNTs continuously filled with single-crystals of ferromagnetic α-Fe and Fe_3C departing from a central core particle. These new radial structures were firstly observed on the top of the closely-packed filled-MWCNTs arrays, and especially near the vapour-flow-facing edge of the substrate. Two examples are shown in Fig.31 and 32.

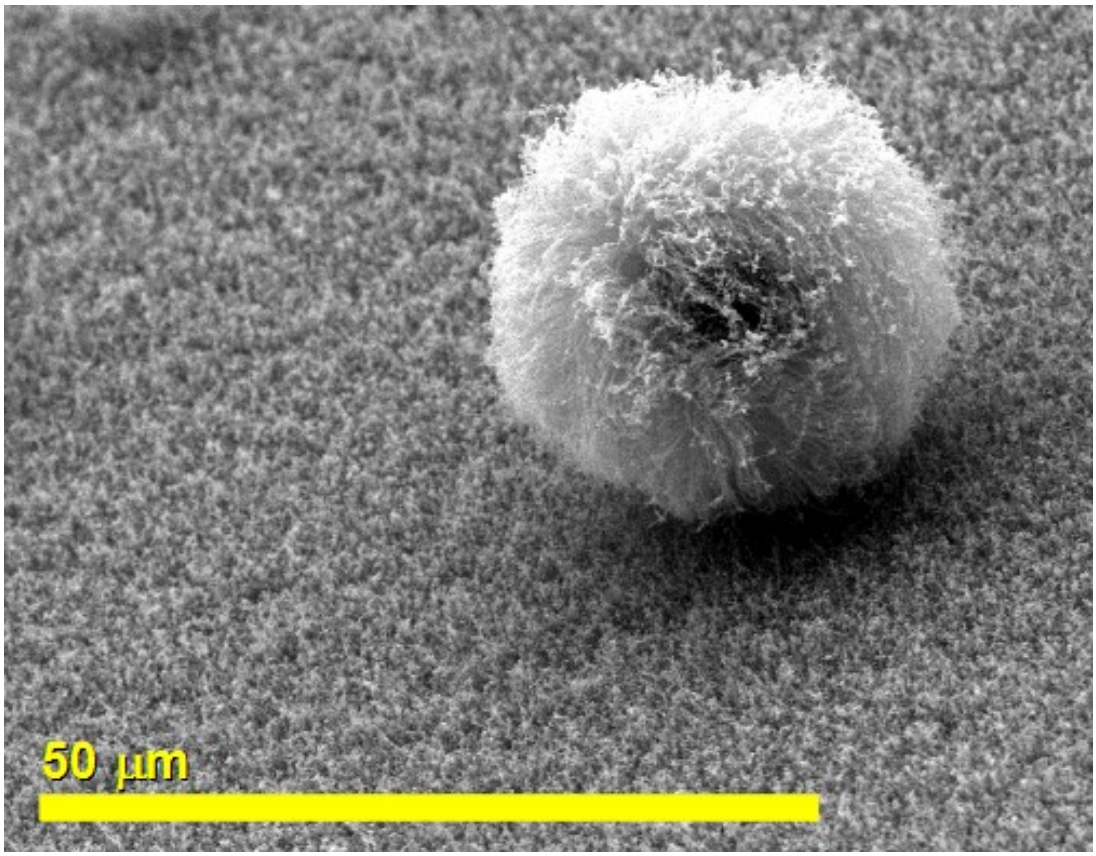

Fig.31: Scanning electron micrograph (taken at 20 kV) showing a radial-structure comprising MWCNTs continuously filled with single-crystals of ferromagnetic α-Fe and Fe_3C departing from a central core particle.

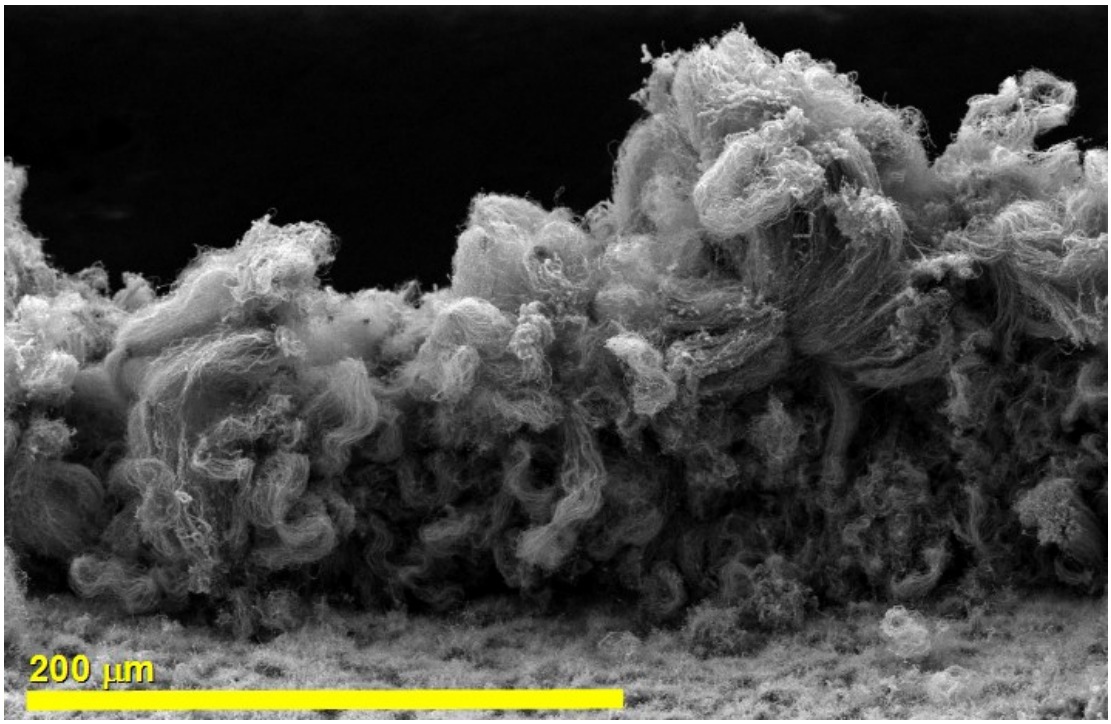

Fig.32: Scanning electron micrograph (taken at 20 kV) showing many radial-structures near the vapour-flow-facing edge of the substrate used for the MWCNTs deposition.

The very high filling ratio (> 90% of MWCNT core) of the radial MWCNTs and the spherical symmetry of these structures strongly pointed to the following preliminary conclusions:

i) The radial structures nucleate in the vapour

ii) The dense vapour created with the very low flow rate and high quantity of ferrocene has a very important role.

iii) The edge of the substrate has a fundamental role in the growth of these structures, by creating local-perturbations in the ferrocene/Ar vapour flow.

More experiments were performed to understand the role of the local-perturbation in the growth mechanism of these new radial-structures and to confirm these

preliminary conclusions. In these experiments the substrate geometry shown in Fig.33 was used. The dimensions of the quartz substrates were: length ~ 30 mm, width ~ 17 mm, thickness ~ 1.5 mm. The dimensions of the Si/SiO_2 substrate were: length ~ 13 mm, width ~ 10 mm, thickness ~ 1 mm. The substrate was positioned in the best growth region where an optimum vapour pyrolysis can be reached (at a vapour flow rate ~ 12 ccm): between 8.5cm and 11.5cm.

The results of these experiments were revealed by scanning electron microscopy (SEM) investigations of the substrates extracted from the reactor. Fig.34 shows the scanning electron micrograph of the radial structures deposited on the surface of the vertical Si/SiO_2 substrate while Fig.35 shows a top view of the same area. The radial-structures were also observed on the top of closely packed arrays of MWCNT grown on the horizontal surface of the quartz substrate shown in Fig.33 (see Fig.36).

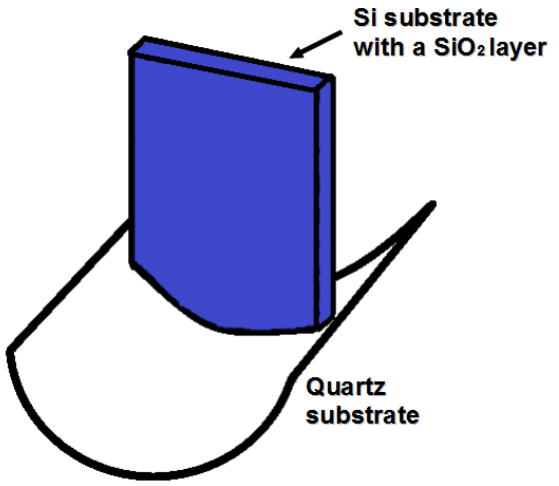

Fig.33: Schematic diagram showing the new substrate geometry used for the preliminary investigations of the radial structures to verify the presence of a local perturbation in the ferrocene/Ar vapour flow.

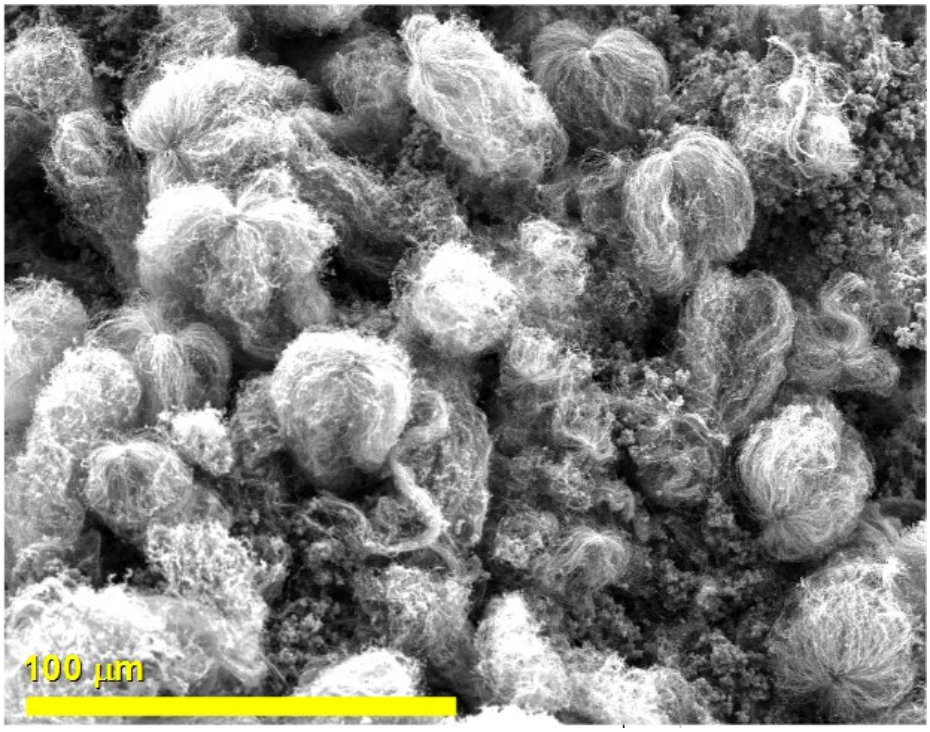

Fig.34: Scanning electron micrograph (taken at 20 kV) showing many radial structures deposited on the vertical surface of the Si/SiO_2 substrate.

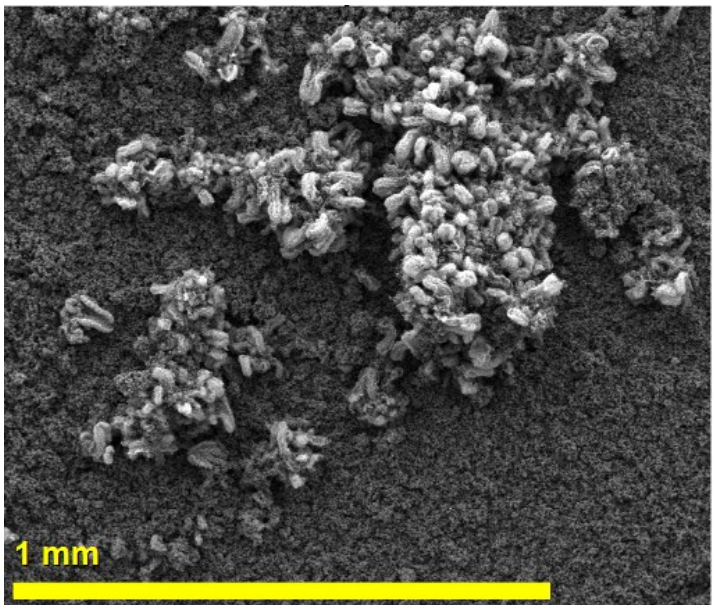

Fig.35: Scanning electron micrograph (taken at 20 kV) showing a top view of many radial structures deposited on the vertical surface of the Si/SiO_2 substrate.

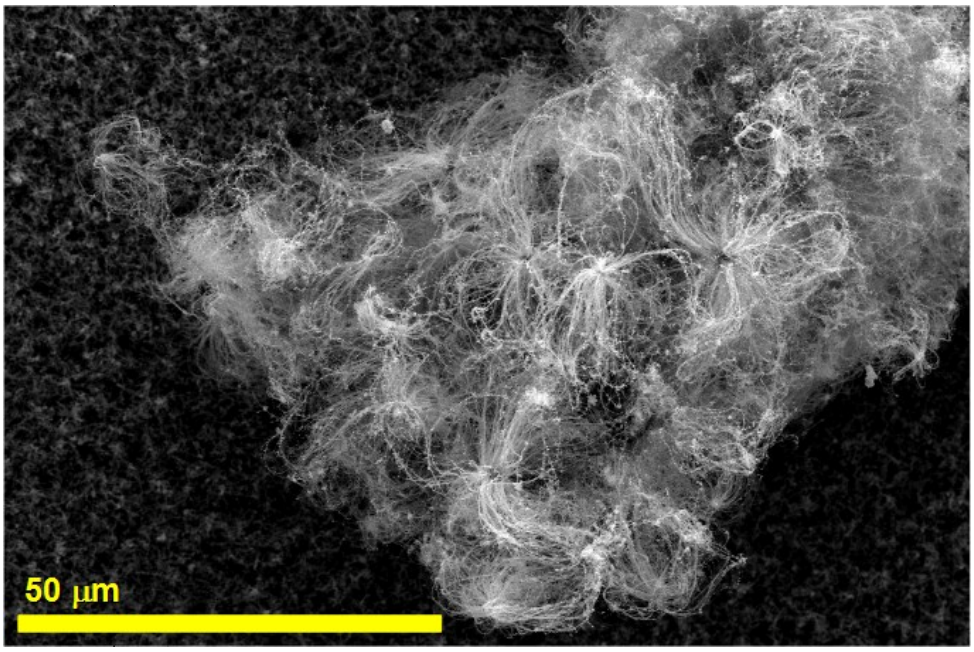

Fig.36: Scanning electron micrograph (taken at 20 kV) showing many radial structures deposited on the top of closely-packed vertical arrays grown on the horizontal surface of the quartz substrate shown in Fig.33.

The results obtained from these experiments suggest that the generation of a local perturbation in an ferrocene/Ar laminar vapour flow can induce the growth of MWCNTs continuously filled with single crystals of α-Fe in ways that were not achievable with the conventional steady-state CVD method. An example of the continuous filling can be observed in Fig.37. While the local-perturbations created with the two substrate-geometries in Fig.27 and in Fig.33 can be visualized in two schematic diagrams shown in Fig.38 and Fig.39. As shown in Fig.38 and Fig.39 the perturbations can be considered as consisting of randomly fluctuating eddies in the proximity of the vapour-flow-facing edge (Fig.38) and of the vapour-flow-facing surface of the vertical Si/SiO_2 substrate in Fig.39. The region where these randomly fluctuating eddies exist is defined as ‘‘viscous boundary layer region’’.

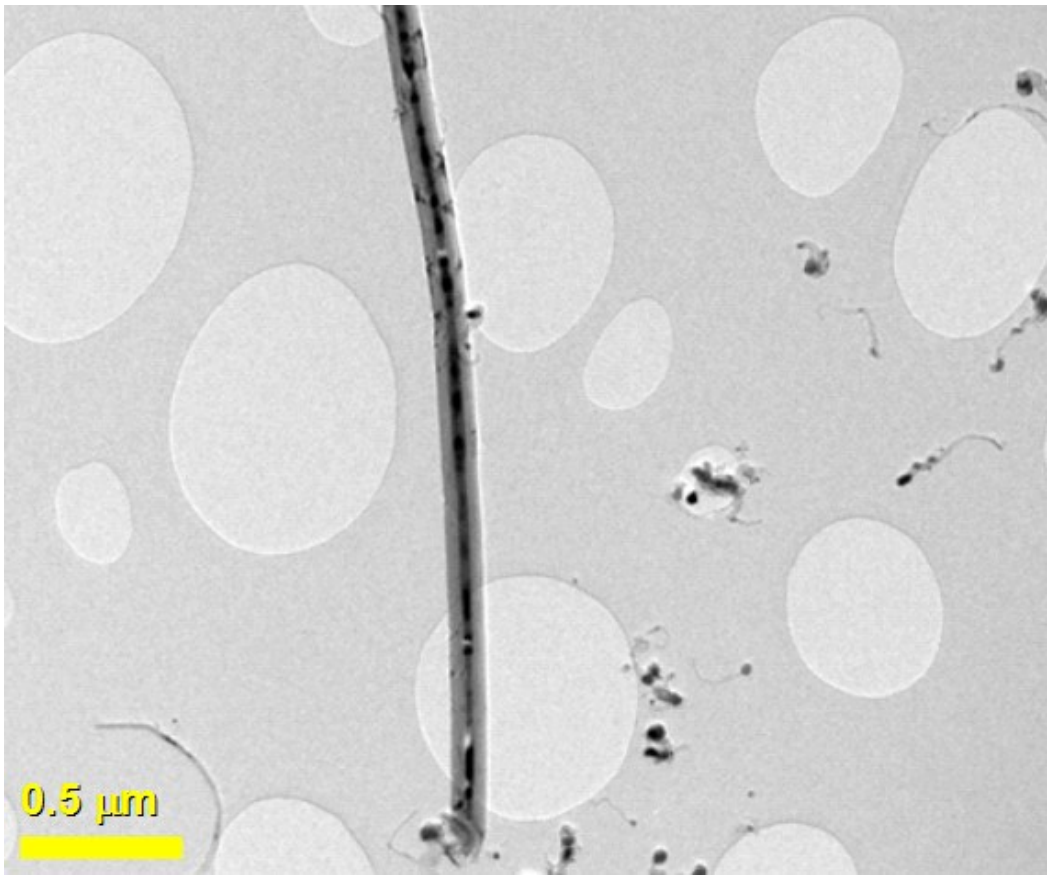

Fig. 37: Transmission electron micrograph (taken at 200 kV) showing a typical example of MWCNT (detached from a radial structure) continuously filled for ~ 12 µm.

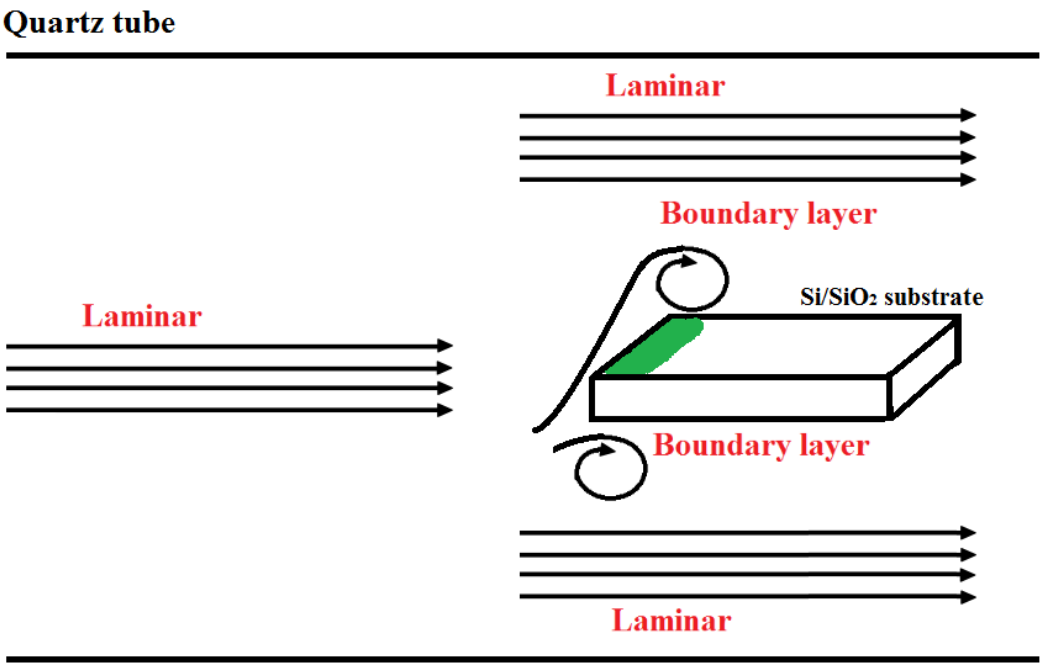

Fig. 38: Schematic diagram showing the viscous boundary layer (eddies) created by the vapour-flow-facing edge of the Si/SiO_2 substrate. This viscous boundary layer is responsible of the formation of the radial structures in the vapour. These structures deposit on the vapour-flow-facing edge of the substrate (green area). The average Reynolds number for the ferrocene vapour flow was estimated to be *Re*=2-4

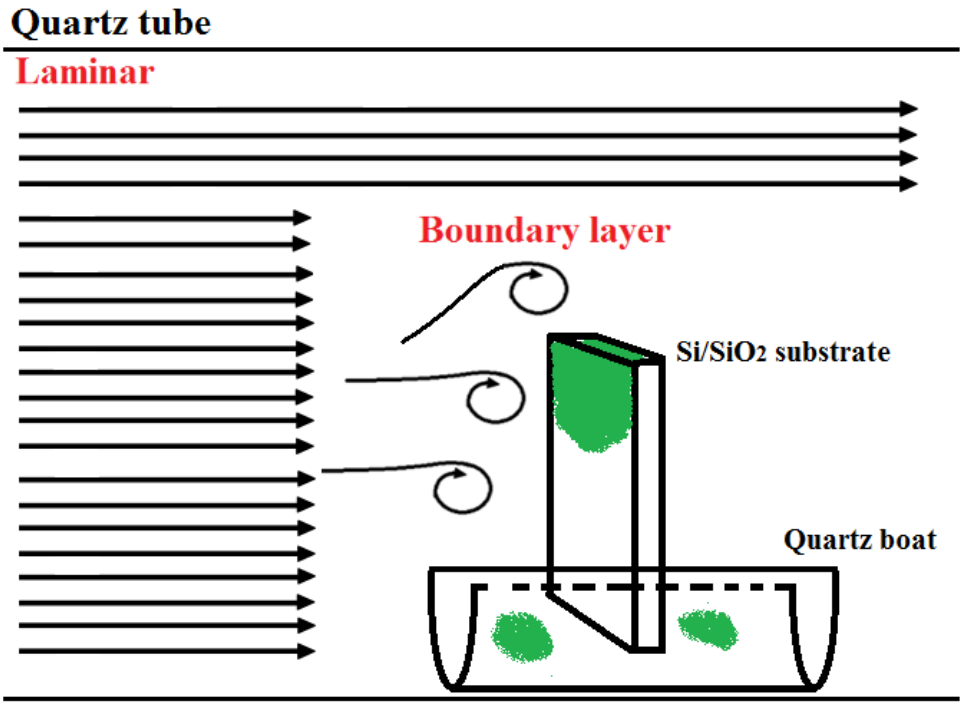

Fig.39: Schematic diagram showing the viscous boundary layer created by the vertical Si/SiO_2 substrate in the geometry shown in Fig.33. This local-perturbation is responsible of the formation of the radial structures that will deposit on the vertical and horizontal surfaces of the Si/SiO_2 and quartz substrates (green areas), as shown in Figs.34-36. The average Reynolds number for the ferrocene vapour flow was estimated to be *Re*=2-4.

These first observations lead to the development of two new methods of filled MWCNTs synthesis: the boundary layer chemical vapour synthesis and the locally perturbed vapour chemical vapour deposition. In the first method, the introduction of a rough quartz surface in the synthesis method described above yelded thick deposits of radial structures comprising MWCNT continuously filled with ferromagnetic single crystals of Fe_3C and α-Fe.

The rough quartz surface creates randomly fluctuating eddies in the pyrolyzed ferrocene vapour close to the substrate surface (viscous boundary layer).

The fluctuating eddies created by a single layer of deposited radial structures are comparable to those created by the asperities in the rough surface, so the reaction is self-sustaining. In the second method flower-like structures comprising MWCNTs continuously filled with α-Fe were produced through the creation of local-perturbation in a dense laminar ferrocene ($Fe(C_5H_5)_2$) vapour flow. The local perturbation, created by the small-hole in the quartz substrate (previously used to accommodate the vertical Si/SiO_2 substrate shown in Fig.33), induces the homogeneous nucleation of nanoparticles in the dense vapour. The nanoparticles, once deposited on the substrate surface, subsequently nucleate flower-like structures comprising MWCNTs continuously filled with Fe-based single crystals.

3.2 The origin of anomalously long lattice-spacings in Fe-based single crystals

Since 2006, the observation of MWCNTs filled with Fe-C phases [11] exhibiting anomalously long lattice spacings has caused confusion since reflections from lattice spacings of ≥0.4 nm are kinematically forbidden for α-Fe, γ-Fe, Fe_3C, and most of the rarely observed, less stable carbides. In different reports these reflections were ambiguously assigned to unknown Fe-C phases, unusual superstructures, or to Fe_3C [17,7,11,66,67].

In this subchapter we demonstrate that the anomalously long lattice spacings of 0.49 nm, 0.66 nm and 0.44 nm correspond to reflections from the (100), (010) and (001) planes of orthorhombic Fe_3C (space group *Pnma*). Observation of these forbidden reflections results from dynamic scattering of the incident beam as first

observed in bulk Fe_3C crystals. With small amounts of beam tilt these reflections can have significant intensities for crystals containing glide planes such as Fe_3C with space groups *Pnma* or *Pbmn*.

During HRTEM and TEM investigations of the MWCNT filling we frequently observed the anomalously long lattice spacings of 0.49 nm, 0.66 nm and 0.44 nm. These lattice spacings are much longer with respect to those present in the frequently observed Fe_3C [ICSD Ref. Code 16593], and the rarely observed less stable carbides Fe_2C [ICSD Ref. Code 76826], Fe_7C_3 [ICSD Ref. Code 167346], $Fe_{20}C_9$ [ICSD Ref. Code 740753] and $Fe_4C_{0:63}$[ICSD Ref. Code 9860]. Lattice spacings of 0.57 nm and 0.42 nm are expected for the rare stable carbide Fe_5C_2 [ICSD Ref. Code 76829 and 245334], while lattice spacings of >0.21 nm are not expected for α-Fe [ICSD Ref. Code 64795] and γ-Fe [ICSD Ref. Code 53803].
Typical examples of the HRTEM images which exhibit anomalously long lattice spacings, together with the SAED patterns and fast Fourier transform (FFT) data, are shown in Figs. 40-42. The lattice spacings of 0.49 nm and 0.19 nm, shown in Fig. 40, are close to the (100) and to the (031) planes of orthorhombic Fe_3C with space group *Pnma*, respectively. The spacings of 0.66 nm and 0.24 nm, shown in Fig. 41, correspond to the reflections from the (010) and the (200) planes of Fe_3C, respectively. The lattice spacing of 0.49 nm in Fig. 42 is close to the (100) plane of Fe_3C while the spacing of 0.44 nm could match the reflections from the (001) plane of Fe_3C. The main problem in this assignment of planes, is that the observation of the (100), (010) and (001) planes of Fe_3C would be kinematically forbidden by the selection rules imposed by the crystal symmetry of orthrohombic Fe_3C with space group *Pnma* or *Pbnm*.

These selection rules allow only certain kinematic reflections to be observed. For orthorhombic Fe_3C with space group *Pnma*, (typical unit cell parameters are labelled *a*=0.509 nm, *b*=0.675 nm and *c*=0.452 nm) the only allowed reflections are (h00) with h=2n, (0k0) with k=2n, (00l) with l=2n, (0kl) with k+l=2n and (hk0) with h=2n, where n is an integer [ICSD Ref. Code. 16593].

These rules are also valid for the Fe_3C with space growp *Pbnm* that differs from *Pnma* Fe_3C only in the labelling of unit cell parameters [ICSD Ref. Code 43375]. The reflections that are not allowed by the selection rules are known as ‘‘kinematical forbidden reflections”. These arguments are generally valid when the intensity of the diffracted beam is small compared to that of the incident beam (kinematic diffraction) [68,86,87]. If the intensity of the diffracted beam increases (as in the case of HRTEM), the dynamic scattering of the diffracted beams by atoms in a crystalline specimen should be considered. This is valid for crystals containing glide planes or screw axes, where, forbidden reflections may appear or disappear owing to slight changes of the incident beam direction. Observation of significant forbidden reflection intensities in electron diffraction studies of bulk Fe_3C with space group *Pbnm* was first reported by Nagakura *et al* [88]. It was shown that the 001 forbidden reflection intensity increased with the incident beam angle relative to a principal crystal axis and became significant after 0.5° of tilt.

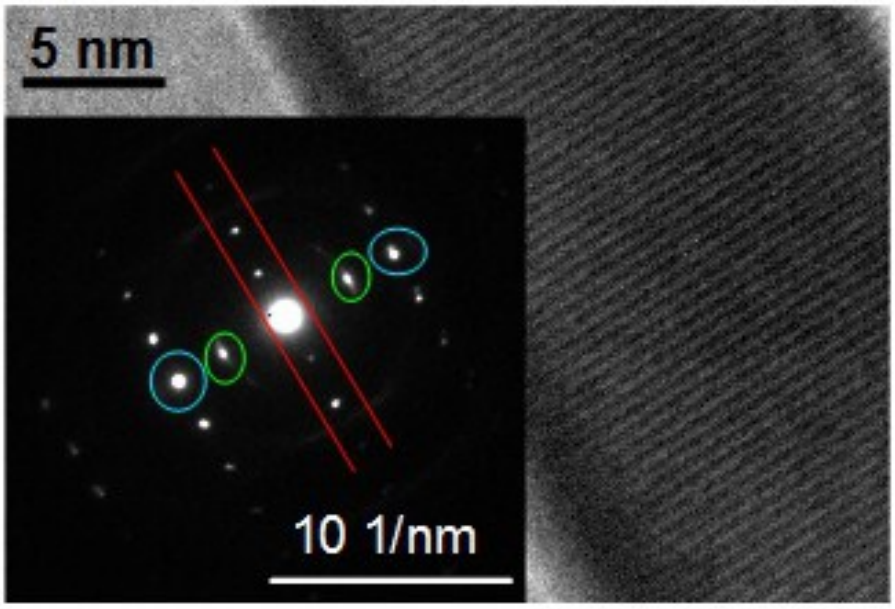

Fig.40: HRTEM micrograph of a Fe_3C single-crystal (taken at 200 kV). In the inset, the reciprocal lattice reflections obtained by electron diffraction (SAED) are shown. The forbidden 100 reflections of Fe_3C (between the red lines) correspond to the lattice spacing 0.49 nm. The blue circles indicate the allowed 031 reflections of Fe_3C corresponding to the lattice spacing 0.19 nm. The green circles indicate the 002 reflection of the graphitic MWCNT walls (lattice spacing of 0.34 nm). The beam direction is [01-3].

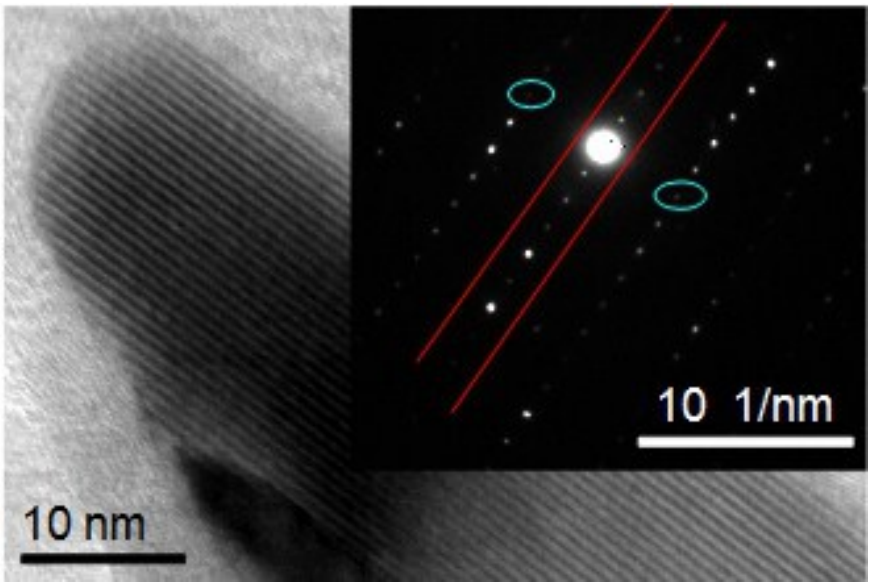

Fig.41: HRTEM micrograph of a Fe_3C single-crystal (taken at 200 kV). In the inset the reciprocal lattice reflections obtained by electron diffraction (SAED) are shown. The forbidden 010 reflections of Fe_3C (between the red lines) correspond to the lattice spacing 0.66 nm. The blue circles indicate the allowed 200 reflections of Fe_3C corresponding to the lattice spacing 0.24 nm. The beam direction is [001].

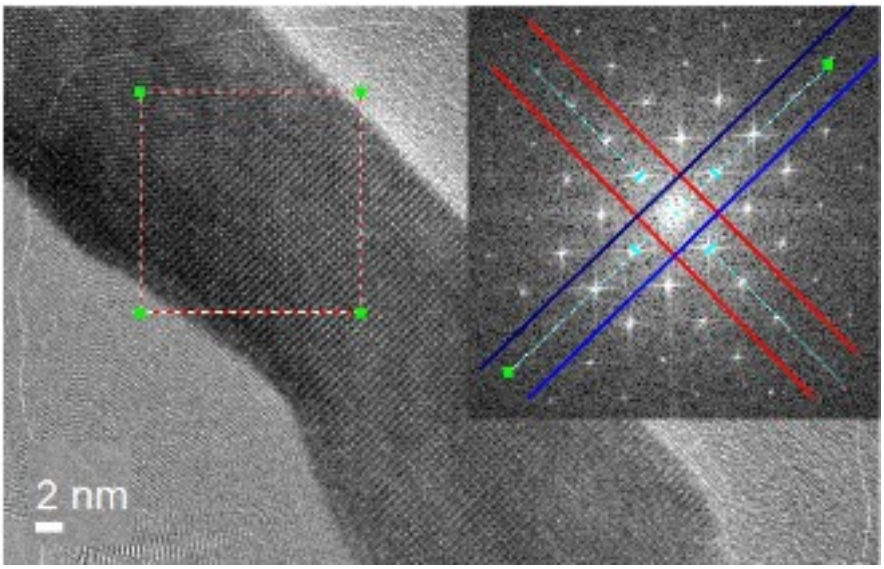

Fig.42: HRTEM micrograph of a Fe_3C single-crystal (taken at 300 kV). In the inset the reciprocal lattice reflections obtained by FFT (of the area within the red square) are shown. The forbidden 100 reflections of Fe_3C (between the red lines) correspond to the lattice spacing of 0.49 nm, while the forbidden 001 reflections (between the blue lines) correspond to the lattice spacing of 0.44 nm. The beam direction is [010].

Considering that the kinematic theory of diffraction is generally valid for almost all the X-ray analyses of thin crystals, XRD analyses were performed to understand the origin of the unusual lattice spacings. If the anomalously long lattice spacings of 0.49 nm, 0.66 nm and 0.44 nm observed by HRTEM corresponded to the forbidden 100, 010 and 001 reflections of Fe_3C, then no peaks should be observed in the range of Bragg angle associated with the anomalous crystal planes (low 2θ) [68,86,87]. As shown in Fig.43 no peaks were observed at low 2θ. The presence of Fe_3C was observed through the 211, 102 and 112 Bragg reflections (see Fig.44).

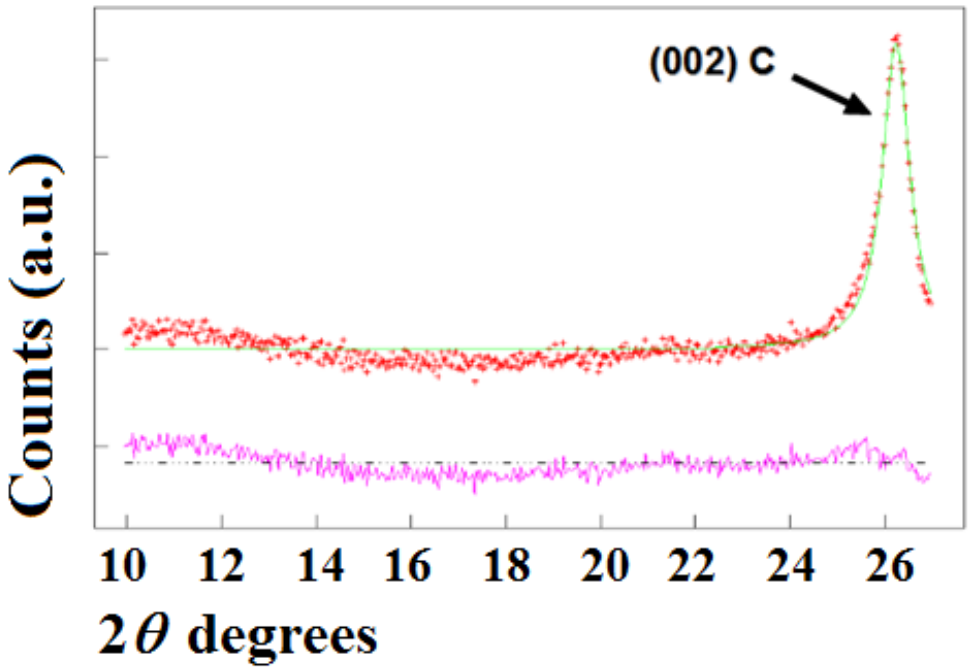

Fig.43: Low-angle XRD diffractogram and Rietveld refinement (green line) of the filled-MWCNT extracted from the reactor. No peaks are observed at low angle, the large peak corresponds to the (002) planes of the graphitic MWCNT walls. The light-violet line corresponds to the difference between the X-ray diffractogram data (red) and the refinement (green line).

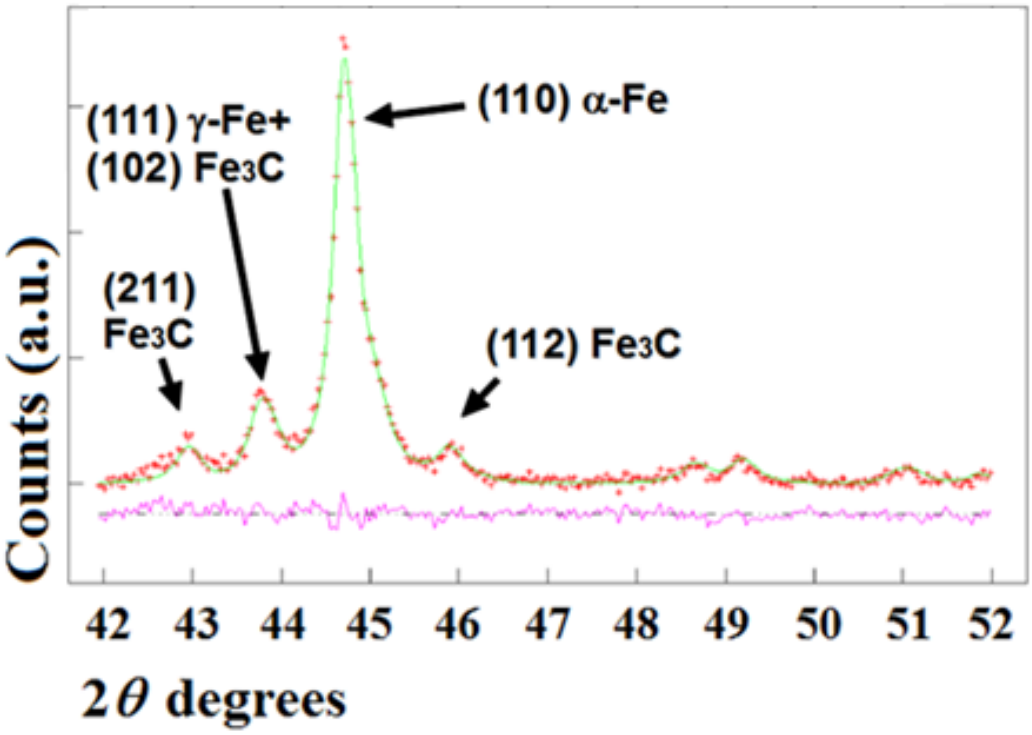

Fig.44: XRD diffractogram and Rietveld refinement (green line) from the filled-MWCNT extracted from the reactor. The relative abundance of the phases is 2.0% of γ-Fe cubic (*Fm-3m*), 20.1% of Fe_3C orthorhombic (*Pnma*) and 16.5% of α-Fe cubic (*Im-3m*). The light-violet line corresponds to the difference between the X-ray diffractogram data (red) and the refinement (green line).

The reflections from the lattice spacing 0.49 nm were then provisionally assigned to the (100) planes of Fe_3C, those from the lattice spacings 0.44 nm to the (001) planes of Fe_3C and those from the lattice spacing 0.66 nm to the (010) planes of Fe_3C. The consistency of the plane assignement was then checked using the Weiss zone law for the "beam direction", [UVW] [68].In the case of the (031) and the (100) planes shown in Fig. 40, the beam direction is [01-3] while in the case of the (200) and (010) planes shown in Fig. 41 the direction is [001], and by considering the (100) and the (001) planes shown in Fig. 42 the direction is [010]. The

appearence of the forbidden 100, 010 and 001 reflections is in agreement with the dynamic extinction rules outlined by Tanaka *et al.* [88-90]. An attempt was also made to observe the disappearence of the forbidden reflections by tilting the sample around the sample holder axis. A disappearance of the forbidden reflections had to be observed for beam directions exactly parallel to a principal axis [89-91]. This was investigated in two different filled MWCNT (in which the filling were showing the anomalously long lattice spacings) by tilting the sample around the sample-holder axis. In the first case, the anomalous lattice spacings disappeared after a tilt of 4.1°, and in the second case after a tilt 4.5°.

The consistency of this interpretation was then checked by chemical compositional analyses of the MWCNT filling by EELS.

Two averaged Fe-L_3/L_2 values, 3.1 and 3.4, were extracted from the MWCNT filling regions that did not show a anomalously long lattice spacing. The single case of MWCNT-filling that did exhibit a anomalously long lattice spacing, Fig.45, yielded the averaged Fe-L_3/L_2 ratio of 2.7 (averaging over ten spectra, a typical example is shown in Fig.46). The Fe-L_3/L_2 ratios previously reported in literature are 3.0 for α-Fe, 3.5 for γ-Fe, and 2.8 for Fe_3C [92-94]. So, in conclusion chemical compositional analyses confirm that the composition of the Fe-C crystals exhibiting anomalously long lattice spacings corresponds to Fe_3C. These analyses are in agreement with the HRTEM, SAD, and XRD interpretations outlined above. The observed anomalously long lattice spacings 0.49 nm, 0.66 nm and 0.44 nm correspond to the 100, 010 and 001 reflections of orthorhombic Fe_3C (Pnma), respectively. These reflections are kinematically forbidden. However, with small amounts of beam tilt these reflections can have significant intensities

for crystals containing glide planes such as Fe_3C with space groups *Pnma* or *Pbmn*.

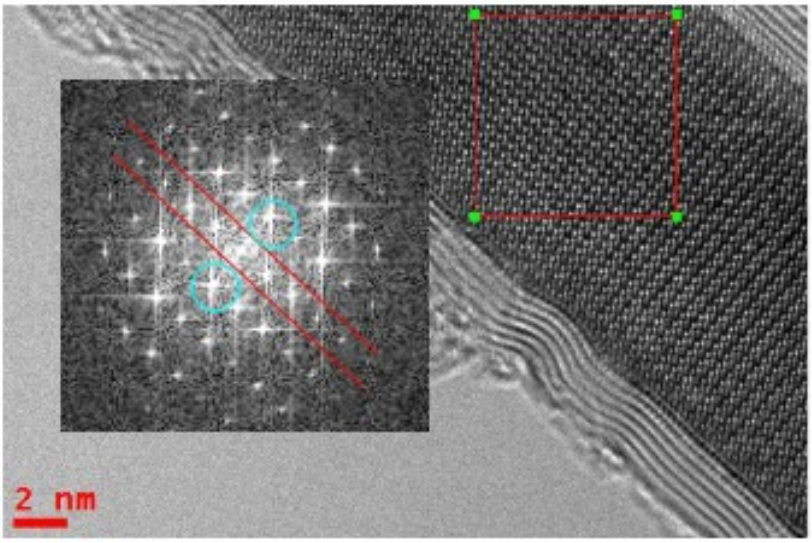

Fig.45: High resolution scanning TEM image of the Fe_3C single crystal used for the EELS analyses (taken at 80 kV). In the inset the reciprocal lattice reflections, obtained by FFT of the area delimited by the red square, are shown. The forbidden 100 reflections of Fe_3C (between the red lines) correspond to the lattice spacing of 0.51 nm. The blue circles indicate the allowed 011 reflections corresponding to the lattice spacing 0.39 nm. The beam direction is [0-11].

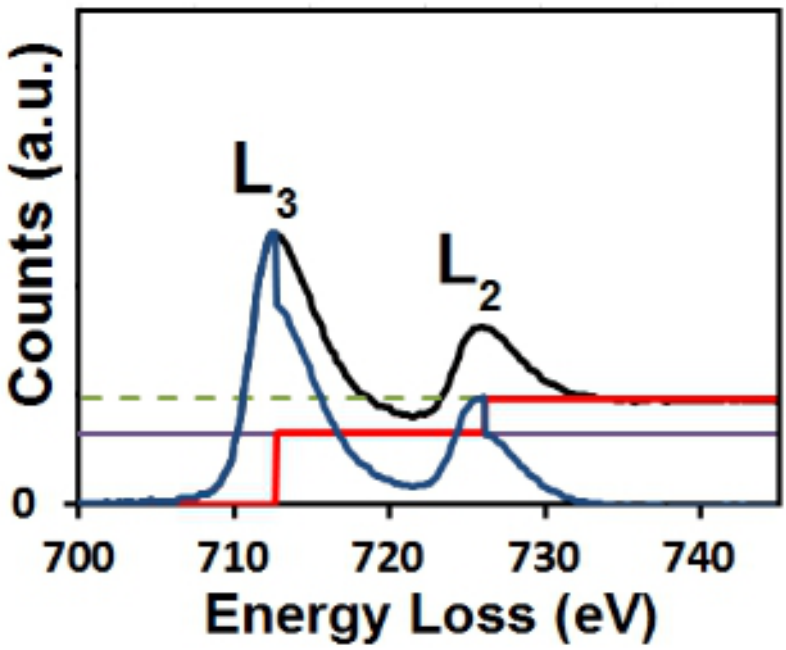

Fig.46: Typical EELS spectra of the Fe_3C single crystal from Fig. 45 before (black) and after (blue) the application of the Pearson method. The two step functions are shown with red color.

3.3 New synthesis methods

3.3.1 Boundary-layer chemical vapour synthesis method

As introduced in section 3.1, new radial-structures comprising MWCNTs continuously filled with single-crystals of ferromagnetic α-Fe and Fe_3C departing from a central core particle were serendipitously observed as product of the pyrolysis of a ferrocene vapour in an Ar flow of ~12 ccm. The nucleation of the structures was considered to be due to two main factors:

i) Local perturbations consisting of randomly fluctuating eddies in the proximity of the vapour-flow-facing edge of a Si/SiO_2 substrate (Fig.38) and in proximity of the vapour-flow-facing surface of a vertical Si/SiO_2 substrate (Fig.39).

ii) Homogeneous nucleation of nanoparticles in the dense vapour created with the very low flow rate and high quantity of ferrocene.

In this subchapter we show how the introduction of a rough quartz surface in the reaction system described in section 3.1, yelded thick deposits of radial structures comprising MWCNTs continuously filled with ferromagnetic single crystals of Fe_3C and α-Fe. The rough quartz surface creates randomly fluctuating confined eddies in the pyrolyzed ferrocene vapour close to the substrate surface (viscous boundary layer). We also demonstrate that the randomly fluctuating eddies produced by a first layer of radial structures are comparable to those created by the rough quartz surface. Therefore in these conditions the reaction is self-sustaining and could be used for industrial purposes. Two examples of the radial structures are shown in the SEM micrographs of Fig.47 and Fig.48. The average diameter of the radial structures was ~13 μm.

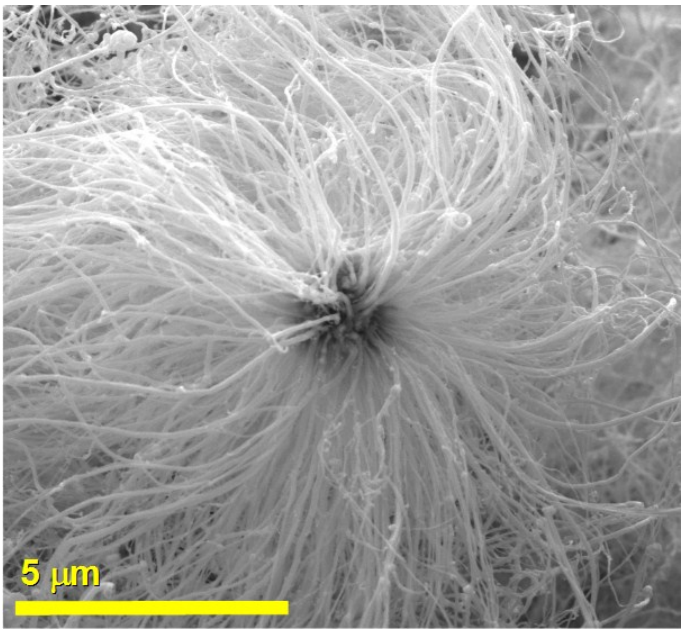

Fig.47: Scanning electron micrograph (taken at 20 kV) of a radial structure comprising radial continuously filled-MWCNTs departing from a central particle (obtained with a flow rate of ~ 11 ccm).

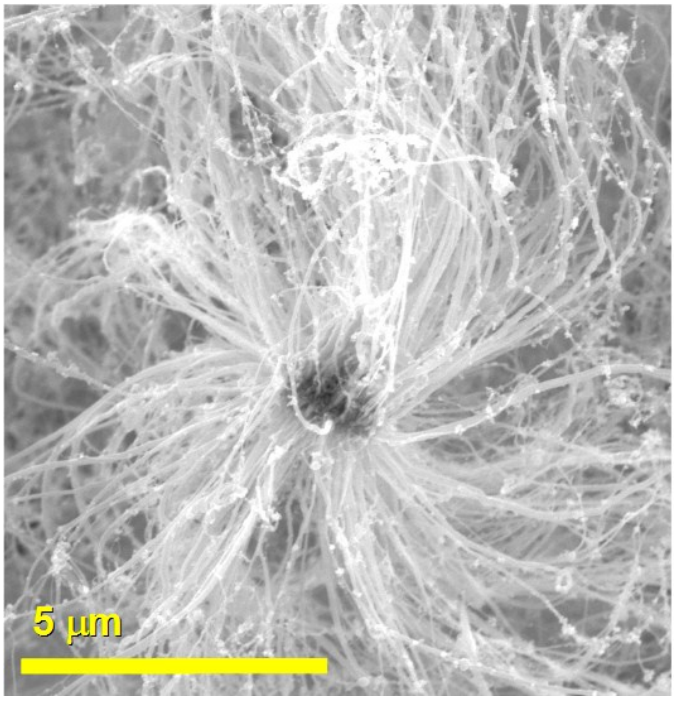

Fig.48: Scanning electron micrograph (taken at 20 kV) of another radial structure comprising radial continuously filled-MWCNTs departing from a central particle (obtained with a flow rate of ~ 11 ccm).

The vapour flow on the scale of the roughness is dominated by viscous forces which result in non-zero lateral vapour velocity at the tips of asperities and randomly fluctuating, confined eddies. This can be visualized in the schematic diagram shown in Fig.49 and is valid for the fluctuating eddies obtained between vapour flow rates of 3.5 and 12.5 ccm. As shown in Fig. 50, thick deposits of radial structures were observed after each synthesis. The thickness of the deposit was many times the diameter of an individual radial structure. The deposited radial structures were easily mechanically or magnetically removed and dispersed in methanol. The ease of removal suggests weak adhesion to the rough quartz surface, weak inter-structural forces, and no covalent cross-linking.

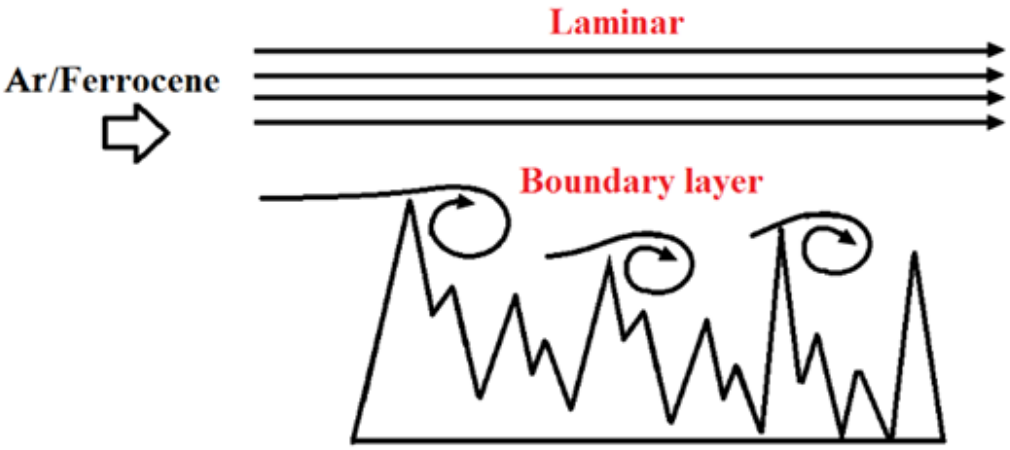

Fig.49: Schematic diagram of the viscous boundary layer between the rough surface of a quartz substrate and the laminar ferrocene/Ar vapour flow. The vapour flow is dominated by viscous forces which result in non-zero lateral velocity at the tips of asperities and fluctuating, confined eddies.

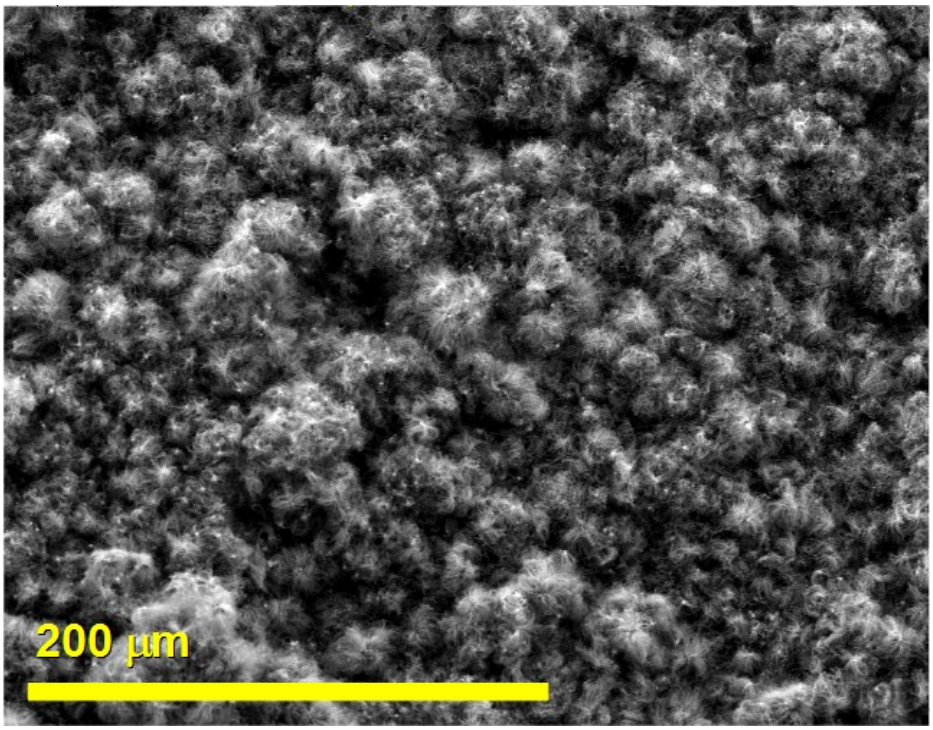

Fig.50: SE micrograph (taken at 20 kV) showing an as grown thick deposit of radial structures.

The spherical symmetry of both the core and the complete individual radial structures, and the above observations strongly point to the following conclusions:

i) the complete structure was spontaneously nucleated and formed in the boundary layer region.

ii) the radial structures growth is 'switched off' by contact with the surface or with a layer of already deposited radial structures.

iii) The vapour fluctuation created by the first layers of radial structures deposited on the roughened surface is comparable to that of the original rough surface; the reaction conditions are therefore self-sustaining and scalable.

These conclusions are also confirmed by the experiments performed with a rough/flat surface showing the boundary between the two growth modes and

underlining the importance of the viscous boundary layer between the rough surface of a quartz substrate and the laminar ferrocene/Ar vapour flow (see Fig. 51). The vapour flow in the rough region of the substrate will be dominated by viscous forces resulting in randomly fluctuating, confined eddies. Differently no confined eddies will be present in smooth regions of the substrate.

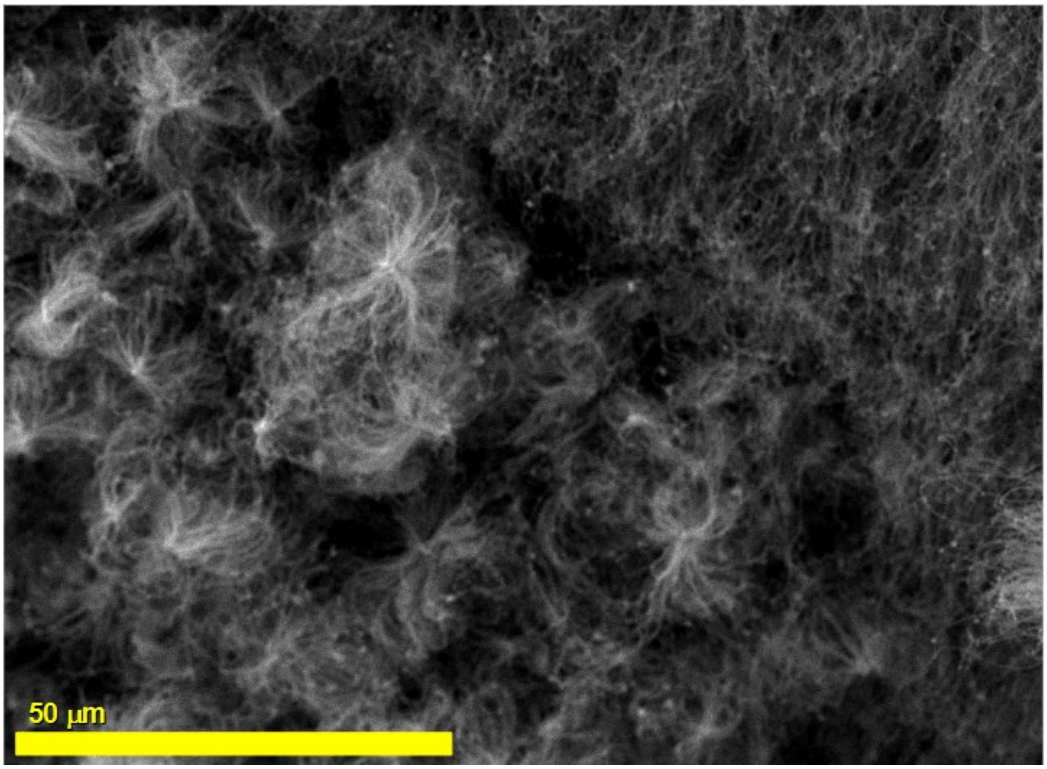

Fig.51: A scanning electron micrograph (taken at 20 kV) showing a distinct vertical-to-radial growth region at smooth-rough quartz substrate boundary: the upper-right region is the top view of a vertical array of filled-multiwall carbon nanotubes grown perpendicular to the smooth quartz surface, and the lower-left is that of layers of free-standing radial structures on the rough quartz surface.

One of the principal advances in the understanding of non-equilibrium thermodynamic systems is that the onset of self-organization is dictated by the

behavior of fluctuations [95]. This means that order can be propagated by amplification of these fluctuations through a feedback mechanism involving the interaction with the global environment. In this section we show that the nucleation and subsequent growth of these radial structures results from fluctuation-amplification by exchange of vapour feedstock and thermal energy with the laminar flow region. The complex morphology of the radial structures was observed by TEM investigations. Two typical examples of radial structures observed by TEM are shown in Fig.52 and Fig.53. Analysis of fifty central particles revealed that the majority had diameter 1.5±0.3 μm; the minimum and maximum observed diameters were 0.4 and 3 μm, respectively. The central particle (the point of departure for the radial continuously filled MWCNT) is an agglomeration of approximately spherical nanoparticles (onions) of 100 - 150 nm diameter comprising single crystals of Fe or Fe_3C encapsulated by graphitic shells with an inter-shell spacing of 0.33 nm (see Fig. 54 and Fig. 55). Owing to the thickness of the spherical nanoparticles agglomeration, in some cases the core can not be observed with high detail.

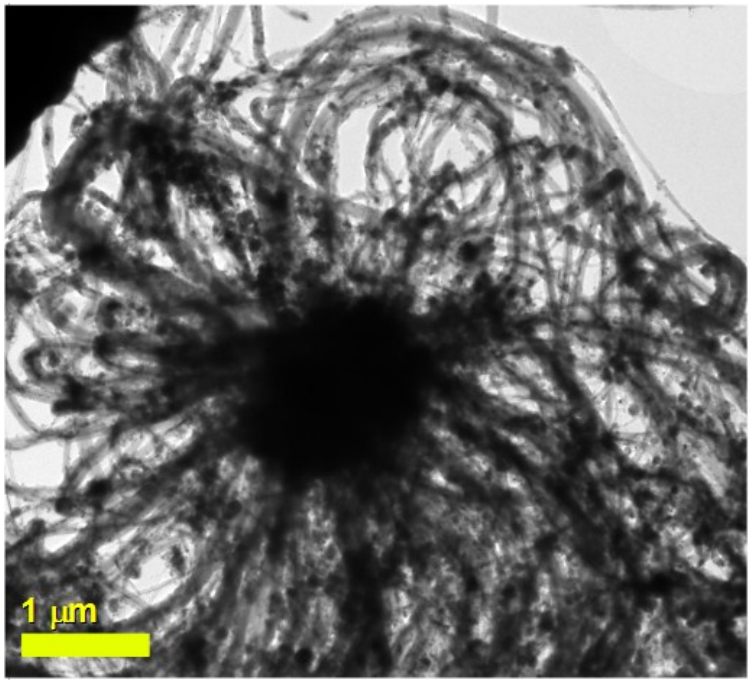

Fig.52: TEM micrograph (taken at 200 kV) showing the cross section of a typical radial structure obtained at a flow rate of ~7 ccm.

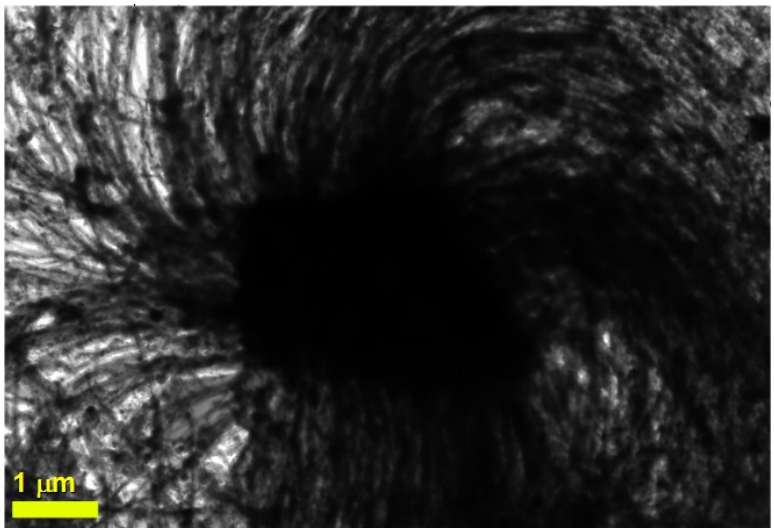

Fig.53: TEM micrograph (taken at 200 kV) showing the cross section of another typical radial structure obtained at a flow rate of ~ 15 ccm.

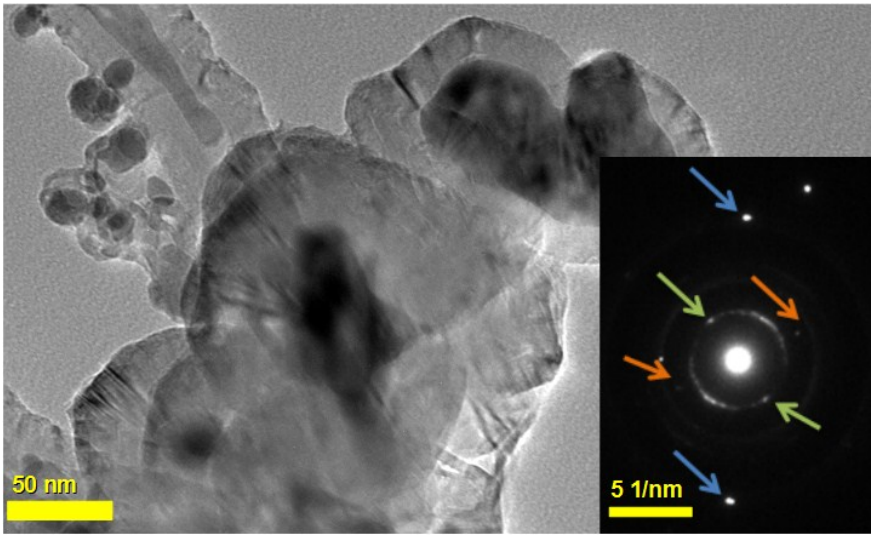

Fig.54: Transmission electron micrograph (taken at 200 kV) of small particles (diameter ~100 nm) observed in the core of a small radial structure. Inset: selective area electron diffraction pattern obtained from one of the spherical particles. The orange arrows indicate a lattice spacing of 0.25 nm corresponding to the (200) plane of Fe_3C. The blue arrows indicate a lattice spacing of 0.11 nm corresponding to the (303) plane of Fe_3C. The green arrows indicate the spots corresponding to the (002) lattice planes of graphite with spacing 0.33 nm.

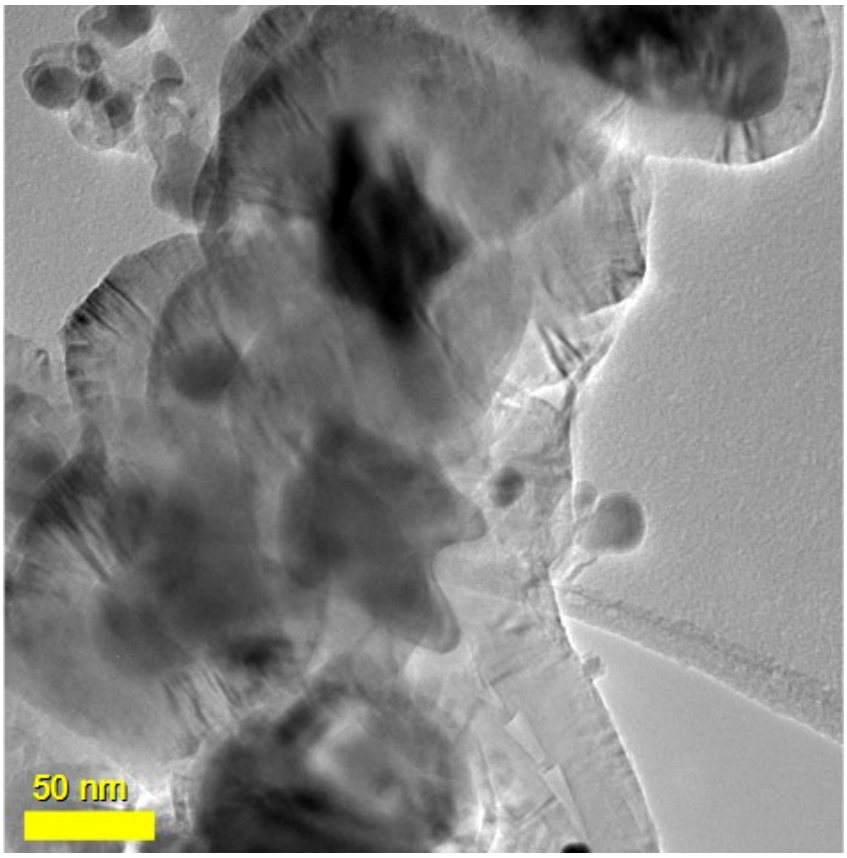

Fig.55: Transmission electron micrograph (taken at 200 kV) showing more small particles (diameter ~100 nm) observed in the core of a small radial structure.

As written above the radial structures comprise MWCNTs continuously filled with Fe-based single crystals. This can be observed in the sequence in Fig. 56. Furthermore, in many cases the single-crystal filling exhibits a preferential orientation with respect to the MWCNT long axis. An example is shown in the sequence in Fig. 57, where, in the TEM micrographs it is shown a Fe_3C single crystal filling continuously a MWCNT. As shown by the turquoise circles in the SAED (indicating the 112 reflection of Fe_3C corresponding to a lattice spacing of 0.195 nm) the Fe_3C single crystal shows a preferred orientation with respect to the MWCNT long axis for the length of 7 μm. In A (i) also the 120 and 240 reflections of Fe_3C are observed, while in B (i) only the 112 reflections are

present. Interestingly, the 240 reflections of Fe_3C are again observed in the ending part of the filling (see Fig.57 E(i)). This could suggests that the single crystal, after certain distances during the filling process, could rotate with a spiral-like motion.

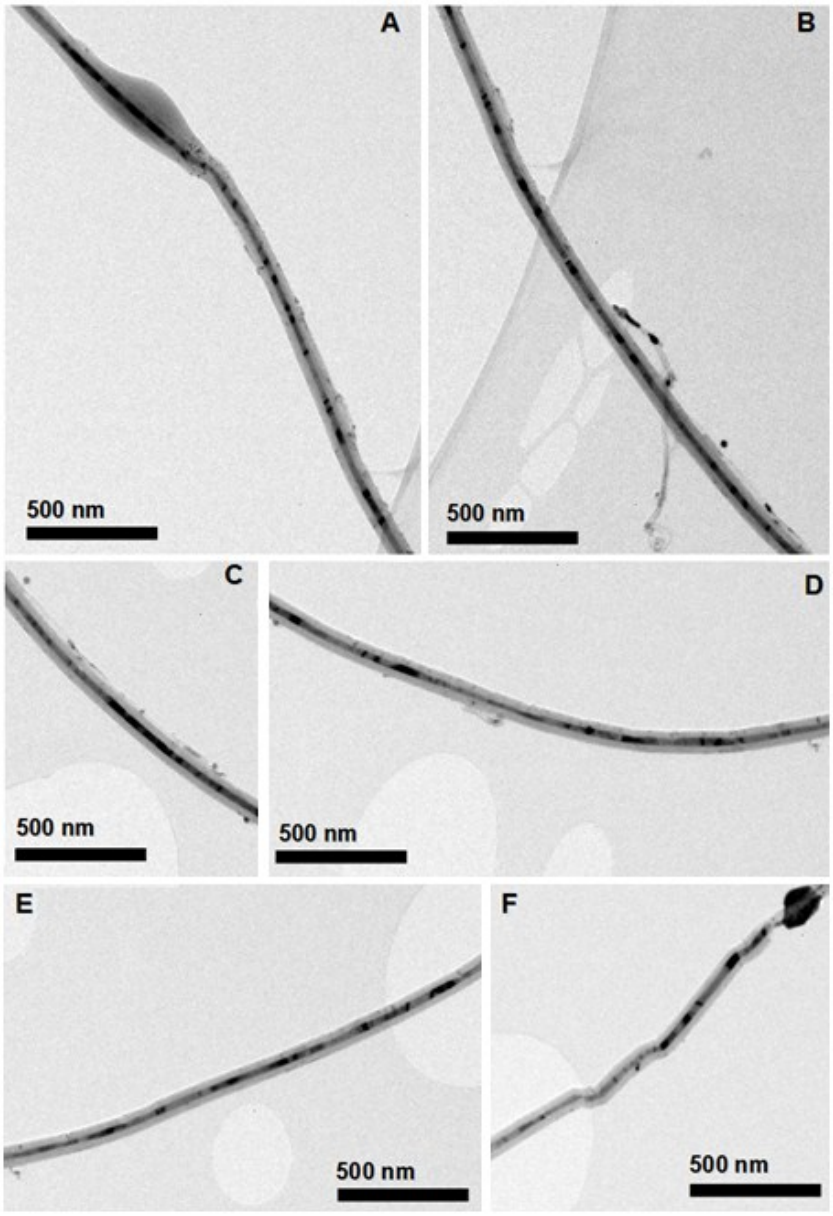

Fig.56: The A-F sequence of transmission electron micrographs (taken at 200 kV) follows a single continuously filled-MWCNT; the filling is continuous for ~9μm. The swelling feature in micrograph F is due to electron beam damage that resulted from the long exposure time needed to complete the sequence.

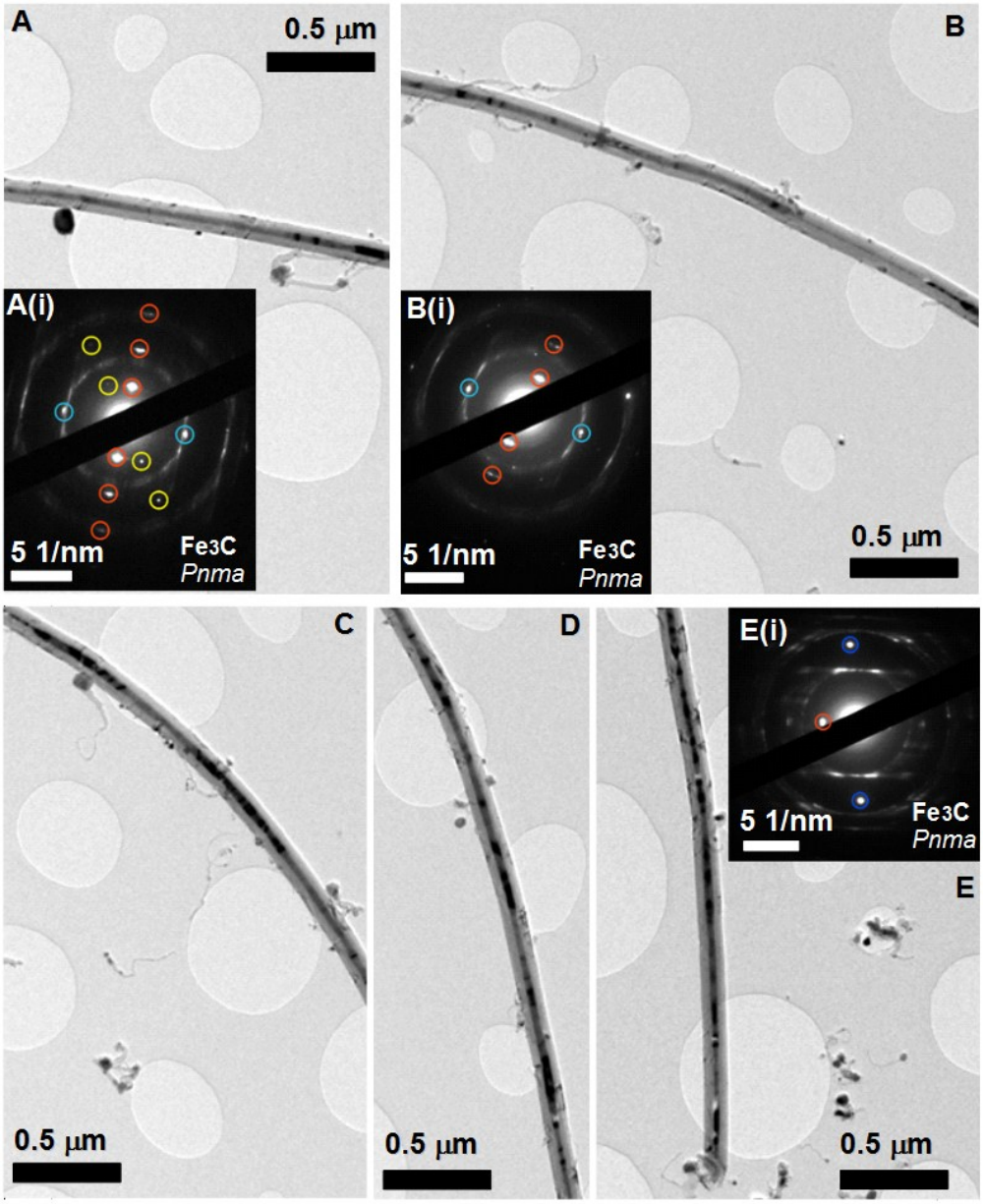

Fig.57: The A-E sequence of transmission electron micrographs (taken at 200 kV) follows a continuously filled MWCNT; the filling is continuous for ~12μm. In the insets (A(i),B(i) and E(i)) the SAED analyses of the filling structure reveal the reflection of orthorhombic Fe_3C. In A(i) and B(i): the turquoise circles indicate the 112 reflection of Fe_3C, the orange circles indicate the 002, 004 and 006 (visible only in A(i)) reflections of the MWCNT, the yellow circles (in A(i)) indicate the 120 and 240 reflections of Fe_3C. In E(i) only the 240 reflection of Fe_3C (indicated with the blue circles) is observed.

Interestingly the morphology of these radial structures changes with the vapour flow rate. TEM investigations revealed that with the increasing of the vapour flow rate from 3.5 ccm to 20 ccm the shape of the core becomes elongated, assuming a flattened shape (see Fig. 58 and Fig. 59). This elongated core is still composed of agglomerated spherical nanoparticles as shown in Fig. 60. The radial structures produced at 20 ccm still comprise MWCNT filled continuously along the core, as shown in Fig.61. However the structure appears more fragile with respect to those obtained at lower flow rates. This could be due to the different density of the vapour created at flow rates of ~ 20 ccm. The behaviour of the vapour flow at flow rates of 15-20 ccm can be qualitatively visualized in Fig. 62.

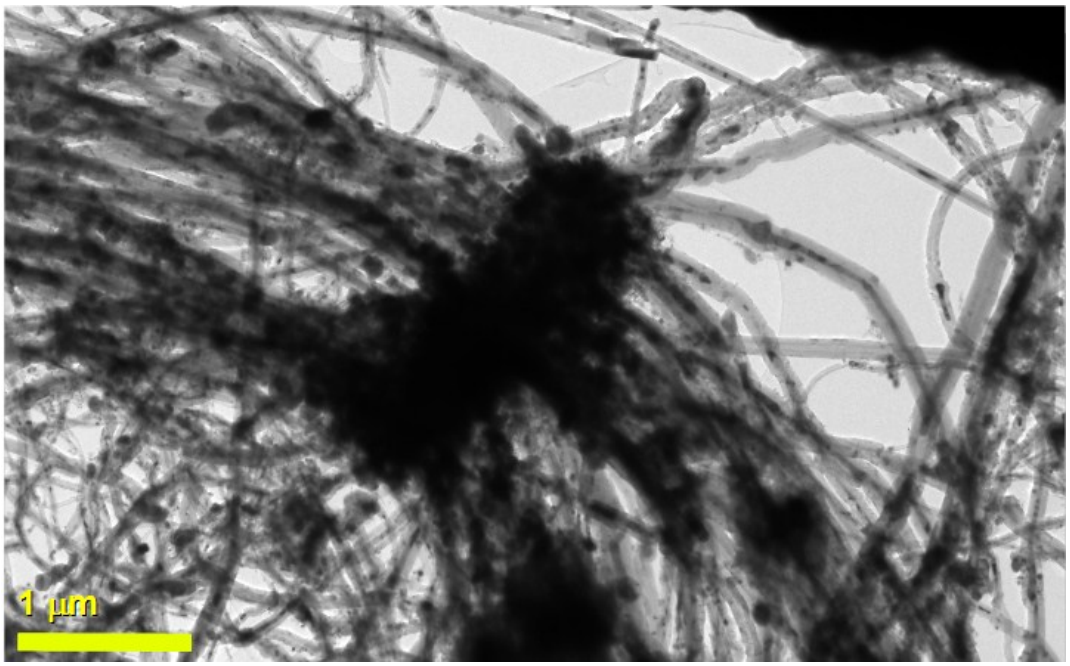

Fig.58: Transmission electron micrograph (taken at 200 kV) showing a radial structure obtained at vapour flow rates of 15 ccm. The core (agglomeration of spherical nanoparticles) clearly exhibits an elongated shape.

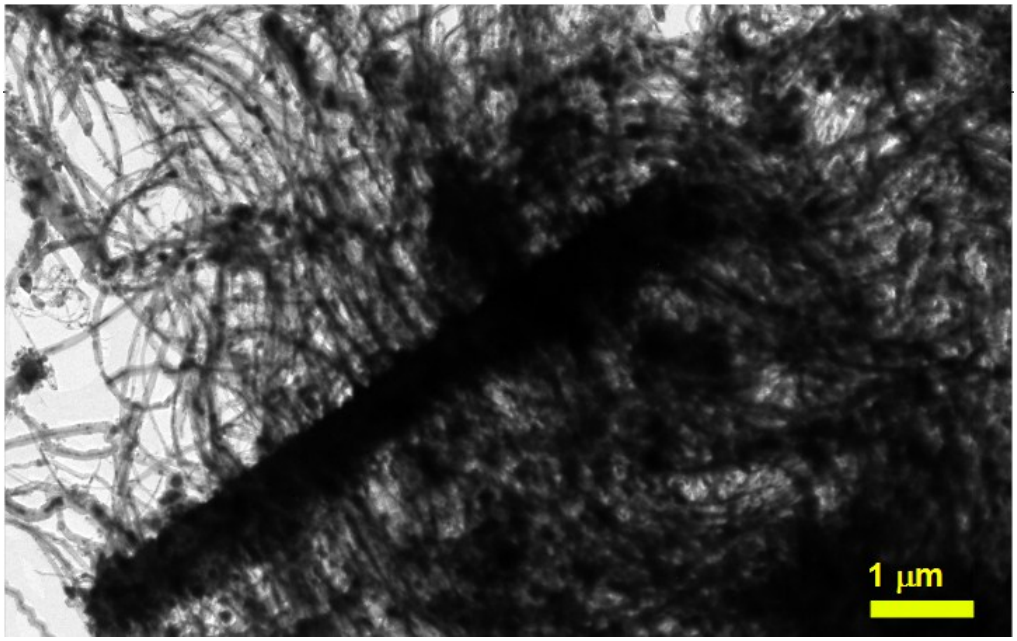

Fig.59: Transmission electron micrograph (taken at 200 kV) showing another radial structure obtained at vapour flow rates of 15 ccm. The core (agglomeration of spherical nanoparticles) presents a straight and elongated shape with a length of ~ 5 μm.

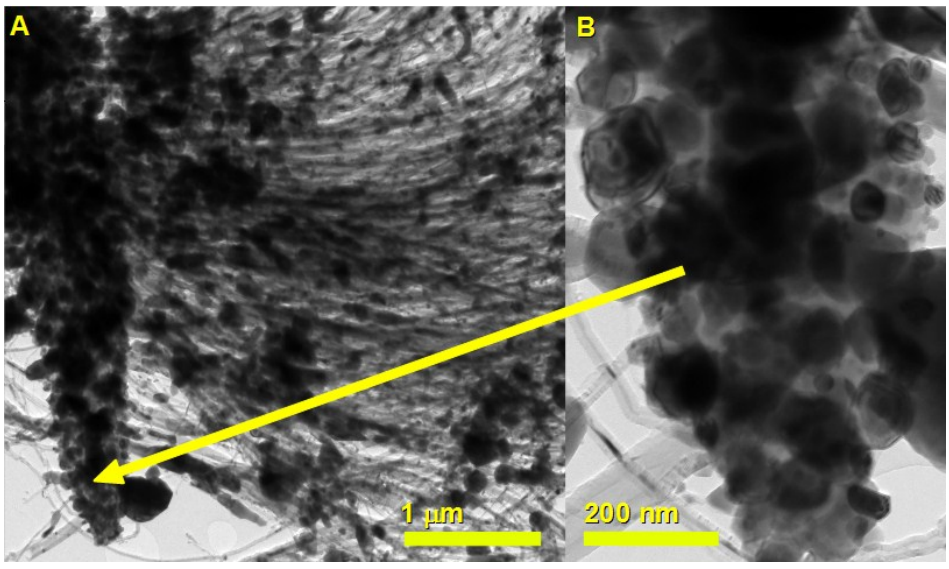

Fig.60: Transmission electron micrographs (taken at 200 kV) showing in A the elongated core (agglomeration of spherical nanoparticles) of a radial structure obtained at vapour flow rates of 20 ccm. In B a high detail of the core particles-agglomeration is shown.

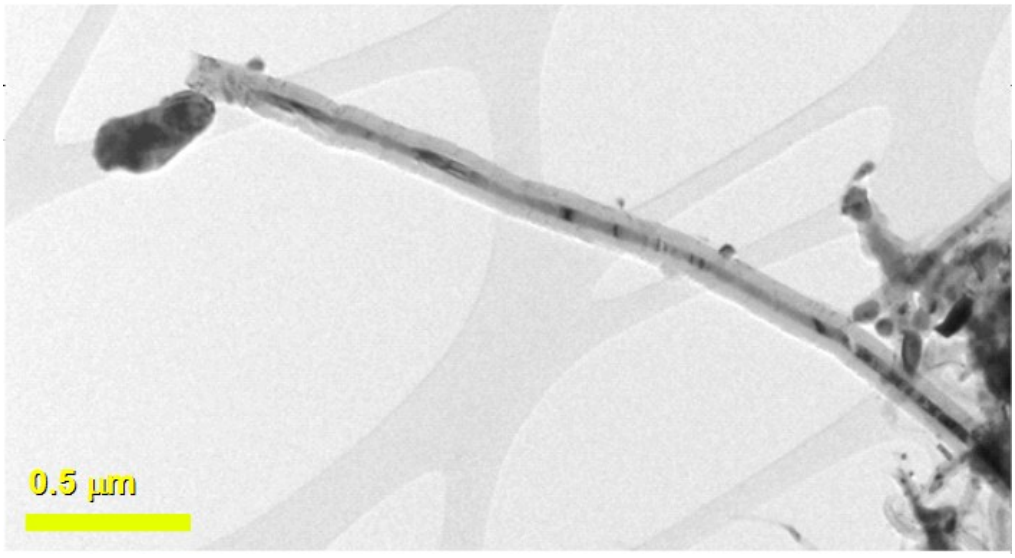

Fig.61: Transmission electron micrograph (taken at 200 kV) showing a continuously filled MWCNT. The MWCNT was detached from a radial structure obtained at vapour flow rates of 20 ccm.

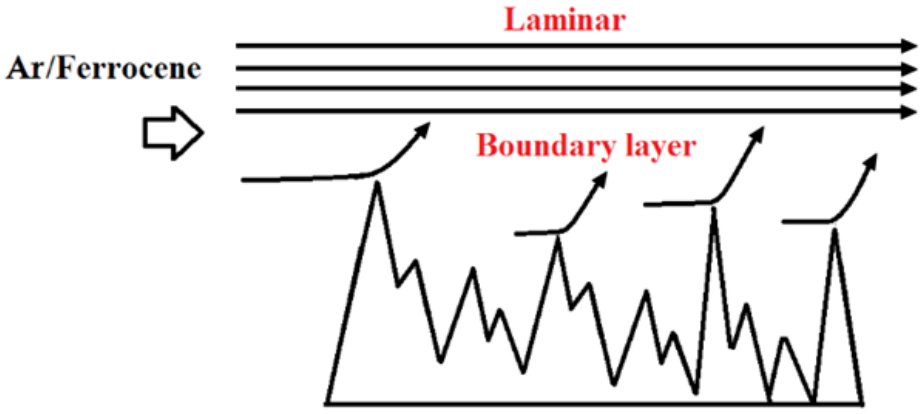

Fig.62: Schematic diagram showing the effect of higher vapour flow rates of 15-20 ccm in the confined eddies. The shape of the core particles suggests that at these flow rates the eddies are not confined. This schematic diagram could explain the elongated shape of the core (particles agglomeration) of the radial structures obtained at vapour flow rates of 15-20 ccm.

The observed nanotube inter-wall spacing was typical for graphitic nanostructures, 0.34 nm, Fig. 63. The difference between the directly observed

inter-layer spacing of the spherical graphitic shells of the agglomeration (agglomeration of nano-onions) and the MWCNT walls (0.33 nm and 0.34 nm, respectively) was manifest as two proximate peaks in X-ray diffractograms, Fig. 63.

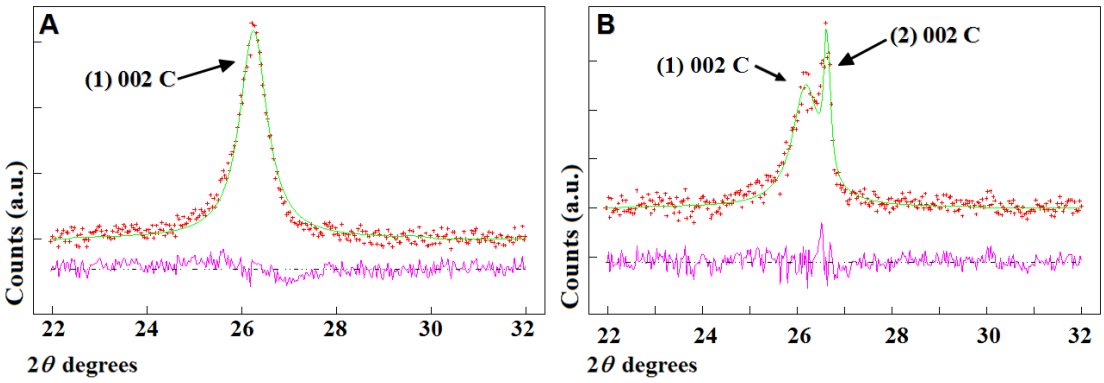

Fig.63: Typical X-ray diffractogram data (red), and Rietveld refinement (green line), of the 002 graphitic carbon reflection obtained from a powder comprising filled nanotube material grown on a smooth quartz surface (A) and from powder comprising radial structures prepared under identical reaction conditions (B). Clearly (B) shows two proximate peaks; the lower angle peak (1) corresponds to the 002 reflection from multiwall carbon nanotube walls observed in (A). This feature corresponds to the 0.34 nm lattice spacing directly observed in selective area diffraction studies of individual filled nanotube (Fig.57), namely the 002 reflection from graphite space group $P6_3/mmc$ (ICSD Chemical Database Ref. 53781). The second graphitic peak (2) corresponds to the lattice spacing of 0.33 nm (002 peak of graphite hexagonal $P6_3/mmc$, ICSD Chemical Database 52230) of the graphitic shell of the spherical particles as observed in the selective area diffraction pattern in Fig.54 (inset). The light-violet line corresponds to the difference between the X-ray diffractogram data (red) and the refinement (green line).

The main encapsulated phases were identified as those commonly observed in the vertical arrays, namely α-Fe, and γ-Fe, and Fe_3C, Fig. 64. Unlike the vertical array structures, the radial structures have a lower abundance of Fe_3C. The Fe_3C content diminishes with increasing vapour flow rates used in the reaction. Furthermore the γ-Fe quantity also diminishes with increasing vapour flow rate. At flow rates of 20 ccm there was essentially no γ-Fe present, Fig.65. This suggests that when the radial structures spend more time in the vapour (at vapour flow rates of 15-20 ccm), more carbon could be migrating from the filling to the MWCNT walls, creating new graphitic layers. This mechanism will be involving also the radial structure core (particles agglomeration). This suggests that, owing to the low thermal mass of the radial structures, the quantity of carbon inside the Fe-based filling will decrease with the increase of time spent by the radial structure in the vapour.The residual γ-Fe (2%) could be then distribuited as a layer around the ending part of some α-Fe single crystals filling the MWCNT or around each core particle forming the agglomeration.

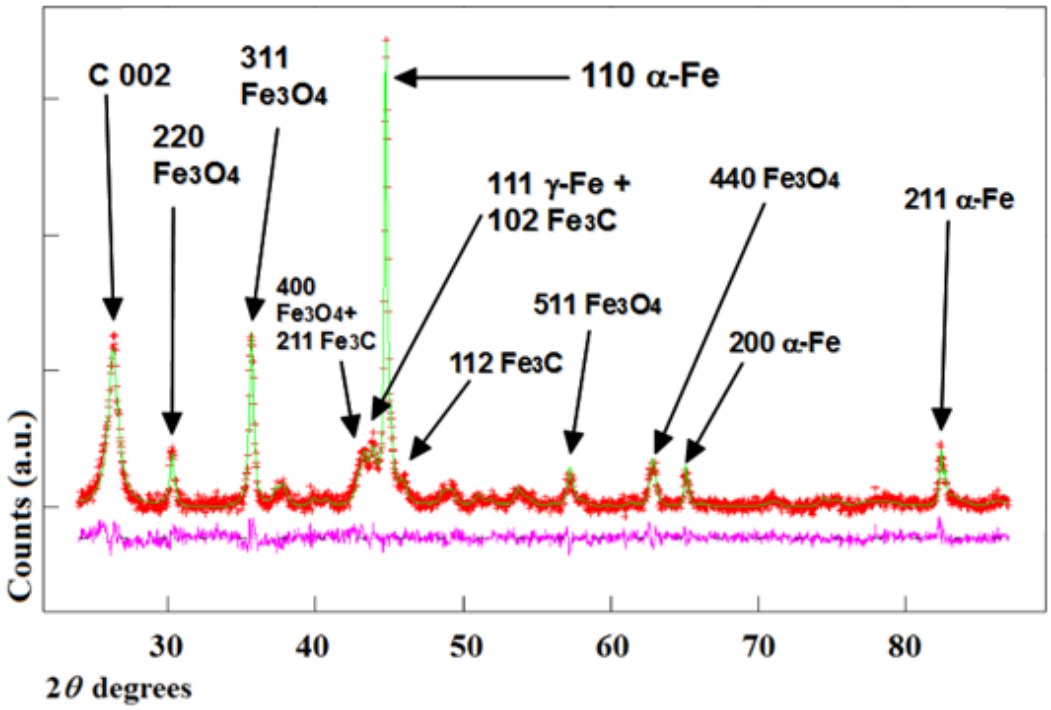

Fig.64: Typical X-ray diffractogram data (red), and Rietveld refinement (green line) for powder of radial structures obtained with an vapour flow rate of 3.5 ccm. The relative weight abundance of the encapsulated phases are 3% cubic γ-Fe (*Fm-3m*, Crystal Open Database Ref. 9008469), and 12% of cubic α-Fe (*Im-3m*, Crystal Open Database Ref. 1100108) and 18 % of orthorhombic Fe_3C (Crystal Open Database Ref. *Pnma* 16593). A 17% weight abundance of Fe_3O_4 (cubic, space group *Fd3-mz,* Ref. 65338 ICSD) results from spontaneous oxidation of non-encapsulated Fe particles when the powder is handled in air. The light-violet line corresponds to the difference between the X-ray diffractogram data (red) and the refinement (green line).

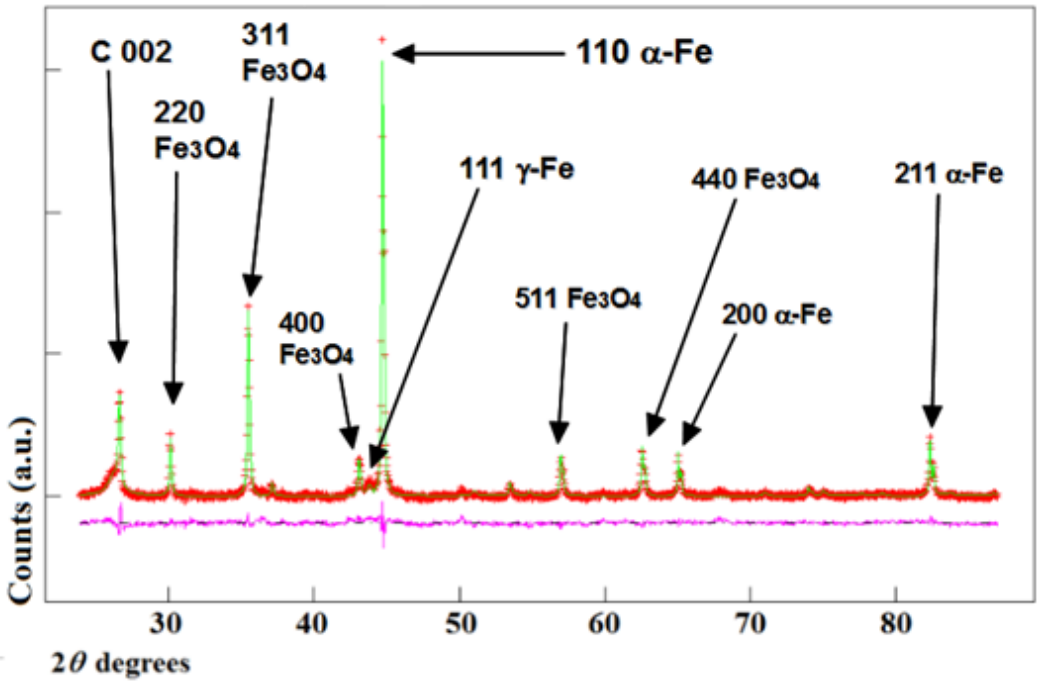

Fig.65: Typical X-ray diffractogram data (red), and Rietveld refinement (green line) for powder comprising radial structures obtained with a vapour flow-rate of 20 ccm. The relative weight abundance of the phases are 2% cubic γ-Fe (*Fm-3m*), and 28% of cubic α-Fe (*Im-3m*). A 26% weight abundance of Fe_3O_4 (cubic, space group *Fd3-mz*) results from spontaneous oxidation of non-encapsulated Fe particles when the powder is handled in air. The light-violet line corresponds to the difference between the X-ray diffractogram data (red) and the refinement (green line).

Following the theory associated to the formation of fluctuating-confined eddies in surfaces with d-type and k-type roughness reported in literature by Perry *et al.* [83] (previously described in Chapter 1), and the theory of the boundary layer flow together with the properties of eddy viscosity reported by J.P. Holman [82] (outlined in Chapter 1), we propose a growth-model in which the formation of the central agglomeration of homogeneously nucleated particles is induced by the

shape of the fluctuating-confined eddies created by the asperities of the rough surface. The development of confined eddies in a rough surface can be described considering the model proposed by Perry *et al.* on the behaviour of a flow in presence of a substrate with d type roughness (Fig.21). Furthermore the schematics previously shown in Fig.20 allowed us to visualize the movement of a turbulent lump in presence of a turbulent flow and to describe the behaviour of the Ar flow in the presence of a rough surface.

Fig.66 shows a schematic diagram of the proposed three-stage radial-structures formation mechanism in fluctuating metal–carbon vapor. The yellow shading implies high iron content, while solid black lines and dark shading represent graphitic carbon and the carbonrichness of a nanoparticle, respectively. The dashed lines represent the volume of vapor within several diffusion lengths (for the metal–carbon species in the vapor) from the active area of formation. In A: (i) the graphite-encapsulated Fe_3C particles spontaneously form by homogeneous nucleation of Fe or Fe-C particles in the viscous boundary layer region of the vapour, (ii) carbon feedstock is driven to particle by the resultant diffusion gradient and dissolves in the particle, (iii) graphitic carbon shells form when the rate of arrival of the carbon feedstock exceeds the rate of dissolution, (iv) the flow of internal carbon is driven to the particle-surface by endothermic formation of the graphitic shells however it ceases when the stable Fe_3C phase is reached.

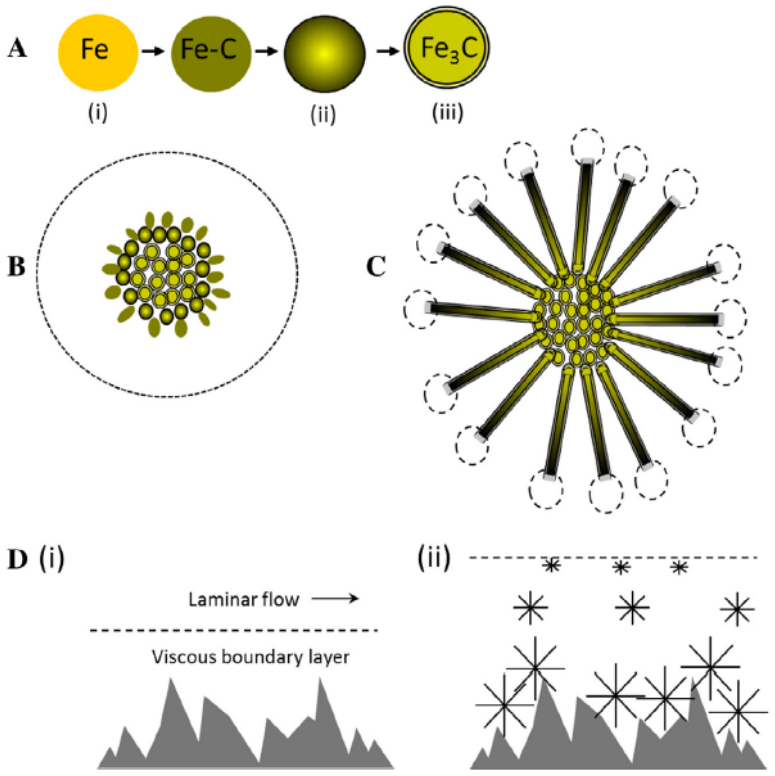

Fig: 66: Schematic of the proposed growth mechanism of the radial structures.

These spherical nanostructures (see B) spontaneously agglomerate following the viscous eddy motion previously described in Fig.49; the central particles are encapsulated (stage A (iii)) whereas the peripheral particles have no graphitic shell (stage A (i)). The spherical diffusion gradient created by the agglomeration results in an asymmetry in the vapor feedstock for the peripheral particles which results in elongation and CNT nucleation. C: The lowest energy stable graphitic MWCNTs structures start to grow. The central-particle-facing face of the elongated peripheral particles is rapidly closed by graphitic shell formation, so the radial growth of the filled nanotubes is driven by the diffusion gradient established at the open tip. D: Self-sustaining reaction conditions can be explained as follows. (i) A rough surface produces randomly fluctuating vapor in the boundary layer between the rough surface and the global laminar flow. (ii) The

diameter uniformity of the central particle and urchin suggests that the homogeneous nucleation and radial-structure growth occurs at the laminar-viscous interface since this is the realm of weak fluctuations and uniform feedstock supply from the global flow. The demarcation between the core (particle-agglomeration) formation and the onset of growth of the radial filled nanotubes appears to be the result of the asymmetry in exposure to the vapour. The rapid formation of the central agglomeration means that the partially formed spherical particles on the exterior of the central agglomeration are exposed to the vapour feedstock flow driven by the diffusion gradient directed toward the central agglomeration. The boundary layer fluctuation amplification mechanism is therefore likely to have two dominant components of feedback:

i) the diffusion gradients created by the consumption of species from the vapour.

ii) the thermal gradients created by endothermic graphitic carbon formation.

The latter is evidenced by the 'switching off' of radial structures growth by contact with an isothermal surface.

Attractive forces on the urchin due to the proximity of the rough surface are greater than the thermophoretic forces so the radial-structure migrates to the rough surface. The period of migration therefore dictates the diameter of the urchin. Once in contact with the surface the formation process will cease because the isothermal surface will equilibrate the temperature gradients at the tips. The roughness of the urchin coating of the surface replicates that of the pristine rough surface, consequently the conditions for nucleation and the laminar-viscous boundary are reproduced. These observations suggest that fluctuations produced

by the interplay of surface roughness and vapour flow determine the conditions for vapour-phase nucleation and subsequent self-organized growth.

In conclusion:

i) In this subchapter we have shown in detail a completely new scaleable chemical vapour synthesis method that yields radial structures comprising MWCNT-continuously filled with α-Fe as dominant and uniform product in the reactor.

ii) We have shown that these structures nucleate and grow in the pyrolized ferrocene vapour, in the viscous boundary layer consisting of randomly fluctuating confined eddies, created by the asperities of a rough surface.

iii) This finding is striking since it clearly shows that the fluctuations have a fundamental role in the achievement of the product due to a self-organizing system. In the system that we described above, the fluctuating eddies and the high density of the pyrolyzed ferrocene vapour induce the homogeneous nucleation and the subsequent agglomeration of the nanoparticles, allowing the formation of the cores of the radial structures.

iv) The homogeneous nucleation process must be connected not only to the degree of supersaturation of the vapour (i.e. the density of the pyrolized ferrocene vapour) but also to the fluctuating eddies.

v) The spherical diffusion gradient created by the agglomeration results in an asymmetry in the vapour feedstock for the peripheral particles which results in elongation (of the particles) and MWCNTs growth. The elongated particles are rapidly closed on the side of the agglomeration by the graphitic shell formation, so the radial growth of the filled MWCNTs must be driven by the diffusion gradient established at the open tip. This tip growth must involve a temperature gradient

exactly at the tip due to the endothermic nanotube formation. This temperature gradient will also drive the carbon flow along the axis of the encapsulated single-crystal toward the tip.

vi) By increasing the vapour flow rates we observe a change in the morphology of the structures from a radial symmetry to an elongated-radial symmetry. This suggests that there is a change in the fluctuation.

vii) We observe also that the relative abundance of Fe_3C and γ-Fe diminishes and become almost zero with the increase of the vapour flow rate.

viii) The fluctuation created by the asperities are comparable to the fluctuations created by a single layer of radial structures. So the reaction is self-sustaining and could be used for industrial purposes.

3.3.2 Locally-perturbed chemical vapour deposition method

In this subchapter we outline in detail another new perturbed vapour flow method of synthesis. In analogy with the radial structures, not previously observed flower-like structures comprising MWCNTs continuously filled with single crystals of α-Fe were observed serendipitously when a small hole in an otherwise flat surface was used to locally perturb the laminar ferrocene/Ar vapour flow. We show that, departing from homogeneously nucleated particles, the MWCNTs nucleate and form in a flower-like arrangement. These particles are produced by the creation of a local perturbation in a vapour with a high density of Fe and C species obtained from the pyrolysis of a laminar ferrocene/Ar vapour flow. Single-phase filling was achieved by a post-synthesis annealing at 500 ºC for 15 hours in Ar flow. The

local perturbation induces the homogeneous nucleation of particles when the pyrolyzed ferrocene vapour reaches particular super-saturation conditions. We demonstrate that these conditions can be reached by using high quantities of ferrocene, high sublimation rates and low vapour flow rates. A schematic diagram of the quartz substrate and the flower-like structures growth region is shown in Fig.67. The flower-like structures morphology was revealed in SEM micrographs of the growth region of substrates extracted from the reactor before the annealing stage. Typical examples are given in Figs.68-71. These structures are found mainly in the regions (10 mm length) immediately after the hole of the substrate (see Figs.67-70). This suggests that the hole can create local perturbed conditions in analogy to the k- type roughness [83] and also that the local perturbed conditions influence the growth of the flower-like structures.

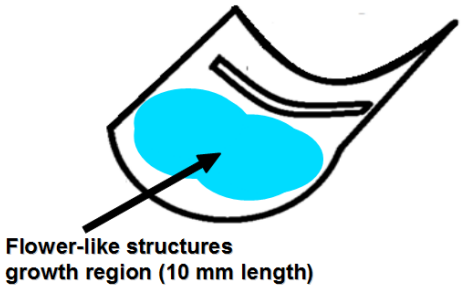

Fig.67: Schematic diagram of the substrate used for the production of flower-like structures indicating the direction of vapour flow, dimensions of the hole, and the growth region.

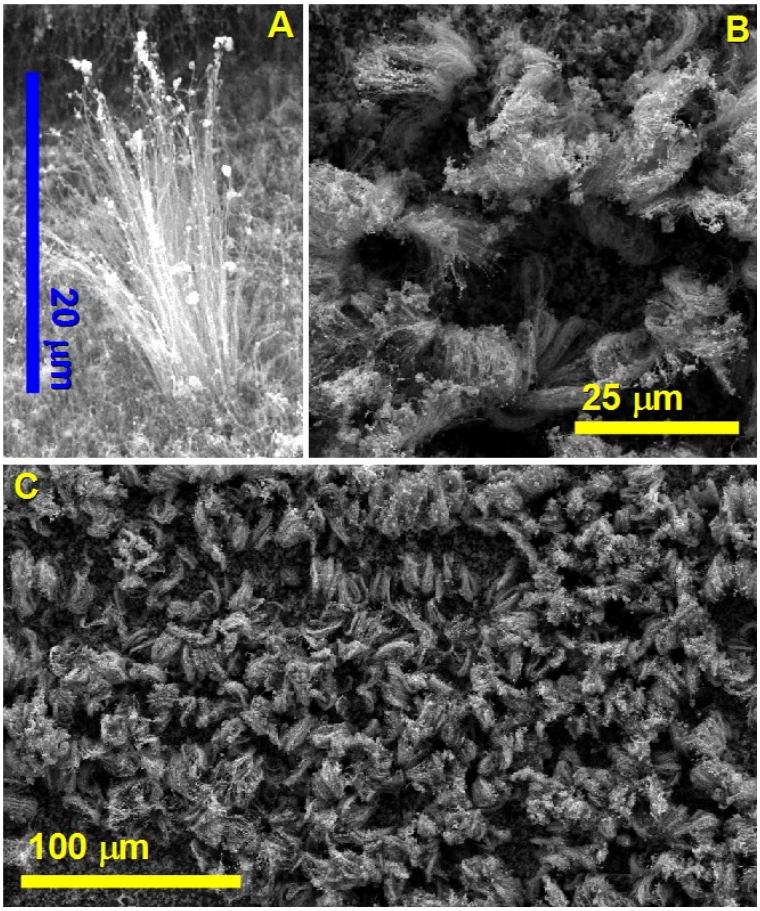

Fig.68: Scanning electron micrographs (taken at 20 kV) of un-annealed flower-like structures in the growth area. A and B show a front-view and top-view (respectively) of individual flower-like structures, C shows a top-view of many flower-like structures.

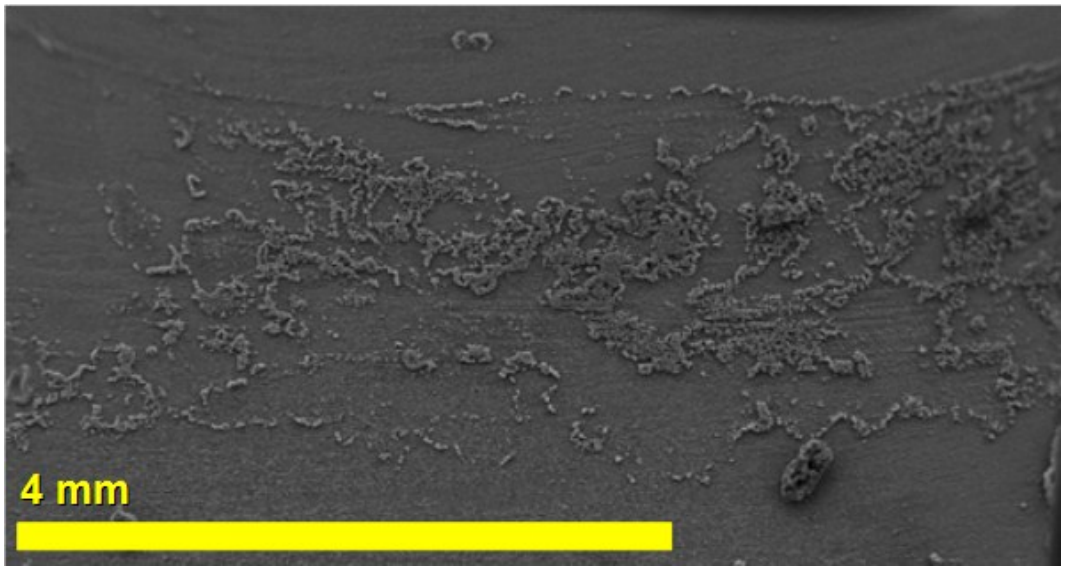

Fig.69: Scanning electron micrograph (taken at 20 kV) of un-annealed flower-like structures in the growth region at low magnification. The length of the growth region is ~ 10 mm.

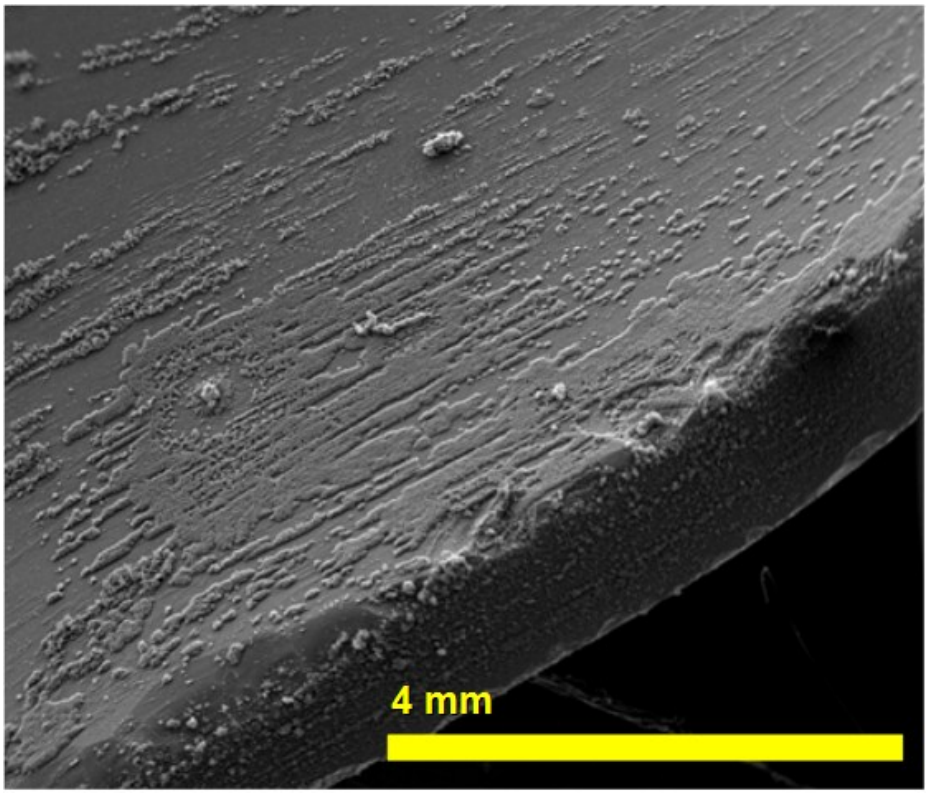

Fig.70: Scanning electron micrograph (taken at 20 kV) of un-annealed flower-like structures showing another part of the growth region at low magnification.

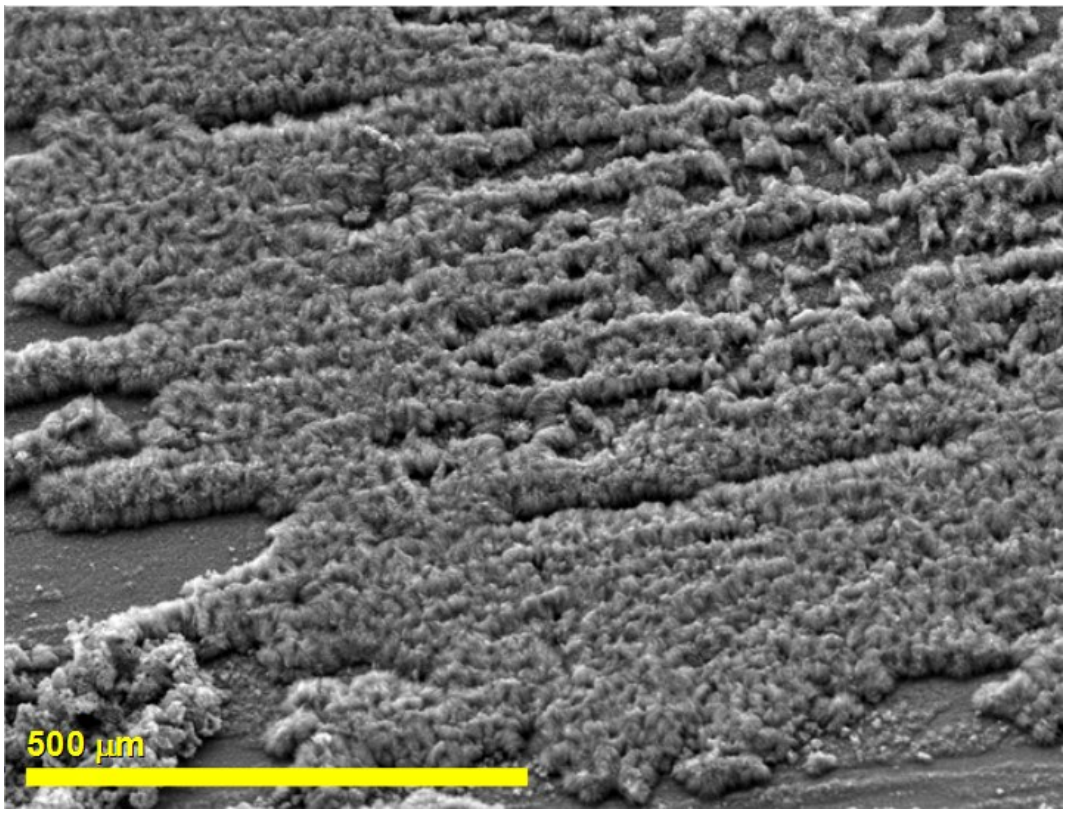

Fig.71: Scanning electron micrograph (taken at 20 kV) of un-annealed flower-like structures in the growth region of the substrate. In some cases the flower-like structures are found with an higher degree of alignment.

The localized perturbation, the high quantity of ferrocene and the very low vapour flow rate are the key process parameters to obtain these structures. The high quantity of ferrocene and the very low flow rate are necessary to create a vapour with high density of Fe and C species. In these conditions the local perturbation induces the homogeneous nucleation of nanoparticles in the vapour (see Fig.72). These nucleating particles are of larger dimensions than those that heterogeneously nucleate on the substrate from the vapour.

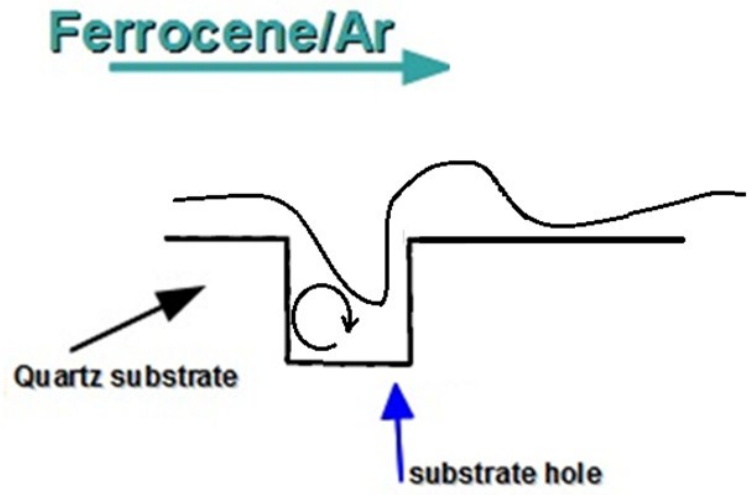

Fig.72: Schematic diagram of the quartz substrate cross-section and ferrocene/Ar vapour flow.

In Fig.73 a schematic of the growth-mechanism of a typical flower-like structure is proposed. The yellow shading implies high iron content; solid black lines and dark shading represent graphitic carbon and the carbonrichness of the particle, respectively. A homogeneously nucleated Fe particle (1) deposits from the vapour to the substrate assuming the shape of a cap (2). The exposure to the C species in the vapour leads to the formation of some islands in the homegenously nucleated particle (1-3). However, owing to its large dimensions, the complete carbon-supersaturation of the particle is not expected. We propose the formation of an not-stable Fe-C based phase as a consequence of the diffusion flux of carbon atoms toward the surface of the particles. Indeed in this process two carbon fluxes must be taken into account: the segregation flux of dissolved carbon atoms towards the particle surface and the diffusion flux of carbon atoms seeking their lowest energy states [35]. Due to the competition between the segregation and diffusion fluxes, two situations can occur in the system depending on the precipitation rate. If the segregation flux is higher than the diffusion flux,

initiation of MWCNT growth can occur. The nucleation of MWCNT is likely to occur from islands where the segregation flux is larger (3-4). If the segregation flux is lower than the diffusion flux, carbon will form the thermodynamically most stable system consisting of metal particles surrounded by graphitic layers. However the latter case is not applicable in our system, since we observe only the formation of MWCNTs. We suggest that after a certain time of exposure to the vapour species (Fe and C) the particle will reach a certain Fe-C concentration and some caps will start to grow from islands of C atoms (See Fig.73) in a mechanism similar to that previously mentioned in the case of SWCNT-nucleation [35, 36, 41]. The nucleation of these caps will lead then to the nanotube growth-stage . The shape of each cap may change during this process leading to open-growth mode of the MWCNT (4). This open-growth mode is confirmed by the fact that the observed MWCNT-filling is continuous for a much longer length scale than that present in MWCNTs grown from heterogeneously nucleated particles. The dashed lines in Fig.73(4) represent the volume of vapor within several diffusion lengths (for the metal–carbon species in the vapor) from the active area of nanotube-formation. We propose two possible open-growth mechanism modes: tip-growth and base-growth. The large dimensions of the homogeneously nucleated particles are beneficial to both of the possible filled-MWCNT open-growth mechanisms: the large cross-section exposed to the vapour ensures high capture and delivery feedstock to the base, and the absence of near neighbors (in contrast with close-packed vertical arrays formation) in the emerging flower-like MWCNTs, which is also a consequence of the large dimensions of the nucleating particle, ensures a well-defined vapour-capture volume at the tips (see Fig.73(4)).

This growth-mechanism is supported by the following observations: i) the flower-like structures are randomly dispersed downstream of the hole (see Fig.68); ii) the MWCNTs spread out from the central point of the flower-like structure (see Fig.68A); iii) the observed minimum-diameter (averaged over 150 flower-like structures) of a single flower-like structure is ~ 5 micrometres so the particle nucleating the structure should possess a diameter larger than 5 micrometres (this is much larger than the typical diameter of 10 nm that an heterogeneously nucleated particle possesses after nucleation. iv) the filling is continuous for a much longer length scale than that present in MWCNTs nucleated and grown from heterogeneously nucleated particles.

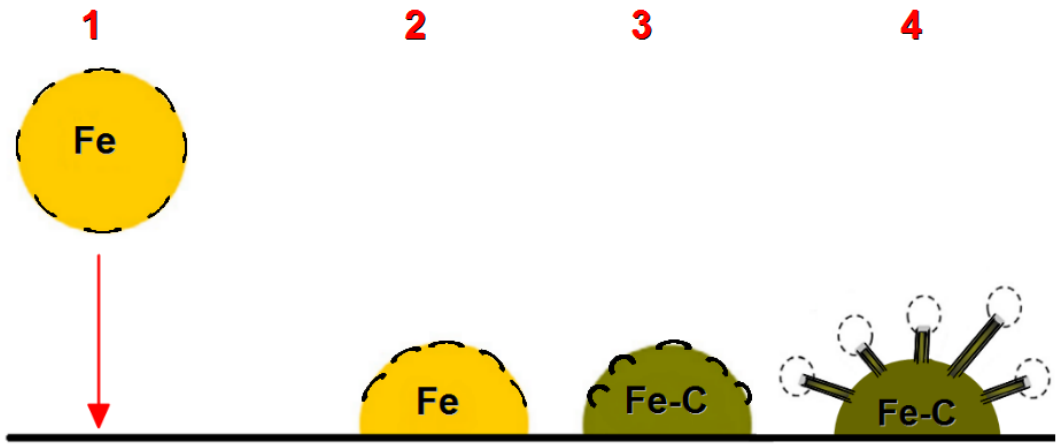

Fig.73: Growth mechanism of the flower-like structures. The black solid lines represent the islands of C atoms formed in a spherical homogeneously nucleated particle (1) that assumes a cap-like shape after contact with the substrate. Carbon caps will start to grow from carbon-islands formed in the homogeneously nucleated particle (stage 2-3) leading to carbon nanotube growth (stage 4).

To increase the yield and obtain flower-like structures as dominant product in a longer area of the substrate, another substrate geometry was also considered. The

new substrate shape is shown in the schematic diagram of Fig.74 and in the scanning electron micrographs of Fig.75. The vapour-flow-facing edges, in the front part of the substrate would favourite the creation of a local perturbation directed toward the curved sides of the substrate. To verify also the growth mechanism explained above, new experiments were performed by using two different sublimations rates of ferrocene. In the first experiment the ferrocene was sublimated with a high sublimation rate (ramp reaching the temperature of 180 °C in ~ 1 min and 30 sec) while in the second case the sublimation rate was lower (ramp reaching 140 °C in 1 min and 45 sec). In both cases a high quantity of ferrocene was used (111 mg), however only in the first case was completely sublimated.The ideal situation to achieve the growth of only flower-like structures would consist in reaching the critical density of the vapour (for homogeneous nucleation) in the shortest time possible. In the first experiment the temperature of 180 °C was reached after 1 min and 30 sec and the reaction time was ~ 2 min (the sample was cooled by using the quench method). Interestingly, as shown in Figs.75-79, the SEM micrographs show the growth of flower-like structures as dominant product along all of the substrate.

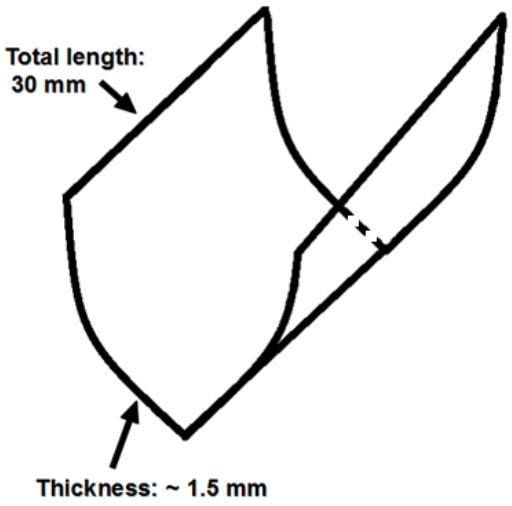

Fig.74: Schematic diagram of the new substrate geometry used for the production of the flower-like structures.

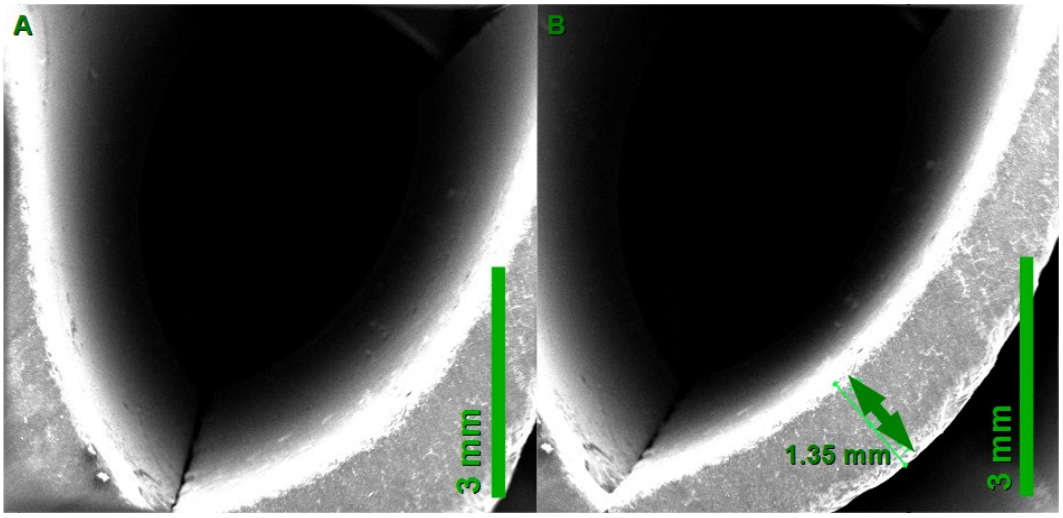

Fig.75: Scanning electron micrograph (taken at 20 kV) showing the new substrate geometry and diameter of the vapour flow-facing edge.

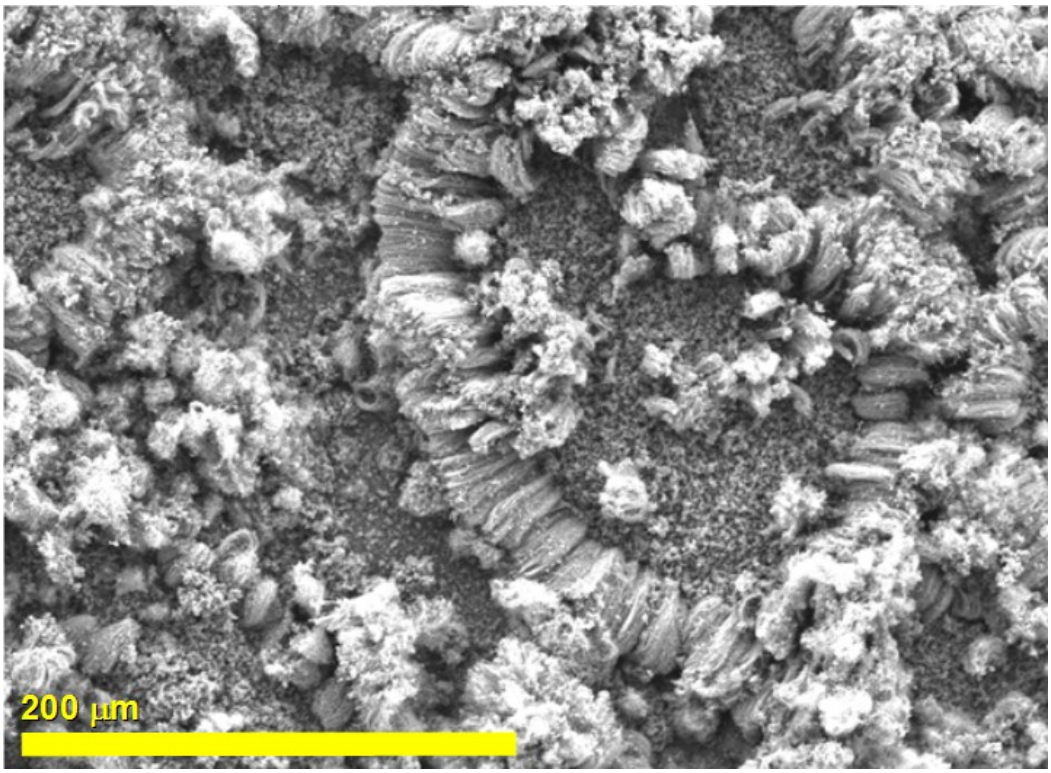

Fig.76: Scanning electron micrograph (taken at 20 kV) of un-annealed flower-like structures in the new substrate.

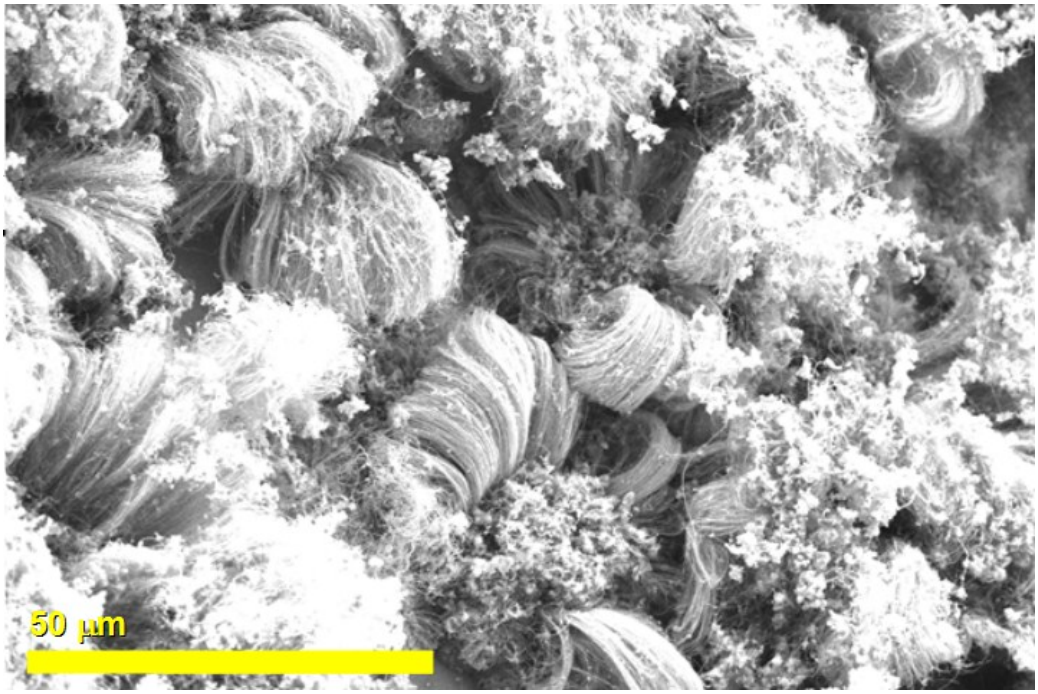

Fig.77: Scanning electron micrograph (taken at 20 kV) showing the homogeneity of the flower-like structures grown in the new substrate.

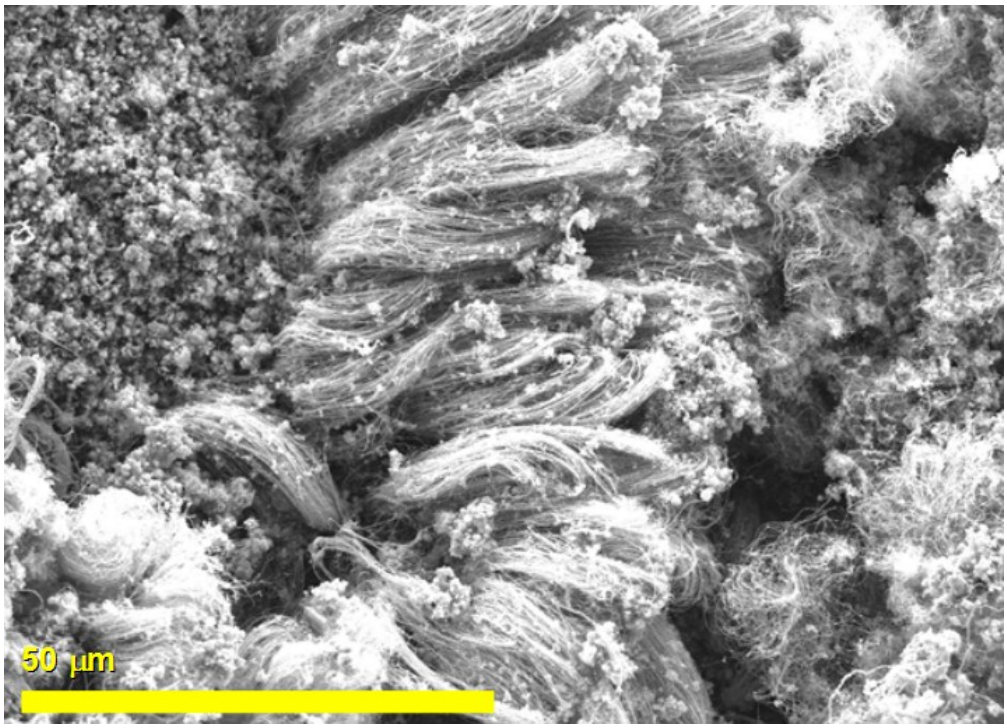

Fig.78: Scanning electron micrograph (taken at 20 kV) showing another region of growth of the flower-like structures grown in the new substrate.

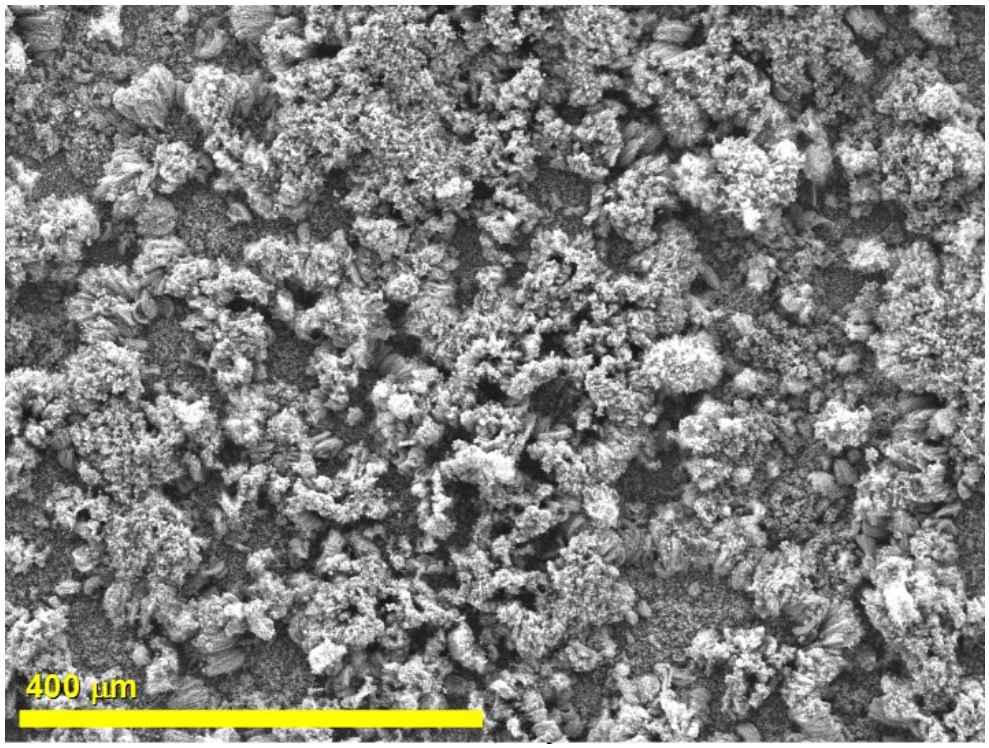

Fig.79: Scanning electron micrograph (taken at 20 kV) showing the high homogeneity of the flower-like structures in a top-view of a larger area.

In the second experiment a lower sublimation rate of ferrocene (~140 °C in 1 min and 45 sec) was used and the sample was quenced (reaction time 1 min and 45 sec). In Figs.80-82 it is possible to notice that in this case the flower-like structures are smaller and grow with variable homogeneity with respect to the case of the faster sublimation. The growth is concentrated in random areas of the substrate where the homogeneosly nucleated particles deposited from the vapour. This observations suggest that, in the case of a slower sublimation of ferrocene, the critical density is reached after a longer time with respect to the previous case and more heterogeneously nucleated particles will be produced. This is confirmed by the smaller length of the flower-like structures (see Figs.81,83,84).

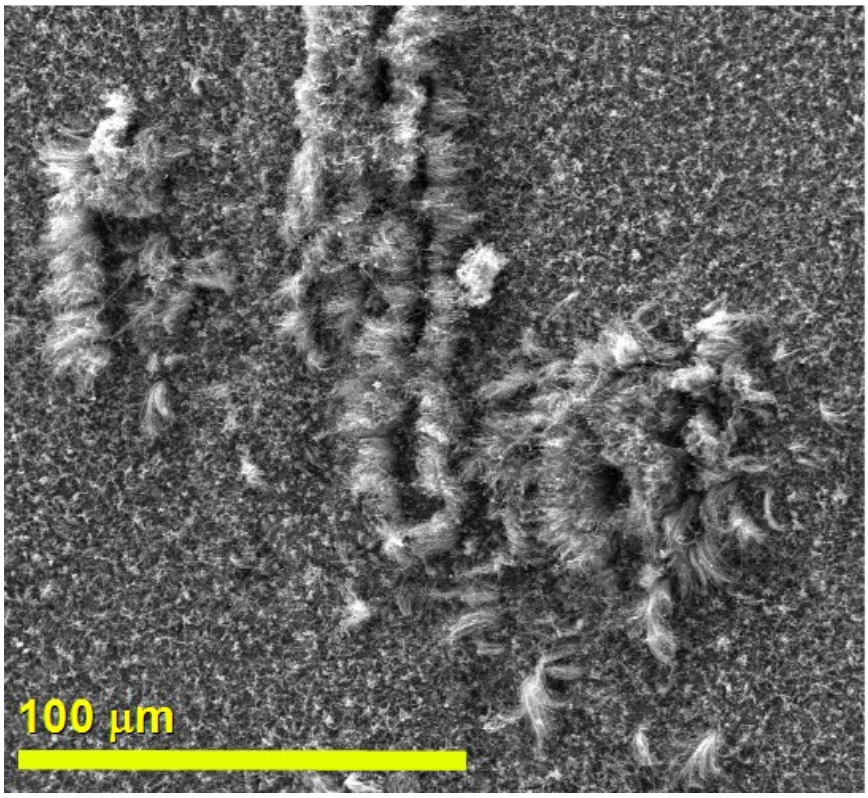

Fig.80: Scanning electron micrograph (taken at 20 kV) showing flower-like structures obtained with lower sublimation rate of ferrocene (~140 °C in 1 min and 45 sec).

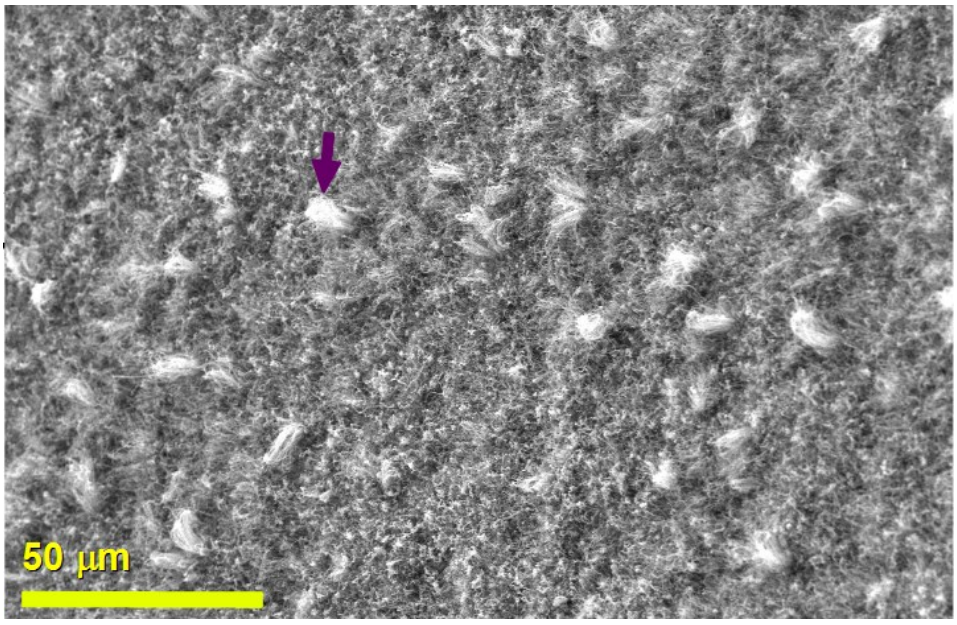

Fig.81: Scanning electron micrograph (taken at 20 kV) showing the variable homogeneity of flower-like structures growth when a lower sublimation rate of ferrocene is used. The violet arrow indicates a single flower like structure.

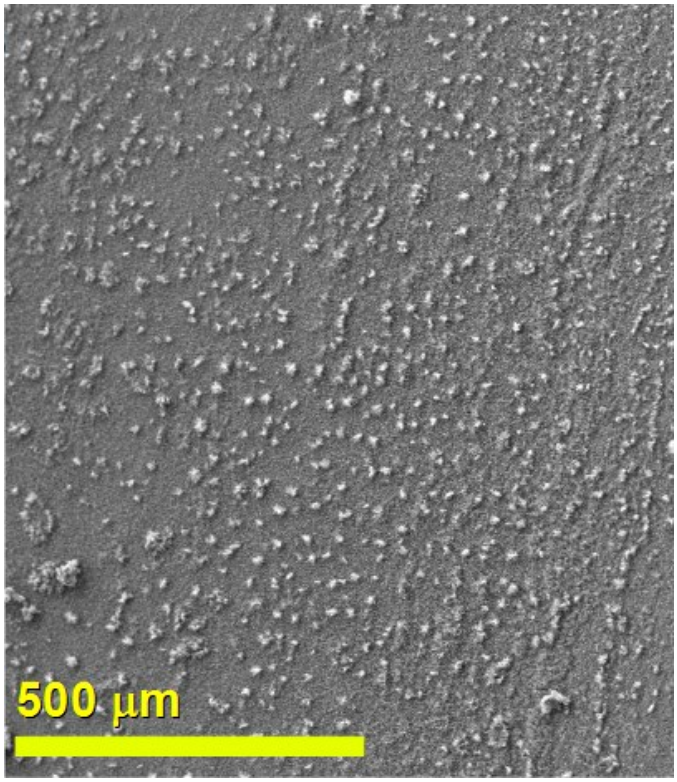

Fig.82: Scanning electron micrograph (taken at 20 kV) showing in a top view the lower homogeneity of flower-like structures growth when a lower sublimation rate of ferrocene is used.

The micrographs in Fig.83 and Fig.84 clearly prove that the growth of the flower-like structures follows the mechanism described above. In the centre of these structures is possible to observe the homogeneously nucleated particles (not completely consumed) from where the MWCNTs nucleated (see Figs.83 and 84). The fact that these particles were not completely consumed, confirms that the critical density for the homogeneous nucleation was reached after a longer time.

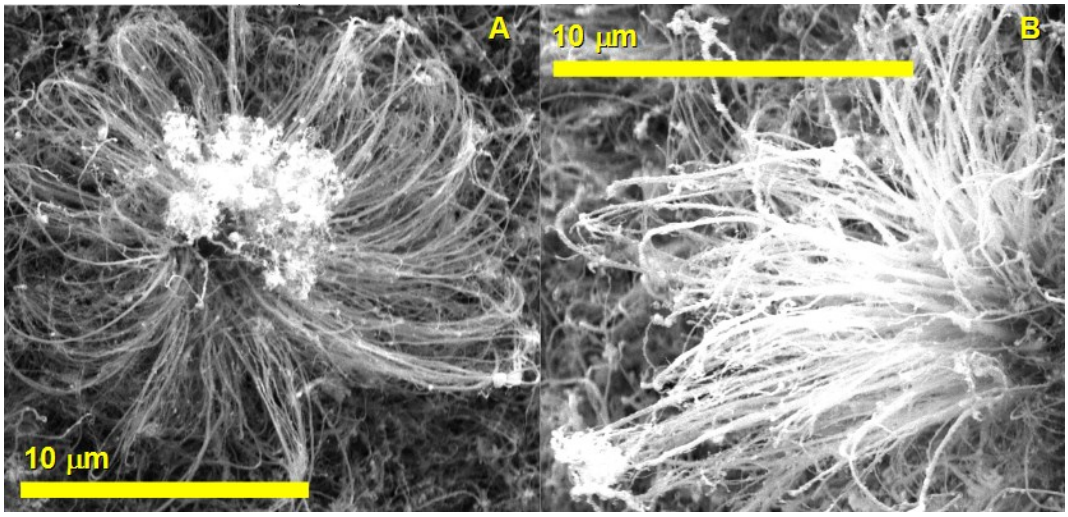

Fig.83: Scanning electron micrographs (taken at 20 kV) showing in A and B the open growth-mechanism of the flower-like structures.

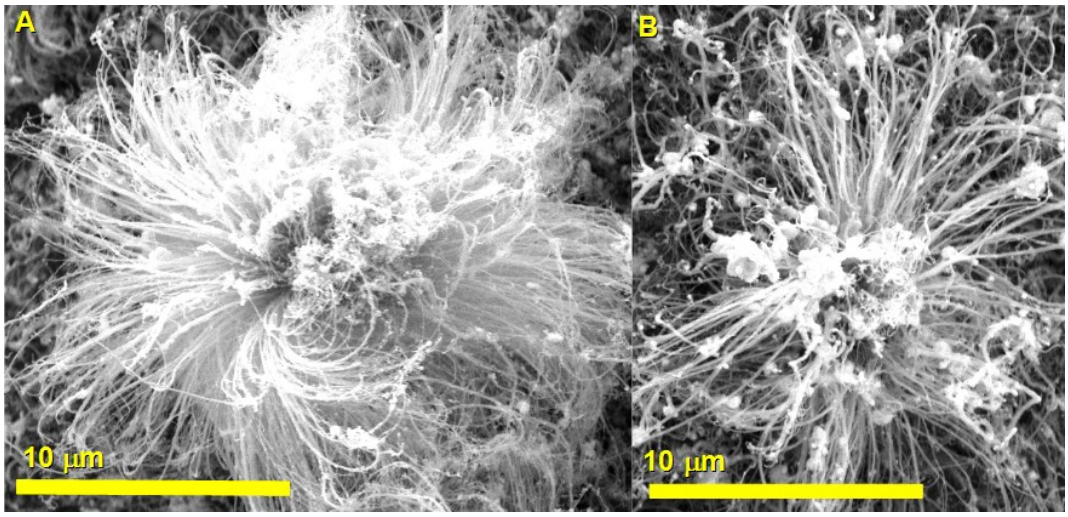

Fig.84: Scanning electron micrographs (taken at 20 kV) showing in A and B two more examples of the open growth-mechanism of the flower-like structures.

The Rietveld refinement of the XRD diffractogram in Fig.85 revealed the relative abundances of the crystalline components of the un-annealed flower-like structures: 59% of carbon (estimated from the 002 diffraction peak of MWCNT graphitic carbon with space group *P6₃/mmc*), 21% of α-Fe (estimated from the 110 and 200 diffraction peaks of α-Fe with space group *Im-3m*), 16% of Fe_3C (estimated from the 102, 211 and 112 diffraction peaks of Fe_3C with space group *Pnma*), and 4% of γ-Fe (estimated from the 111 and 200 diffraction peaks of γ-Fe with space group *Fm3-m*). To maximize the abundance of encapsulated α-Fe, a post-synthesis heat-treatment was considered since (as shown previously in Fig.14 in Chapter 1) bulk γ-Fe decomposes into α-Fe and Fe_3C below 727 ºC, and bulk Fe_3C decomposes into α-Fe and graphitic carbon when is in contact with graphite; the maximum decomposition rate is in the temperature range 500-550 ºC.

Previous reports of post-synthesis annealing of closely packed arrays of MWCNTs filled with single crystals of the above phases showed that annealing for 15-20 hours at 645 – 675 ºC in Ar/H_2 or in Ar resulted in the decomposition of the γ-Fe phase into α-Fe and Fe_3C. Following the previous reports, a first attempt was made to anneal the flower-like structures in Ar for 15 h at 640ºC. However, this attempt resulted in the complete oxidation of the material to α-Fe_2O_3. This oxidation process was also observed in one previous report after annealing at 675 ºC [7], however no explanation of the origin was given. This process could be due to the interaction between hydrogen and the surface of the quartz substrate during the pyrolysis of ferrocene. Previous reports related to hydrogen-quartz interactions showed the possibility of a slow gas-solid reaction leaving a residual dissolved SiO in the quartz [96].

In the attempt to avoid the oxidation of the flower-like structures, new annealings were performed using a lower annealing temperature of 500 ºC. Annealings at 500 ºC in Ar for 13 h and 15 h resulted in the expected decomposition of γ-Fe into Fe_3C and α-Fe, and of Fe_3C into α-Fe and carbon. A single phase of α-Fe encapsulated by the MWCNT was obtained after 15 h of annealing at 500 ºC, also in this case a partial oxidation to α-Fe_2O_3 was observed. The Rietveld refinement of the diffractogram obtained from the flower-like structures annealed for 13 h at 500 ºC is shown in Fig.86. The relative abundances of the crystalline components of the flower-like structures are: 2% of γ-Fe (estimated from the 111 diffraction peak of γ-Fe with space group *Fm3-m*), 71% of carbon (estimated as before), 22% of α-Fe (estimated as before), and 3% of Fe_3C (estimated from the 102 diffraction peak and from the small 211 and 112 diffraction peaks indicated with the blue and the magenta star respectively). The relative abundance of α-Fe_2O_3 (2%) was estimated from the 104 diffraction peak. In order to observe the changes in the relative abundance of α-Fe_2O_3 with respect to α-Fe, Fe_3C, γ-Fe, and C, the diffraction peaks of the ferromagnetic Fe_3O_4 were not considered.

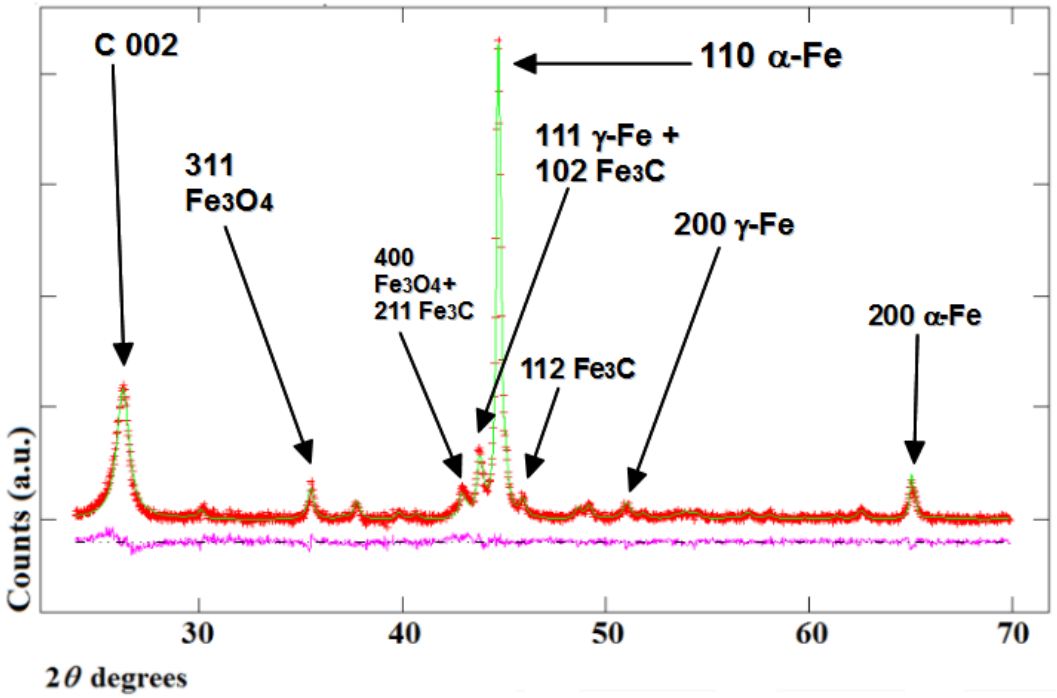

Fig.85: XRD diffractogram obtained from the un-annealed flower-like structures mechanically removed from the growth area in Fig.62C. The Rietveld refinement is indicated by the green line. The light-violet line corresponds to the difference between the X-ray diffractogram data (red) and the refinement (green line).

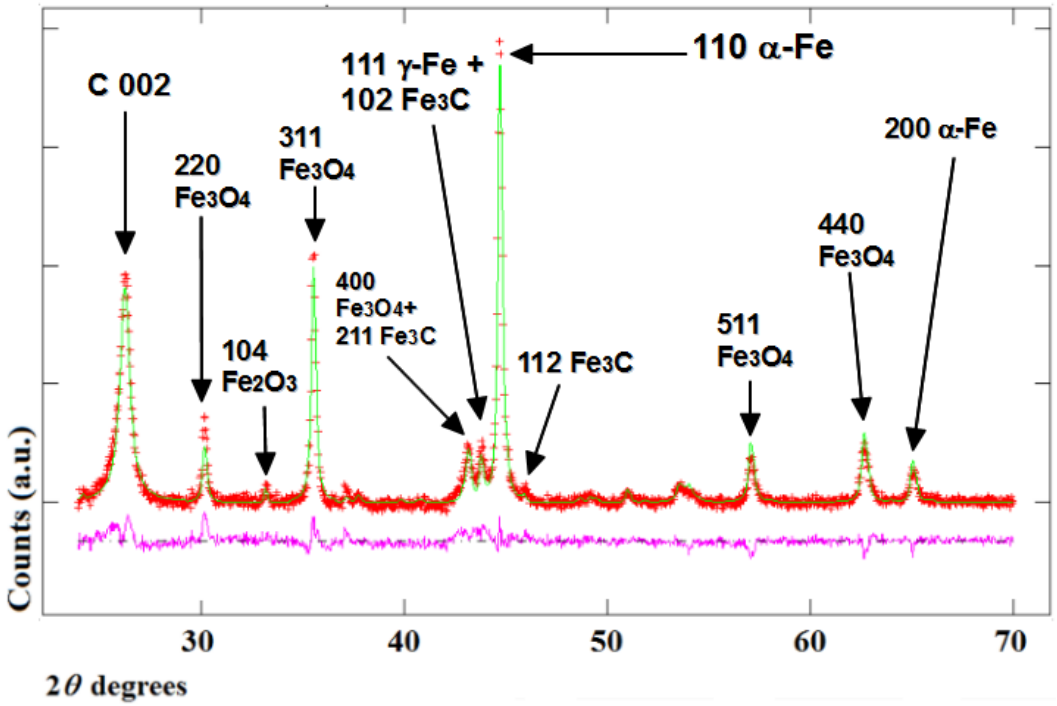

Fig.86: XRD diffractogram of the flower-like structures obtained after annealing for 13 h at 500ºC. The Rietveld refinement is indicated by the green line. The light-violet line corresponds to the difference between the X-ray diffractogram data (red) and the refinement (green line).

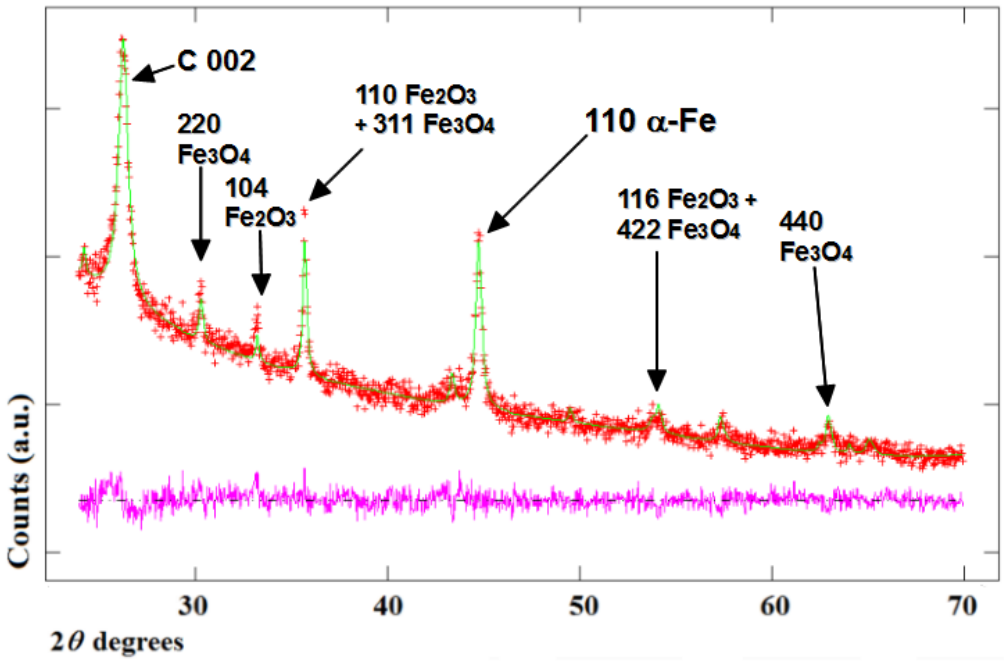

Fig.87: XRD diffractogram of the flower-like structures after annealing for 15 h at 500 ºC. The Rietveld refinement is indicated by the green line. The light-violet line corresponds to the difference between the X-ray diffractogram data (red) and the refinement (green line).

Fig.87 shows the Rietveld refinement of the diffractogram obtained from the flower-like structures annealed for 15 h at 500 ºC. Interestingly, after 15 h of annealing no diffraction peaks from γ-Fe and Fe_3C were observed. The relative abundance of α-Fe (12%) was estimated from the 110 diffraction peak. The relative abundance of carbon (80%) (estimated as before), is slightly higher with respect to what was observed in the diffractogram of the flower-like structures annealed for 13 h (Fig.86) and much higher with respect to what was observed in the diffractogram of the unannealed flower-like structures (Fig.85). The relative abundance of α-Fe_2O_3 (8%) was estimated from the 104, 110 and 116 diffraction peaks indicated with the black stars.

The observation of the α-Fe_2O_3 diffraction peaks (absent in the diffractogram of the un-annealed sample) suggests that the walls of some MWCNTs are damaged during the long annealing process leading to partial oxidation of the MWCNTs filling. This is suggested by the lower intensity of the 110 diffraction peak of α-Fe. The filling of the flower like structures was also investigated by TEM and SEM. Fig.88 shows two SEM micrographs of the flower-like structures removed from the substrate after annealing for 13h. In Fig.88(A) the back scattered electron micrograph shows (in white) the very high filling the MWCNTs. In Fig.88(B) the secondary electron micrograph of the same area is shown. In Fig.89 an example of MWCNTs continuously filled with α-Fe obtained after 15 h of annealing is shown together with a SAED. In the micrograph it is possible to notice the high morphological quality of the very long filling of the MWCNT core. In the SAED, the cyan circles indicate the 002 and 004 diffraction spots of the graphitic MWCNT (space group *$P6_3/mmc$*) corresponding to a lattice spacing of 0.34 nm and 0.17 nm respectively. The yellow circles indicate the 110 diffraction spots of α-Fe corresponding to a lattice spacing of 0.20 nm. The contrast of the MWCNT core in Figs.89-92 appears lighter or darker due to the change of the single crystal orientation relative to the diffraction conditions. More examples of MWCNTs continuously filled with α-Fe single crystals are shown in Figs.90, 91 and 92. The MWCNTs observed in the TEM investigations have an average outer-diameter of 150 nm . The MWCNTs filling shows mainly a diameter of ~ 30 nm and ~ 55 nm. In agreement with the XRD analyses, α-Fe_2O_3 nanoparticles were also observed during the TEM investigations of the MWCNTs obtained after annealing for 15 h at 500 ºC. As shown in Fig.93 the observed α-Fe_2O_3 nanoparticles were found in contact with the walls of some MWCNTs and also attached to the end-

part and the walls of damaged MWCNTs. The α-Fe_2O_3 nanoparticles were also identified through SAED analyses in TEM investigations.

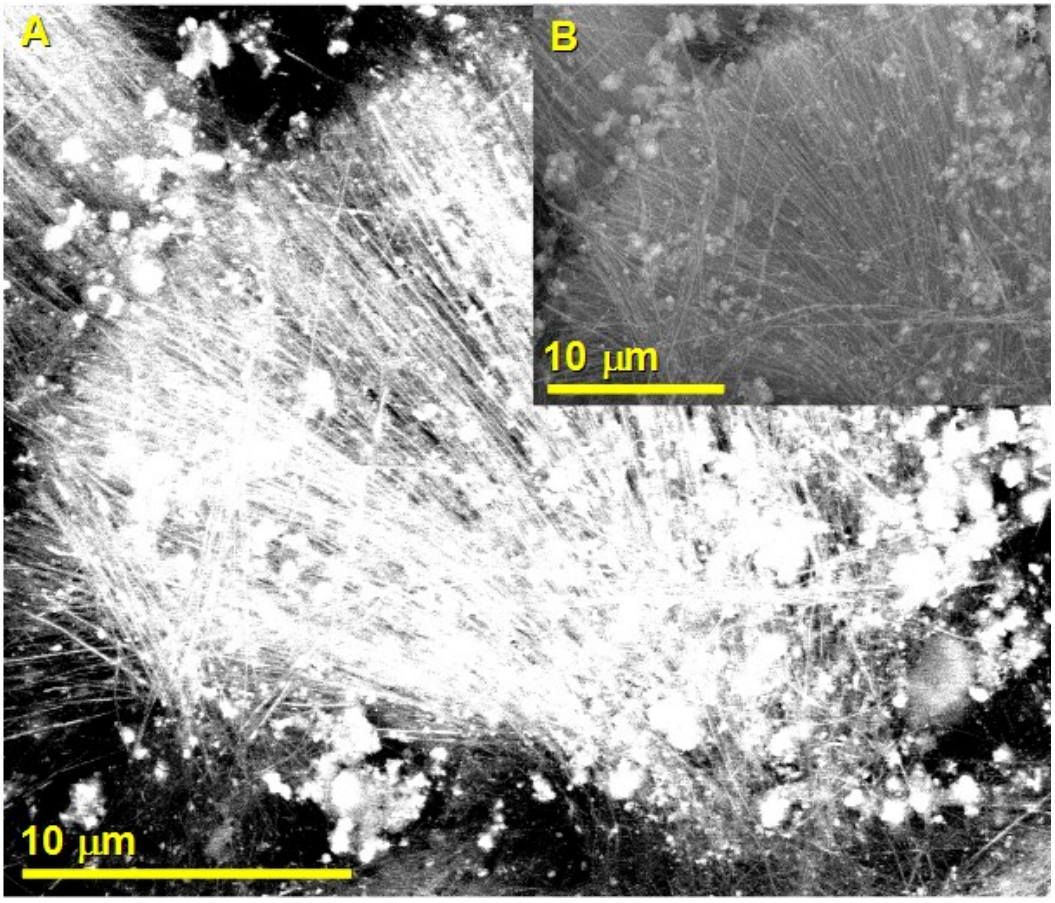

Fig.88: A backscattered electron and a secondary electron micrographs of the flower-like structures removed from the substrate after annealing for 13h. A shows (bright regions) the continuous single crystals filling the MWCNTs. B shows the SE image (taken at 20 kV) of the same area. It is also possible to observe some Fe_3O_4 nanoparticles resulting from oxidation of Fe particles (non-encapsulated inside the nanotubes) when the powder is handled in air.

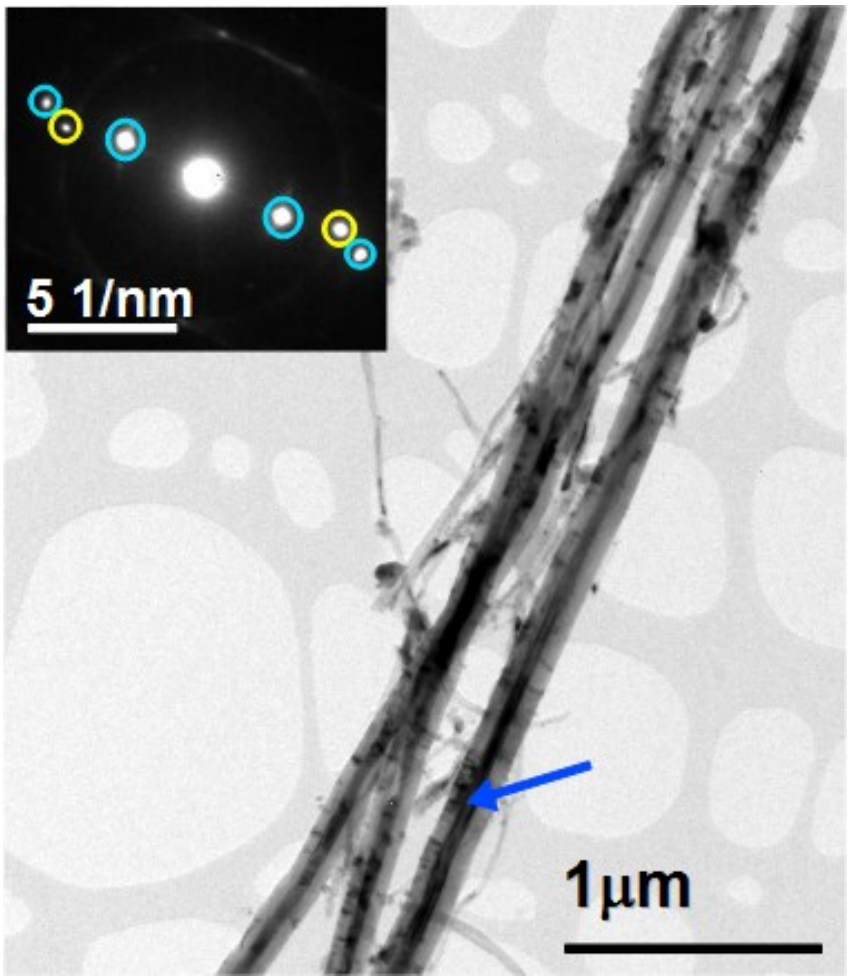

Fig.89: Transmission electron micrograph (taken at 200 kV) showing typical MWCNTs continuously filled with α-Fe (obtained after 15 h of annealing) with the selective area electron diffraction taken from the area indicated by the blue arrow.

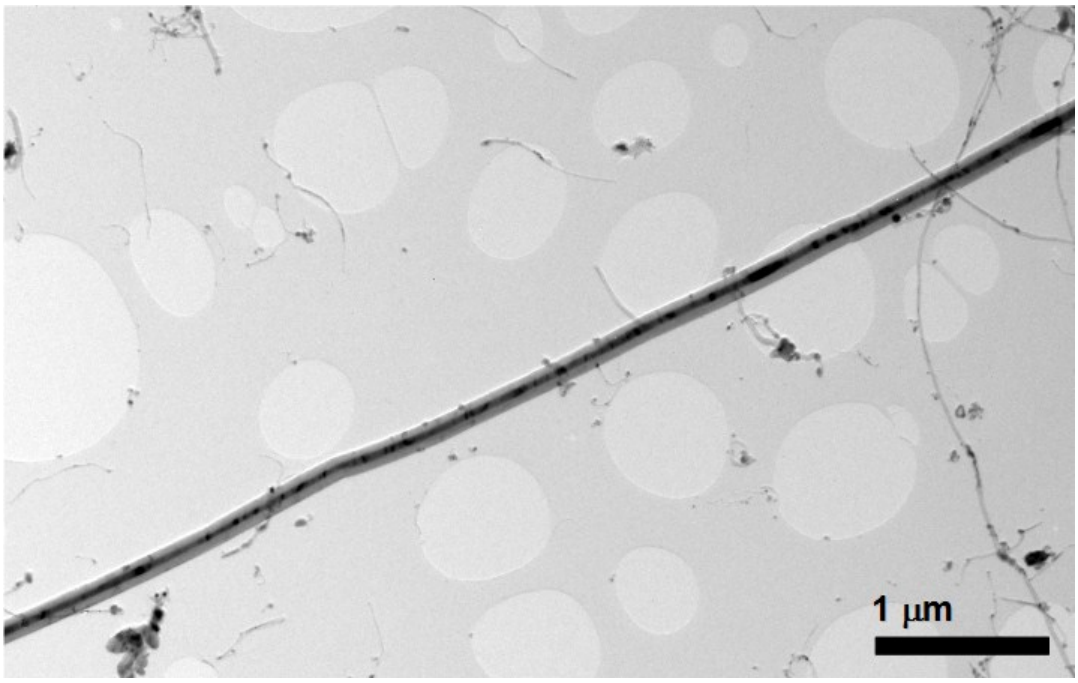

Fig.90: Transmission electron micrographs (taken at 200 kV) showing a region of a MWCNT continuously filled for approximately 19 μm.

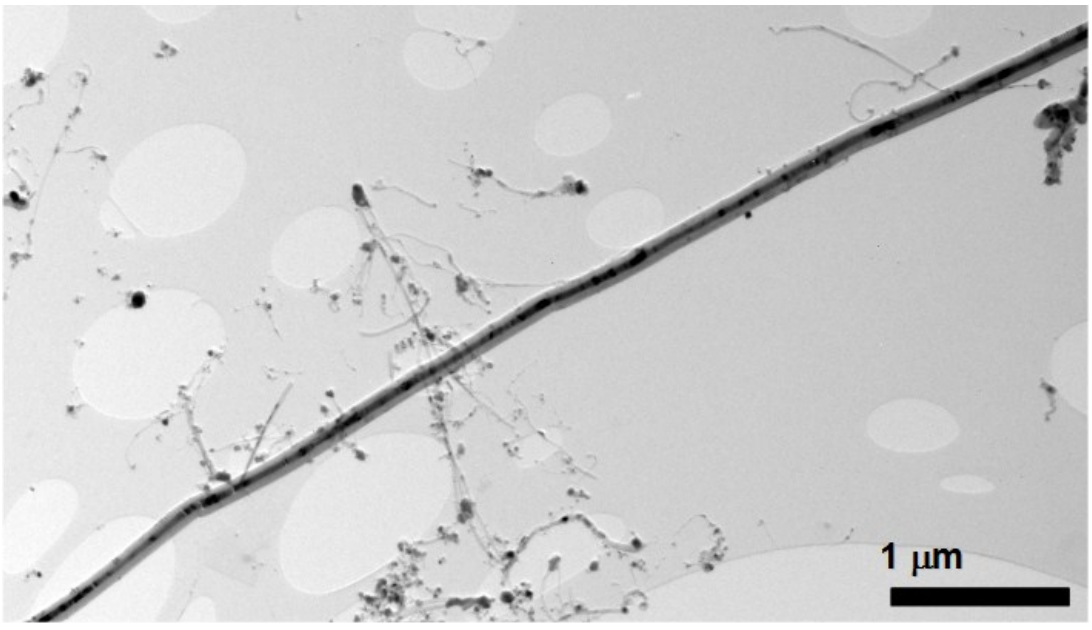

Fig.91: Transmission electron micrographs (taken at 200 kV) showing another region of a MWCNT continuously filled for approximately 19 μm.

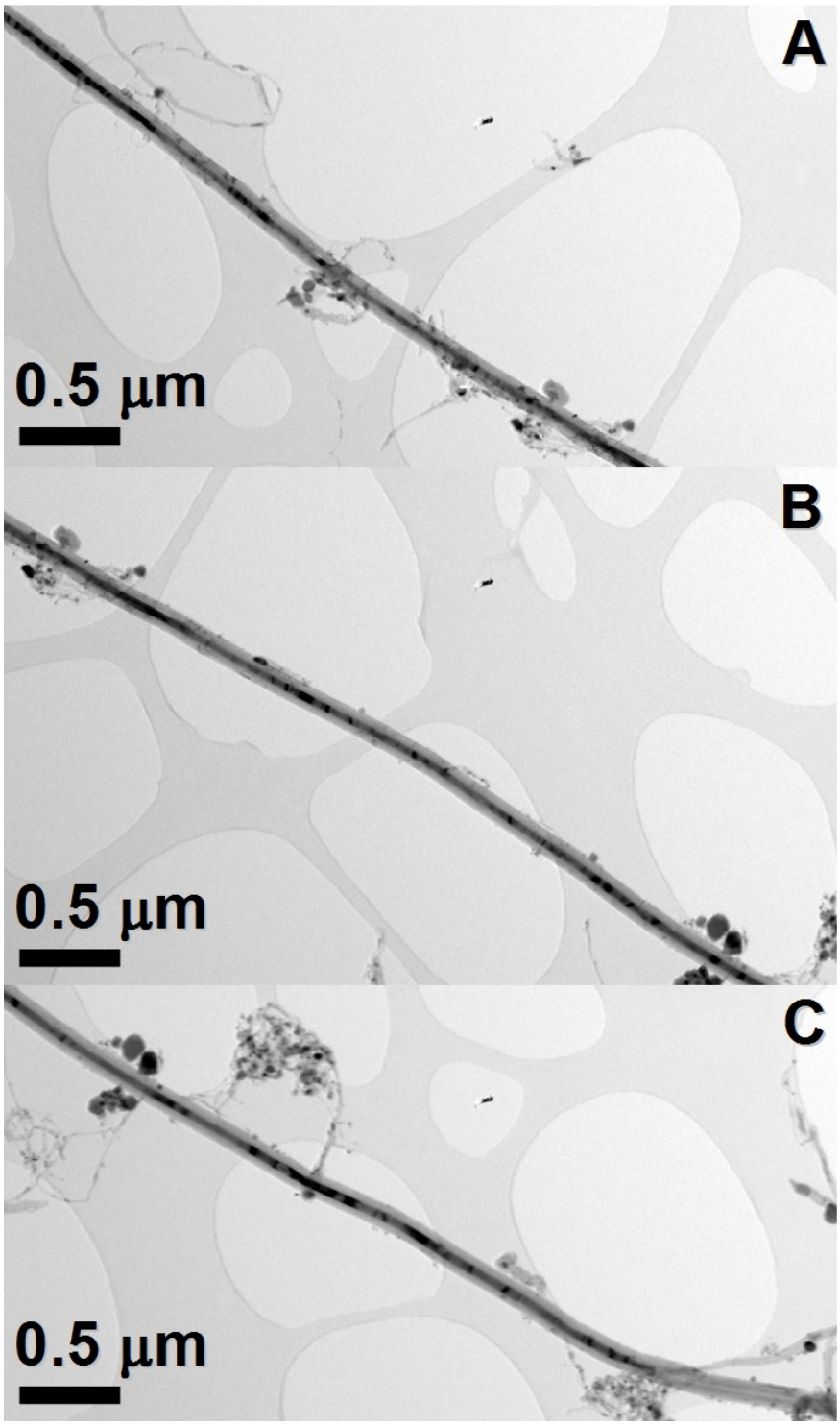

Fig.92: Transmission electron micrographs (taken at 200 kV) showing another MWCNT continuously filled for approximately 13 µm obtained after 15 h of annealing.

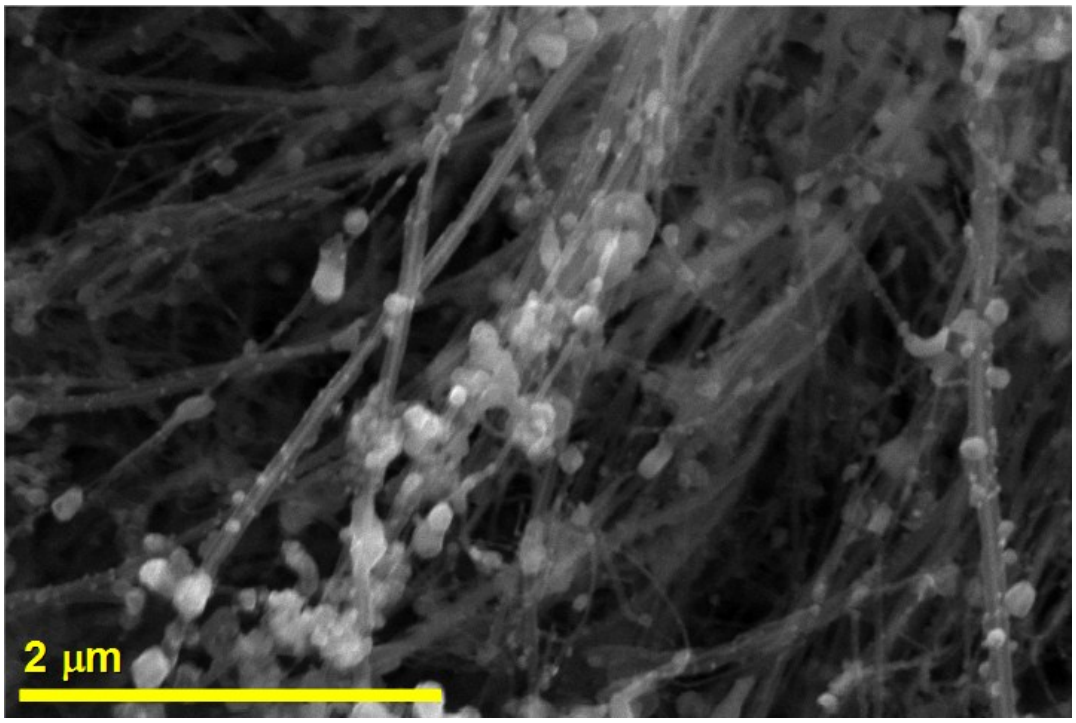

Fig.93: Scanning electron micrograph (taken at 20 kV) showing α-Fe2O3 particles on filled MWCNTs structures owing to the oxidation process after 15 h of annealing at 500 °C.

In conclusion:

i) We have shown a new chemical vapour deposition approach, using a two-stage process consisting of a synthesis in perturbed-vapour conditions, and an annealing at 500 ºC that results in the growth of MWCNTs filled with α-Fe single crystals of up to 19 μm length. These MWCNTs are found in flower-like structures.

ii) The local perturbation induces the homogeneous nucleation of nanoparticles when the pyrolysing ferrocene/Ar vapour flow reaches particular super-saturation conditions. These conditions can be reached by using high quantities of ferrocene, fast sublimation rates and low vapour flow rates.

iii) Once deposited in the substrate, the homogeneously nucleated particles play a fundamental role in the growth of the continuously filled flower-like structures. The large cross-sections of the flower-like structures growing from these particles ensures high capture and delivery feedstock to the base, and the absence of close packing in the emerging MWCNTs ensures a well-defined vapour-capture volume at the tips.

iv) Single-phase filling was achieved by a post-synthesis annealing at 500 ºC for 15 hours in Ar flow. In these conditions only partial sample oxidation of the MWCNTs was observed. Instead, annealing at 640 ºC resulted in complete oxidation of the flower-like structures into α-Fe_2O_3.

3.4 Magnetic properties

3.4.1 Samples prepared by boundary-layer chemical vapour synthesis method

In this subchapter the magnetic properties of the radial structures obtained at 3.5 ccm and 20 ccm will be shown.

The field dependence of dc magnetization of as-produced powder of radial structures exhibited ferromagnetic hysteresis (see Fig.94); at 5 K the saturation magnetization, M_s, showed a dependence on the vapour flow rate, with M_s(3.5 ccm) = 31 emu/g and M_s(20 ccm) = 13 emu/g, whereas the coercivity is almost constant: H_c(3.5 ccm)= 790 Oe, and H_c(20 ccm)= 843 Oe, Fig.94.

The relative weight abundance of the components found in the as-produced powder was extracted from the Rietveld analysis of the X-ray diffractograms, Figs.64 and 65. The sum of the α-Fe and γ-Fe contributions to the saturation magnetisation was then estimated by subtracting the weighted average of the saturation magnetization of bulk α-Fe (M_s~220 emu/g; Curie temperature, T_c= 1043 K), Fe_3C (M_s~169 emu/g, T_c= 483 K) [12], Fe_3O_4 (M_s= ~82-100 emu/g, T_c= 850 K) [97], and the diamagnetic behaviour of graphitic carbon (M=−0.7 emu/g at 50 kOe) [70]. This quantity was found to be always negative thus indicating an exchange-coupled ferromagnetic system despite only a small fraction of γ-Fe (the antiferromagnetic component): this conclusion agrees with that of Karmakar *et al.* for Fe-filled carbon nanotubes [12].

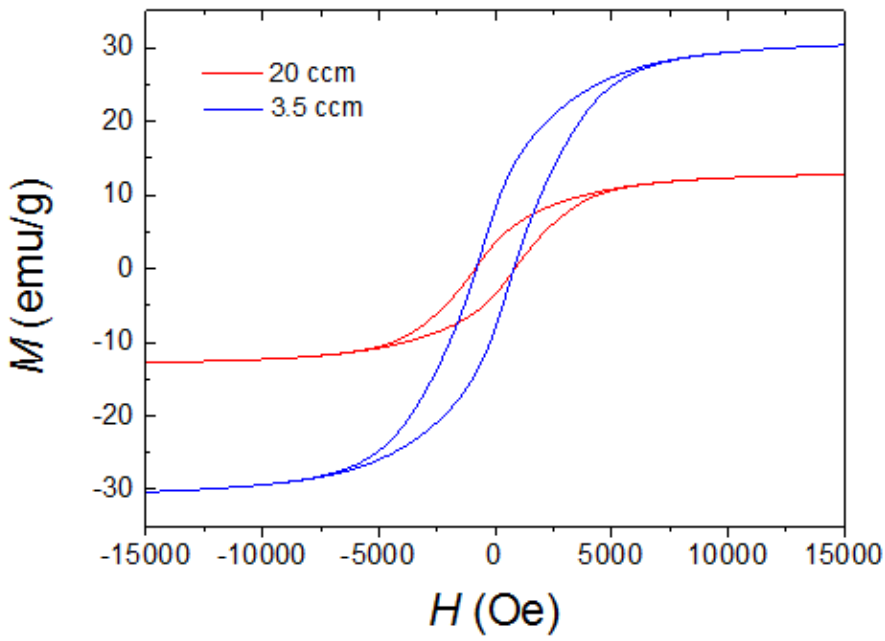

Fig.94: The field dependence of dc magnetization at T=5 K of as-produced powder of radial structures for two values of the laminar vapour flow rate. The relative weight abundance for the powder produced with a flow rate of 3.5 ccm was 3% γ-Fe, 12% α-Fe, 18% Fe_3C, 17% Fe_3O_4, and 50% C (see Fig.64). The relative weight abundance for the powder produced with a flow rate of 20 ccm was 2% γ-Fe, 28% α-Fe, 26% Fe_3O_4, and 44% C (see Fig.65).

The presence of antiferromagnetic γ-Fe in these systems is also suggested by the temperature dependence of field-cooled dc magnetization under the applied magnetic fields of 10 kOe, 1kOe and 0.1 kOe (Figs.95-97). In particular the transition of the γ-Fe phase is visible in Fig.96 and Fig.97 where a change is observed in proximity of 125 K.

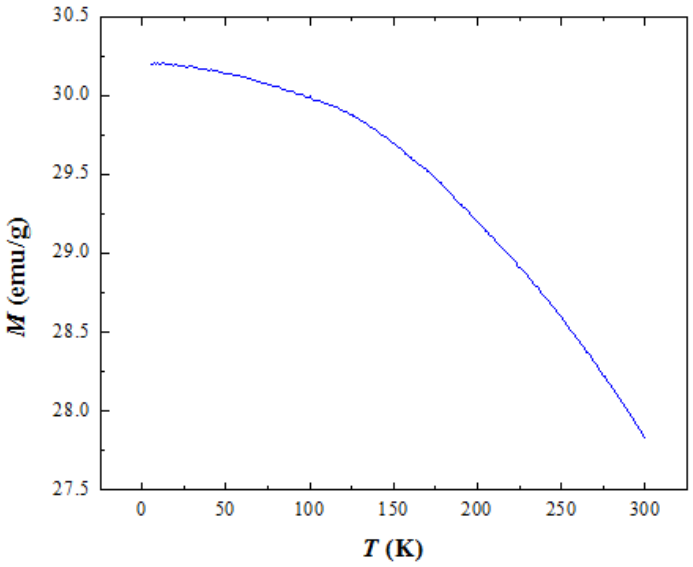

Fig.95: Temperature dependence of field-cooled dc magnetization under the applied magnetic field of 10 kOe (powder produced with a flow rate of 3.5 ccm).

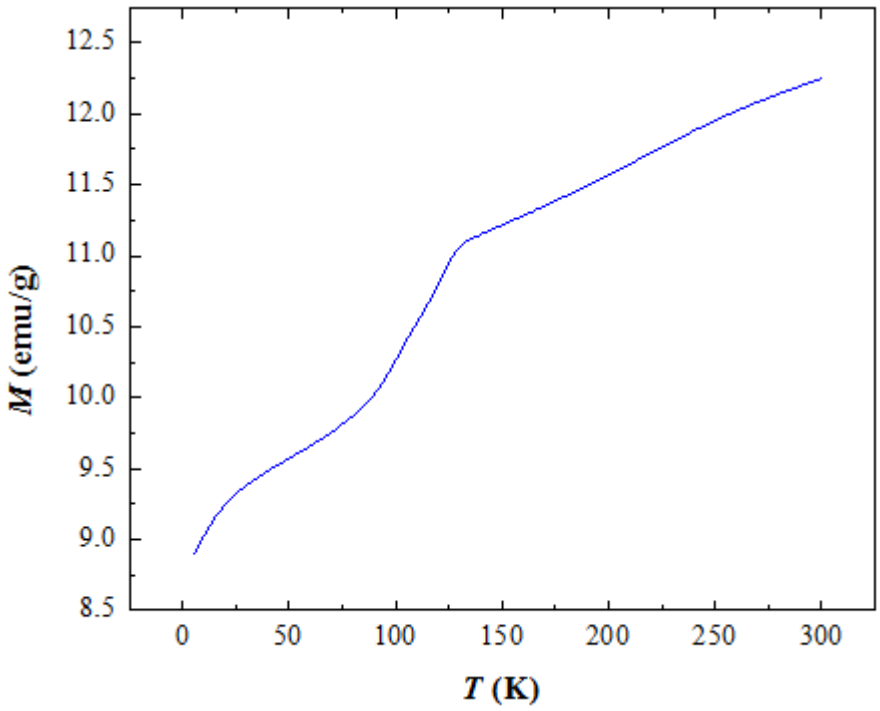

Fig.96: Temperature dependence of field-cooled dc magnetization under the applied magnetic field of 1 kOe (powder produced with a flow rate of 3.5 ccm).

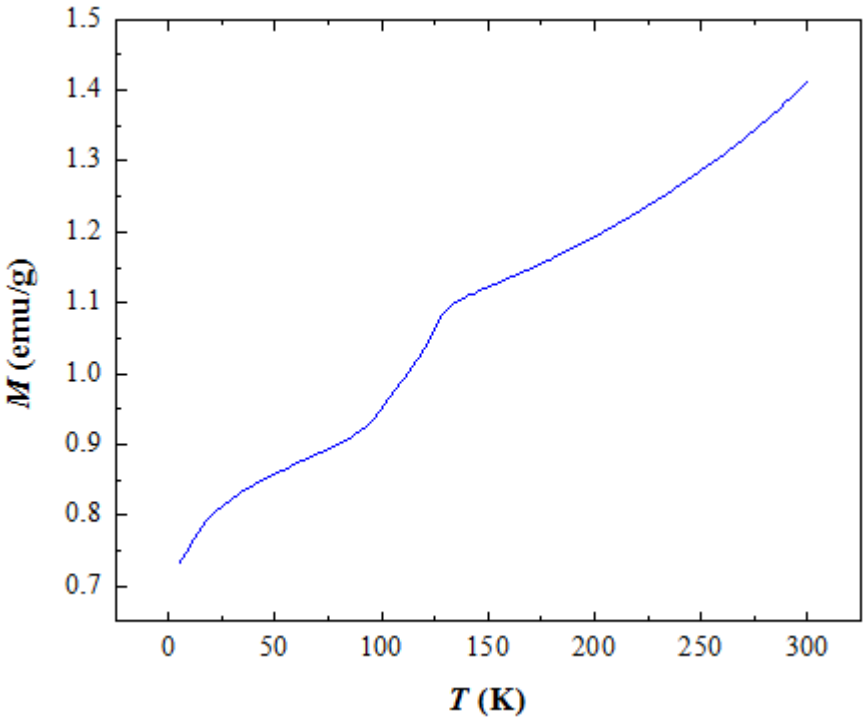

Fig.97: Temperature dependence of field-cooled dc magnetization under the applied magnetic field of 0.1 kOe (powder produced with a flow rate of 3.5 ccm).

The measured values of coercivities are much higher with respect to the coercivities of polycrystalline Fe (1 Oe) and nanocrystalline Fe (23 Oe) [12], slightly lower but comparable to what was measured by Prados *et al.* (1100 Oe) in Fe-filled MWCNTs [13], higher with respect to what was measured by Karmakar *et al.* (660 Oe) in Fe-filled MWCNTs [12] but much lower with respect to what was measured by Aaron Morelos-Gomez *et al*.(~2200 Oe) [9] and Ruitao Lv *et al.* (2000 Oe) [69] (in Fe-filled MWCNTs). In the latter two cases, the MWCNTs were filled discontinuously with very small particles (~10 nm diameter and ~ 300 nm length) of Fe_3C distributed along the MWCNTs core.

The high values of coercivity that we have measured for the radial structures obtained at 3.5 ccm and 20 ccm are likely to be due to the small diameter (MWCNT-filling diameter ~ 30-40 nm) of the α-Fe single crystals filling.

However a contribution of the exchange coupled system can not be excluded. Differently with respect to Prados *et al.*, in our system we don't observe hysteresis shift.

In conclusion:

i) The powder containing the radial structures exibith high coercivities of 790 Oe (3.5 ccm) and 843 Oe (20 ccm).

ii) The as-produced powder is an exchange-coupled ferromagnetic system despite only a very small fraction of antiferromagnetic γ–Fe is present in the radial structures.

iii) The saturation magnetizations appear to be strongly influenced by the exchange coupling.

3.4.2 Samples prepared by locally-perturbed chemical vapour deposition method

In this subchapter the magnetic properties of the flower-like structures are shown. Considering that the quality of the α-Fe single-crystals decreases after 15 h of annealing owing to the oxidation process previously described, the magnetic measurements were performed on the sample annealed for 13 h where only 2% of α-Fe_2O_3 was present. Magnetic measurements were also performed to compare the magnetic properties of the flower-like structures with the magnetic properties of the discontinuously-filled MWCNTs previously produced with steady-state CVD methods reported in literature (with emu/g units) [6,8,9,12,13,69]. Fig.98 shows the hysteresis loop (measured at 5 K) of the powder containing the flower-like structures (obtained after annealing for 13 h). The saturation magnetization corresponds to 72 emu/g, while the coercivity corresponds to 580 Oe.

As reported by Karmakar *et al.* and Likodimos *et al.* [12,70] pure MWCNTs have a diamagnetic behaviour with magnetization of -0.7 emu/g at 50 kOe field. Subtracting the diamagnetic contribution of MWCNTs, it is possible to obtain the corrected saturation-magnetization value of the ferromagnetic single crystals (α-Fe and Fe_3C) [12]. In this case, it is also necessary to consider the relative abundance associated to the diffraction peaks of the ferromagnetic Fe_3O_4 in the Rietveld refinement shown in Fig.86.

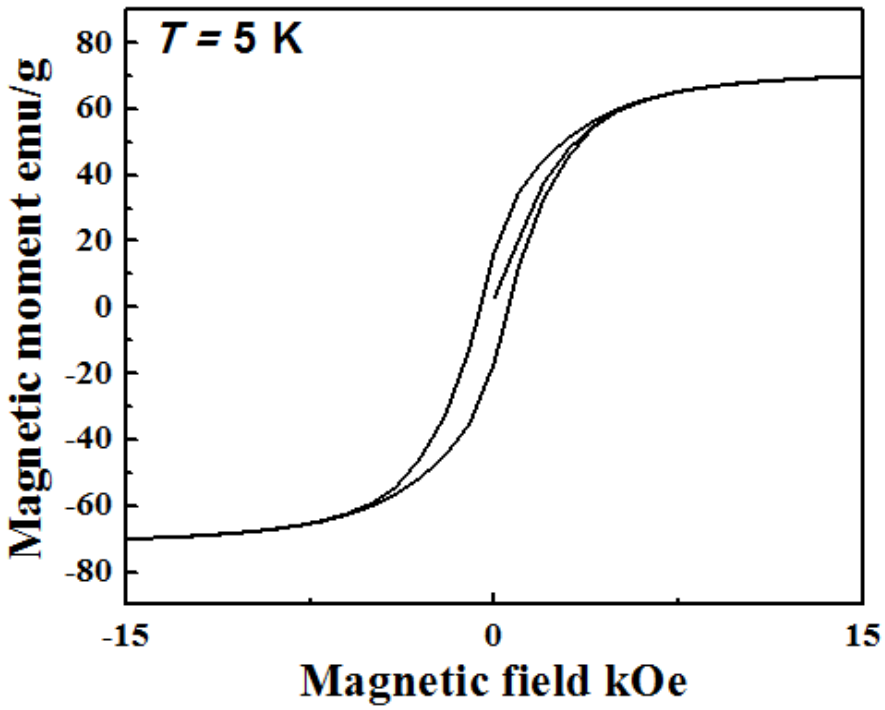

Fig.98: Hysteresis loop at 5 K of the powder containing the flower-like structures annealed for 13 h (X-ray diffractogram previously shown in Fig.86). In this case also the diffraction peaks of the ferromagnetic Fe_3O_4 nanoparticles were included in the quantitative analysis.

The relative abundances of the phases present in the overall sample correspond to 19% of α-Fe, 2% of γ-Fe, 3% of Fe_3C, 59% of C (MWCNT walls), 16% of Fe_3O_4 and 1% of α-Fe_2O_3. As written above the saturation magnetization for bulk α-Fe, bulk Fe_3C and bulk Fe_3O_4 are ~ 220 emu/g, ~ 169 emu/g and ~ 82-100 emu/g respectively [12,97], while γ-Fe and α-Fe_2O_3 are antiferromagnetic at temperatures lower than ~ 100 K [12,13,98]. Referring the saturation magnetization of 72 emu/g only to the ferromagnetic fraction of the sample (38%), it is possible to obtain a corrected saturation magnetization of 189.5 emu/g [12]. This calculation excludes the diamagnetic contribution of the MWCNT

walls (59%) and ignores for simplicity the antiferromagnetic contribution of α-Fe_2O_3 (1%) and γ-Fe (2%) [12]. The corrected saturation magnetization is comparable to the saturation magnetization of bulk α-Fe of 220 emu/g [12]. Whereas if we don't exclude the α-Fe_2O_3 and γ-Fe contributions, the corrected saturation magnetization will result in 175.5 emu/g. In particular this value of saturation magnetization suggests that the γ-Fe phase is likely to have a different space distribution inside the MWCNTs with respect to the radial-structures case described above. This value of saturation magnetization is much higher with respect to those observed in the case of the radial structures and higher with respect to those reported in previous literature works [6,8,9,12,13,69].

The coercivity of the powder containing the flower-like structures is comparable with the coercivity observed by Karmakar *et al*. [12] in un-annealed MWCNT (660 Oe) and much higher with respect to the coercivity of annealed MWCNT observed by Xuchun Gui *et al.* [8] (290 Oe). The measured coercivity of 580 Oe is however slightly lower with respect to that measured in the un-annealed MWCNT by F.C. Dillon *et al.* [6] (850 Oe) and much lower with respect to that measured by Ruitao Lv *et al.* in the (un-annealed) ferromagnetic buckypaper [69] (2000 Oe) and by Aaron Morelos-Gomez *et al.* [9] (~2200 Oe). This appears to be due to the smaller diameter and much higher quantity of Fe_3C single crystals. In those cases the higher magnetocrystalline anisotropy contribution could also play an important role in the magnetization measurements [6,9,69]. Here, the flower-like structures annealed for 13h have only 3% of Fe_3C so the magnetocrystalline anisotropy plays a much lesser role. The lower value of coercivity can also be due to the lower alignment of the flower-like structures after the post-synthesis annealing treatment of 13h.

In conclusion:

i) The powder containing the flower-like structures show a very high saturation magnetization of 189.5 emu/g comparable with the saturation magnetization of bulk α-Fe, and also a high coercivity of 580 Oe.

3.4.3 Magnetic domain description

In this subchapter the approximated critical diameter size with which a single crystal of α-Fe can be considered a single magnetic domain will be compared to the diameter of the observed α-Fe single crystals that continuously fill the MWCNTs obtained with the new synthesis methods described in the previous subchapters.

Despite the high aspect ratio, previous literature studies of the magnetic arrangement in the Fe_3C and α-Fe fillings (with diameter ~10-40 nm) reported that these single crystals are found in a single magnetic domain arrangement [66,67]. Fe_3C single crystals exhibited a single magnetic domain behaviour dominated by the magnetocrystalline anisotropy which cause the easy magnetic axis of the crystal to be perpendicular to the long axis of the MWCNT. α-Fe were also found in a single magnetic domain arrangement, however in this case instead of the magnetocrystalline anisotropy, the magnetic behaviour is dominated by the shape anisotropy, causing the easy axis of magnetization to be along the long axis of the MWCNT. In these reports [66,67] a critical diameter size of approximately 60 nm was given for a single magnetic domain of a spherical Fe_3C single crystal.

The formula used for this approximation is shown in equation (29) and can be also used to calculate the approximation for a critical diameter size in the case of a single magnetic domain of an approximately spherical α-Fe single crystal.

$$r_{\alpha-Fe} < \frac{9\pi\sqrt{A(K_{sa}-K_{ma})}}{\mu_0 M_s^2} \qquad (29)$$

Where K_{sa} is the shape anisotropy energy density of an elongated α-Fe (0.9×10^6J/m^3) or Fe_3C (0.3×10^6J/m^3) ellipsoids of revolution, K_{ma} is the magnetocrystalline anisotropy energy density of an elongated α-Fe (0.048×10^6J/m^3) or Fe_3C ($K_2 = 1.88\times 10^5$J/m^3 and $K_1 = 0.394 \times 10^6$ J/m^3) ellipsoids of revolution, M_s is the saturation magnetization (1.7×10^6A/m for α-Fe and 9.8×10^5A/m for Fe_3C) and A is the exchange stiffness constant that is 8.7×10^{-12} J/m for Fe_3C and 2.1×10^{-11} J/m for α-Fe [66,67,99,100,101]. The exchange stiffness constant can be written [99] as shown in equation (30):

$$A = 2JS^2z/a \qquad (30)$$

Where J is the exchange integral, a is the nearest neighbour distance, z is the number of sites in the unit cell (z=2 for body centered cubic) and S the spin [99].

The calculation in the case of α-Fe allows to roughly estimated a critical single magnetic domain diameter of 66 nm. The single crystals that we have shown above in the TEM micrographs, present always a diameter much lower than 66 nm. In the case of the radial structures, the filling diameter has been found always

in the range of ~ 17-37 nm, while in the case of flower-like structures the α-Fe filling diameter has been found always in the range between ~ 30-55 nm and only in rare cases the diameter of ~ 63 nm was observed.

If a control of the MWCNTs and filling length is required, the use of a quench can be considered. This fast cooling method can allow to reduce the length of the continuously filled MWCNTs.

In conclusion:

i) The critical single magnetic domain diameter of an elongated α-Fe particle is roughly estimated to be ~ 66 nm. This size depends on the changes of *K* anysotropy parameter.

ii) The single crystals that we have analyzed in the TEM micrographs, present always a high aspect ratio. In the case of the radial structures the filling diameter has been found always in the range of ~ 17-37 nm and the length in the range of 7-8 μm. In the case of flower-like structures the α-Fe filling diameter has been found always in the range between ~ 30-55 nm and only in rare cases the diameter of ~ 63 nm was observed. The average single crystal length was in the range of 19-21 μm.

iii) The high aspect ratio allows to control the *K* anysotropy parameter and therefore plays a crucial role in the control the magnetic properties of the α-Fe filling.

Chapter 4

Conclusions

In conclusion we have shown two new in-situ synthesis methods that allow to obtain CNTs continuously filled with α-Fe single crystals. These methods are: the viscous-boundary layer chemical vapour synthesis and the locally perturbed-vapour chemical vapour deposition. In the following the specific conclusions related to each method are listed:

- 1) In the first method, radial structures comprising MWCNT continuously filled with ferromagnetic single crystals of α-Fe were produced in randomly fluctuating vapour in the viscous boundary layer between the rough surface of a quartz substrate and the laminar ferrocene/Ar vapour flow.
- 1.1) Continuous filling of the radial-MWCNTs was achieved by using Ar flow rates between 3.5 and 20 ccm. The best growth conditions to obtain radial structures with continuous filling were achieved with flow rates between 3.5 ccm and 12.5 ccm. We observed that, by increasing the vapour flow rate from 12.5 ccm to 20 ccm, the core (agglomeration of spherical nanoparticles) becomes elongated, assuming a flattened shape. The radial structures produced at flow rates of 20 ccm still comprise

MWCNT filled continuously along the core, however the structure appears more fragile with respect to those obtained at lower flow rates.

- 1.2) The filling diameter has been found always in the range of ~ 17-37 nm
- 1.3) The main encapsulated phases were α-Fe, γ-Fe, and Fe_3C. Unlike the vertical array structures, the radial structures have a lower abundance of Fe_3C. The Fe_3C content diminishes with increasing vapour flow rates used in the reaction. Furthermore the γ-Fe quantity also diminishes with increasing vapour flow rate. At flow rates of 20 ccm there was no Fe_3C and only 2% of γ-Fe present in the continuous filling of the radial structures.
- 1.4) In all the reactions of the first method the source vapour was produced by sublimation of 60-100 mg of ferrocene in a quartz tube reactor with the following dimensions: length: 2 m, outer diameter: ~ 22 mm, inner diameter: ~ 19 mm, wall thickness: ~ 1.5 mm. The maximum temperature of the preheater was 180 °C, and the furnace temperature was ~ 990 ºC. The average Reynolds number for the ferrocene vapour flow was estimated to be *Re*=2-4. The duration of each reaction was 4.5 minutes. The reactor was cooled to room temperature at the natural rate of the furnace.
- 2) In the second method flower-like structures comprising MWCNTs continuously filled with α-Fe were produced through the creation of local-perturbation in a dense laminar ferrocene ($Fe(C_5H_5)_2$) vapour flow and an additional long annealing treatment.

- 2.1) Two type of substrates (with different geometry) were used to create a local perturbation: In the first case a small hole (approximately 1 mm diameter) in an otherwise smooth quartz substrate was used to locally perturb a laminar ferrocene/Ar vapour flow. In the second case a V shaped substrate was used to locally perturb the laminar flow.
- 2.2) Continuous filling of the MWCNTs was achieved with both the substrate geometries
- 2.3) Single-phase filling was achieved by a post-synthesis annealing at 500 ºC for 15 hours in Ar flow. In these conditions only partial sample oxidation of the MWCNTs was observed. Instead, annealing at 640 ºC resulted in complete oxidation of the flower-like structures into α-Fe_2O_3.
- 2.4) The large cross-sections of the flower-like structures ensures high capture and delivery feedstock to the base, and the absence of close packing in the emerging MWCNTs ensures a well-defined vapour-capture volume at the tips.
- 2.5) In all the reactions of the second method the source vapour was produced by sublimation of 80-111mg of ferrocene in a quartz tube reactor with the following dimensions: length: 2 m, outer diameter: ~ 22 mm, inner diameter: ~ 19 mm, wall thickness: ~ 1.5 mm. The maximum temperature of the preheater was 180 °C, and the furnace temperature was ~ 990 ºC. The Ar flow rate was 12.5 ccm and the average Reynolds number for the ferrocene vapour flow was estimated to be *Re*=2-4.
- 2.6) The duration of each reaction performed with the first substrate geometry was 4 minutes. The duration of each reaction performed with the second substrate geometry was 2 min.

- 2.8) The α-Fe continuous filling shows mainly a diameter of ~ 30 nm and ~ 55 nm.

The ferromagnetically filled carbon nanotube radial structures have potential for applications which exploit the high surface area and the high volume fraction of ferromagnetic material of an individual radial structure, for example as magnetic nanocomposite fillers, microwave absorbing materials, and magnetic particles for magnetorheological fluids. These structures have promise also for magnetic hyperthermia applications since the radial arrangement of the filled MWCNTs guarantees the ferromagnetic alignment of filled MWCNTs with an external magnetic field in any direction.

The powder containing the flower-like structures show a very high saturation magnetization of 189.5 emu/g comparable with the saturation magnetization of bulk α-Fe, and also a high coercivity of 580 Oe. The long α-Fe ferromagnetic single crystals are ideal for applications in quantum disk devices, enhancement of the magnetic loss in microwave absorption applications, enhancement of the torque when placed in a constant magnetic field, and oscillatory response on a time-varying magnetic field.

Chapter 5

Future work

There are numerous avenues of potential future work emerging from this project. These revolutionary methods could be extended to other metallocenes compounds with structure similar to ferrocene, as nickelocene or cobaltocene for the creation of alloys as for example ‘‘Permalloy ($Fe_{20}Ni_{80}$)’’ that is usually known for its high magnetic permeability or to tune the Curie temperature (as in $Fe_{73}Ni_{27}$) for applications in cancer thermotherapies (T_c ~ 42 °C) and magnetocaloric refrigeration (T_c ~25 °C). The use of other compounds with more carbon in the metallocene structure as for example ‘‘Bis(pentamethylcyclopentadienyl)iron’’ could allow to study also the effect of the viscous boundary layer in different pyrolysing systems.

The fast cooling method (quench) that has been shown could be used to control the length of the flower-like structures tailoring the single crystals length for applications that requires long continuously filled MWCNTs or short continuously filled MWCNTs.

Further studies of the fluctuating eddies created by rough surfaces would allow to produce smaller or bigger radial structures by reducing or increasing the size of the asperities (salient features) in a rough surface. This studies can allow to reach industrial production by introducing also new reactor designs, since the rough

surface could be obtained in all the reactor length and the reaction is self-sustaining.

Other important measurements could be done on the microwave absorption. The mechanism of microwave absorption in filled MWCNTs is not well understood and the role of the filling can be investigated by using these new structures. If the filling enhances the microwave absorption, the continuously filled MWCNTs obtained in our methods could be ideal for this application.

Furthermore the antiferromagnet/ferromagnet interaction could be investigated more by deliberately introducing the antiferomagnetic Mn or Cr in the system. For example the flower-like structures could be grown in a substrate partially (with a layer) or entirely composed of an antiferromagnetic material creating therefore a direct magnetic interaction between ferromagnetic and antiferromagnetic materials.

A neutron diffraction experiments would give also more knowledge about the magnetic domain arrangement of the α-Fe single crystals in the radial-structures and in the flower-like structures.

References

[1] Radushkevich LV, Lukyanovich VM. O strukture ugleroda, obrazujucegosja pri termiceskom razlozenii okisi ugleroda na zeleznom kontakte ("About the structure of carbon formed by thermal decomposition of carbon monoxide on iron substrate"). Zurn Fisic Chim 1952; 26: 88-95.

[2] Oberlin A, Endo M, Koyama T. Filamentous growth of carbon through benzene decomposition. Journal of Crystal Growth 1976; 32: 335-49.

[3] Iijima S. Helical microtubules of graphite carbon. Nature 1991; 354: 56.

[4] Iijima S, Ichihashi T. Single-shell carbon nanotubes of 1-nm diameter. Nature 1993; 363: 603.

[5] Terrones H, López-Urías F, Muñoz-Sandoval E, Rodríguez-Manzo J A, Zamudio A, Elías A L, et al. Magnetism in Fe-based and carbon nanostructures: Theory and applications. Solid State Sciences 2006; 8: 303-20.

[6] Dillon F C, Bajpai A, Koos A, Downes S, Aslam Z, Grobert N. Tuning the magnetic properties of iron-filled carbon nanotubes. Carbon 2012; 50: 3674-81.

[7] Leonhardt A, Ritschel M, Elefant D, Mattern N, Biedermann K, Hampel S, et al. Enhanced magnetism in Fe-filled carbon nanotubes produced by pyrolysis of ferrocene. Journal of Applied Physics 2005; 98: 074315.

[8] Gui X, Wei J, Wang K, Wang W, Lv R, Chang J, et al. Improved filling rate and enhanced magnetic properties of Fe-filled carbon nanotubes by annealing and magnetic separation. Materials Research Bulletin 2008; 43: 3441-6.

[9] Morelos-Gomez A, Lopez-Urıas F, Munoz-Sandoval E, Dennis C L, Shull R D, Terrones H, et al. Controlling high coercivities of ferromagnetic nanowires encapsulated in carbon nanotubes. Journal of Material Chemistry 2010; 20: 5906-5914.

[10] Leonhardt A, Ritschel M, Kozhuharova R, Graff A, Muhl T, Huhle R, et al. Synthesis and properties of filled carbon nanotubes. Diamond and Related Materials 2003; 12: 790-3.

[11] Golberg D, Mitome M, Muller Ch, Tang C, Leonhardt A, Bando Y. Atomic structures of iron-based single-crystalline nanowires crystallized inside multi-walled carbon nanotubes as revealed by analytical electron microscopy. Acta Materialia 2006; 54: 2567-2576.

[12] Karmakar S, Sharma S M, Mukadam M D, Yusuf S M, Sood A K. Magnetic behaviour of iron-filled multiwalled carbon nanotubes. Journal of Applied Physics 2005; 97: 054306.

[13] Prados C, Crespo P, Gonzalez J M, Hernando A, Marco J F, Gancedo R, et al. Hysteresis shift in Fe-filled carbon nanotubes due to γ-Fe. Physical Review B 2002; 65: 113405.

[14] Marco J F, Gancedo J R, Hernando A, Crespo P, Prados C, Gonzalez J M, et al. Mossbauer Study of Iron-Containing Carbon Nanotubes. Hyperfine Interactions 2002; 139: 535-42.

[15] Ermakova M A, Ermakov D Y, Chuvilin A L, Kuvshinov G G. Decomposition of Methane over Iron Catalysts at the Range of Moderate Temperatures: The Influence of Structure of the Catalytic Systems and the Reaction Conditions on the Yield of Carbon and Morphology of Carbon Filaments. Journal of Catalysis 2001; 201: 183-97.

[16] Bellucci S, Malesevic A. Physics of Carbon Nanostructures in: Physical Properties of Ceramic and Carbon Nanoscale Structures. Lecture Notes in Nanoscale Science and Technology: Springer; 11; 2011, 155-94.

[17] Muller C, Golberg D, Leonhardt A, Hampel S, Buchner B. Growth studies, TEM and XRD investigations of iron-filled carbon nanotubes. Physica status solidi (a) 2006; 203: 1064-68.

[18] Callister W D. Fundamentals of Materials Science and Engineering: John Wiley and Sons; 2007.

[19] Singhal S C, Worrell W L. High Temperature Materials: Proceedings of a Symposium in Honor of the 65th Birthday of professor Wayne L. Worrell: The Electrochemical Society Inc; 2002.

[20] Chen C, Zhang Y. Nanowelded Carbon Nanotubes: From Field-Effect Transistors to Solar Microcells:Springer; 2009.

[21] Saito Y, Yoshikawa T. Interlayer spacings in carbon nanotubes. Physical Review B 1993; 48: 1907-09.

[22] Winterer M. Nanocrystalline Ceramics - Synthesis and Structure: Springer, Heidelberg, Springer Series in Materials Science Volume 53; 2002.

[23] Jorio A, Dresselhaus G, Dresselhaus M S. Carbon nanotubes, advanced topics in the Synthesis, Structure, Properties and Applications: Springer publishing; 2008.

[24] Weissker U, Hampel S, Leonhardt A, Buchner B. Carbon Nanotubes Filled with Ferromagnetic Materials. Materials 2010; 3: 4387-427.

[25] Mehrotra R. C. Organometallic Chemistry: New Age International; 2004.

[26] Hampel S, Leonhardt A, Selbmann D, Biedermann K, Elefant D, Muller Ch, et al. Growth and characterization of filled carbon nanotubes with ferromagnetic properties. Carbon 2006; 44: 2316-22.

[27] Cheng J, Zou X P, Zhu G, Wang M F, Su Y, Yang G Q, et al. Synthesis of iron-filled carbon nanotubes with a great excess of ferrocene and their magnetic properties. Solid State Communications 2009; 149: 1619-22.

[28] Chakraborty A K, Jacobs J, Anderson C, Roberts C J, Hunt M R C. Chemical vapor deposition growth of carbon nanotubes on Si subtrates using Fe catalyst: What happens at the nanotube/Fe/Si interface. Journal of Applied Physics 2006; 100: 084321.

[29] Joon Jung Y, Wei B, Vajtai R, Ajayan P M, Homma Y, Prabhakaran K, et al. Mechanism of Selective Growth of Carbon Nanotubes on SiO_2/Si Patterns. Nanoletters 2003; 3: 561-64.

[30] Mullin J W. Crystallization: Butterworth and Co. Publishers Limited; 1961.

[31] Cao G, Wang Y. Nanostructures and Nanomaterials, Synthesis, Properties and Applications. World Scientific series in nanoscience and nanotechnology: World Scientific Publishing Co. Pte. Ltd; 2011.

[32] Flickinger M C. Downstream Industrial Biotechnology: Recovery and Purification. Wiley; 2013.

[33] Ducati C, Alexandrou I, Chhowalla M, Robertson J, Amaratunga G A J. The role of the catalytic particle in the growth of carbon nanotubes by plasma enhanced chemical vapor deposition. Journal of Applied Physics 2004; 95: 6387-91.

[34] Groudeva-Zotova S, Kozhuharova R, Elefant D, Muhl T, Schneider C M, Monch I. Phase composition and magnetic characteristics of Fe-filled multi-walled carbon nanotubes. Journal of Magnetism and Magnetic Materials 2006; 306: 40–50.

[35] Moisala A, Nasibulin A G, Kauppinen E I. The role of metal nanoparticles in the catalytic production of single-walled carbon nanotubes—a review. Journal of Physics: Condensed Matter 2003; 15: S3011–35.

[36] Kumar M, Ando Y. Chemical Vapor Deposition of Carbon Nanotubes: A Review on Growth Mechanism and Mass Production. Journal of Nanoscience and Nanotechnology. 2010; 10: 3739–58.

[37] Moshkalev SA , Verissimo C. Nucleation and growth of carbon nanotubes in catalytic chemical vapor deposition. Journal of Applied Physics 2007; 102: 044303.

[38] Louchev O A, Kanda H. Thermal physics in carbon nanotube growth kinetics. Journal of Chemical Physics 2004; 121:446-56.

[39] Ren W, Li F, Cheng H M. Evidence for, and an Understanding of, the Initial Nucleation of Carbon Nanotubes Produced by a Floating Catalyst Method. Journal of Physical Chemistry B 2006; 110: 16941-6.

[40] Hofmann S, Sharma R, Ducati C, Du G, Mattevi C, Cepek C et al. In situ Observations of Catalyst Dynamics during Surface-Bound Carbon Nanotube Nucleation. Nano Letters 2007;7: 602-8.

[41] Raty J Y, Gygi F, Galli G. Growth of Carbon Nanotubes on Metal Nanoparticles: A Microscopic Mechanism from *Ab Initio* Molecular Dynamics Simulations. Physical Review Letters 2005; 95: 096103 .

[42] Helveg S, Lopez-Cartes C, Sehested J, Hansen P L, Clausen B S, Rostrup-Nielsen J R, Abild-Pedersen F, NørskovJ K. Atomic-scale imaging of carbon nanofibre growth Nature 2004; 427: 426-9.

[43] Ruoff RS, Lorents DC, Chan B, Malhotra R, Subramoney S. Single crystal metals encapsulated in carbon nanoparticles. J Nanoscience Nanotechnology 1993; 259:346–8.

[44] Rodríguez-Manzo J A, Terrones M , Terrones H , Kroto HW, Sun L, Banhart F. *In situ* nucleation of carbon nanotubes by the injection of carbon atoms into metal particles. Nature Nanotechnology 2007; 2: 307 -11.

[45] Kim M S, Rodriguez N M, Baker R T K. The role of interfacial phenomena in the structure of carbon deposits. Journal of Catalysis 1992; 134 : 253–68.

[46] Baker R T K, Harris P S. The formation of filamentous carbon. Chemistry and Physics of Carbon 1978; 14: 83.

[47] Tibbetts G G. Why are carbon filaments tubular? Journal of Crystal Growth 1984; 66: 632-38

[48] Wagner R S, Ellis W C. Vapor-Liquid-Solid Mechanism of Single Crystal Growth. Applied Physics Letters 1964; 4: 89.

[49] Ding F, Rosen A, Bolton K. The role of the catalytic particle temperature gradient for SWNT growth from small particles. Chemical Physics Letters 2004; 393: 309-13.

[50] Schaper A K, Hou H, Greiner A, Phillipp F. The role of iron carbide in multiwalled carbon nanotube growth. Journal of Catalysis 2004; 222: 250-4.

[51] Li Y, Chen J, Ma Y, Zhao J, Qin Y, Chang L. Formation of bamboo-like nanocarbon and evidence for the quasi-liquid state of nanosized metal particles at moderate temperatures. Chemical Communications 1999; 1141-2.

[52] Kim H, Sigmund W. Iron particles in carbon nanotubes. Carbon 2005; 43: 1743-8.

[53] Kim H, Kaufman Mj, Sigmund Wm, Jacques D, Andrews R. Observation and formation mechanism of stable face centered-cubic Fe nanorods in carbon nanotubes. Journal of Materials Research 2003; 18:1104-8.

[54] Schneider A. Iron layer formation during cementite decomposition in carburising atmospheres. Corrosion Science 2002; 44: 2353-65.

[55] Zhang J, Schneider A, Inden G. α- Fe layer formation during metal dusting of iron in CO-H_2-H_2O gas mixtures. Materials and Corrosion 2003; 54: 763-9.

[56] Zhang J, Schneider A, Inden G. Effect of gas composition on cementite decomposition and coke formation on iron. Corrosion Science 2003; 45: 281-99.

[57] Zhang J, Schneider A, Inden G. Coke formation during metal dusting of iron in CO-H_2-H_2O gas with high CO content. Materials and Corrosion 2003; 54: 770-7.

[58] Wei Q, Pippel E, Woltersdorf J, Grabke H J. Microprocesses of coke formation in metal dusting. Materials and Corrosion 1999; 50: 628-33.

[59] Pippel E, Woltersdorf J, Schneider R. Micromechanisms of metal dusting on Fe-base and Ni-base alloys. Materials and Corrosion 1998; 49: 309-16.

[60] Grabke H J. Thermodynamics, mechanisms and kinetics of metal dusting. Materials and Corrosion 1998; 49: 303-8.

[61] Grabke H J. Carburization, carbide formation, metal dusting, coking. Materiali in tehnologije 2002; 36: 297-305.

[62] Podgurski H H, Kummer J T, DeWitt T W, Emmet P H. Preparation, Stability and Adsorptive Properties of the Carbides of Iron. Journal of the American Chemical Society 1950; 72: 5382-8.

[63] Guo T, Nikolaev P, Rinzler A G, Tomanek D, Colbert D T, Smalley R E. Self-Assembly of Tubular Fullerenes. Journal of Physical Chemistry 1995; 99: 10694-7.

[64] Kwon Y-K, Lee Y H, Kim S-G, Jund P, Tomanek D, Smalley R E. Morphology and Stability of Growing Multiwall Carbon Nanotubes. Physical Review Letters 1997; 79: 2065-8.

[65] Ruskov T, Spirov I, Ritschel M, Muller C, Leonhardt A, Ruskov R. Mossbauer morphological analysis of Fe-filled multiwalled carbon nanotube samples. Journal of Applied Physics 2006; 100: 084326.

[66] Weissker U, Loffler M, Wolny F, Lutz M U, Scheerbaum N, Klingeler R, et al. Perpendicular magnetization of long iron carbide nanowires inside carbon nanotubes due to magnetocrystalline anisotropy. Journal of Applied Physics 2009; 106: 054909.

[67] Lutz M U, Weissker U, Wolny F, Muller C, Loffler M, Muhl T, et al. Magnetic properties of α-Fe and Fe_3C nanowires. Journal of Physics: Conference Series 2010; 200: 072062.

[68] Hammond C. The basics of Crystallography and Diffraction: Oxford Science Publications; 2009.

[69] Lv R, Tsuge S, Gui X, Takai K, Kang F, Enoki T, et al. In situ synthesis and magnetic anisotropy of ferromagnetic buckypaper. Carbon 2009; 47: 1141-5.

[70] Likodimos V, Glenis S, Guskos N, Lin C L. Magnetic and electronic properties of multiwall carbon nanotubes. Physical Review B 2003; 68: 045417.

[71] Philippi S, Weißker U, Muhl T, Leonhardt A, Buchner B. Room temperature magnetometry of an individual iron filled carbon nanotube acting as nanocantilever. Journal of Applied Physics 2011; 110: 084319.

[72] Klingeler R, Sim R B, editors. Carbon Nanotubes for Biomedical Applications: Springer; 2011.

[73] Lutz M U, Lipert K, Krupskaya Y, Bahr S, Wolter A, El-Gendy A A, et al. Feasibility of Magnetically Functionalised Carbon Nanotubes for Biological Applications: From Fundamental Properties of Individual Nanomagnets to Nanoscaled Heaters and Temperature Sensors. In: Klingeler R, Sim R B, editors. Carbon Nanotubes for Biomedical Applications: Springer Berlin Heidelberg; 2011, 97-124.

[74] Taylor A, Lipert K, Kramer K, Hampel S, Fussel S, Meye A, et al. Biocompatibility of iron filled carbon nanotubes in vitro. Journal of Nanoscience and Nanotechnology 2009; 9: 5709-16.

[75] Elhissi M A A, Ahmed W, Hassan I Ul, Dhanak V R, D'Emanuele A. Carbon Nanotubes in Cancer Therapy and Drug Delivery. Journal of Drug Delivery 2012; 837327: 1-10.

[76] Sitharaman B, Wilson L J. Gadonanotubes as new high-performance MRI contrast agents. International Journal of Nanomedicine. 2006; 1: 291-5.

[77] Watts P C P, Hsu W K, Randall D P, Kotzeva V, Chen G Z. Fe-Filled Carbon Nanotubes: Nano-electromagnetic Inductors. Chemistry of Materials 2002; 14: 4505-8.

[78] Wolny F, Muhl T, Weissker U, Lipert K, Schumann J, Leonhardt A, et al. Iron filled carbon nanotubes as novel monopole-like sensors for quantitative magnetic force microscopy. Nanotechnology 2010; 21: 435501.

[79] Hudziak S, Darfeuille A, Zhang R, Peijs T, Mountjoy G, Bertoni G, et al. Magnetoresistive phenomena in an Fe-filled carbon nanotube/elastomer composite. Nanotechnology 2010; 21: 125505.

[80] Lin H, Zhu H, Guo H, Yu L. Investigation of the microwave-absorbing properties of Fe-filled carbon nanotubes. Materials Letters 2007; 61: 3547-50.

[81] Noriaki S, Masakazu N, Takeyuki K. Enhanced field emission properties of films consisting of Fe-core carbon nanotubes prepared under magnetic field. Carbon 2007; 45: 78-82.

[82] Holman J P. Heat Transfer: McGraw-Hill, Inc; 1976.

[83] Perry A E, Schofield W H, Joubert P N. Rough Wall Turbulent Boundary Layers. Journal of Fluid Mechanics 1969; 37: 383-412.

[84] Riedl T, Gemming T, Wetzig K. Extraction of EELS white-line intensities of manganese compounds: Methods, accuracy, and valence sensitivity. Ultramicroscopy 2006; 106: 284-91.

[85] Pearson D H, Ahn C C, Fultz B. White lines and d-electron occupancies for the 3d and 4d transition metals. Physical Review B 1993; 47: 8471.

[86] Zandbergen H W, Andersen S J, Jansen J. Structure determination of Mg_5Si_6 particles in Al by dynamic electron diffraction studies.Science 1997; 277: 1221-5.

[87] Williams D B , Carter C B. Transmission Electron Microscopy: Plenum Press New York and London; 1996.

[88] Nagakura S, Nakamura Y, Suzuki T. Forbidden reflection intensity in electron diffraction and its influence on the crystal structure image. Japanese Journal of Applied Physics 1982; 21: L449-L451.

[89] Tanaka M, Sekii H, Nagasawa T. Space-group determination by dynamic extinction in convergent-beam electron diffraction. Acta Crystallographica 1983; A 39: 825-37.

[90] Gjonnes J, Moodie A F. Extinction conditions in the dynamic theory of electron diffraction. Acta Crystallographica 1965; 19: 65-7.

[91] Cowley J M, Moodie A F. The scattering of electrons by atoms and crystals. III. Single-crystal diffraction patterns. Acta Crystallographica 1959; 12: 360-7.

[92] Wetscher F, Pippan R, Sturm S, Kauffmann F, Scheu C, Dehm G. TEM investigations of the structural evolution in a pearlitic steel deformed by high-pressure torsion. Metallurgical and Materials Transactions 2006; A 37: 1963-8.

[93] Kurata H, Tanaka N. Iron $L_{2,3}$ white line ratio in nm-sized γ-iron crystallites embedded in MgO. Microscopy Microanalysis Microstructures 1991; 2: 183-90.

[94] Leapman R D, Grunes L A, Fejes P L. Study of the L_{23} edges in the 3d transition metals and their oxides by electron-energy-loss spectroscopy with comparisons to theory. Physical Review B 1982; 26: 614-35.

[95] Nicolis G, Prigogine I. Self-Organization in Nonequilibrium Systems: From Dissipative Structures to Order Through Fluctuations: Wiley; 1977.

[96] Hastie J W.10 th. materials research symposium on characterization of high temperature vapors on gases: NBS special publication 561 n.1; 1978.

[97] Roca A G, Morales M P , Grady K O, Serna C J. Structural and magnetic properties of uniform magnetite nanoparticles prepared by high temperature decomposition of organic precursors. Nanotechnology 2006; 17: 2783.

[98] Liu Z, Lv B, Wu D, Sun Y, Xu Y. Magnetic and electrochemical behavior of rhombohedral Fe_2O_3 nanoparticles with (104) dominant facets. Particuology 2013; 11: 327-33.

[99] Blundell S. Magnetism in Condensed Matter: Oxford Master Series in Condensed Matter Physics; 2001.

[100] Sattler K D, Handbook of Nanophysics: Principles and Methods: CRC Press, Taylor and Francis group; 2011.

[101] Getzlaff M. Fundamentals of Magnetism: Springer; 2003.